

# Defining the Relationship between Seismicity and Deformation at Regional and Local Scales

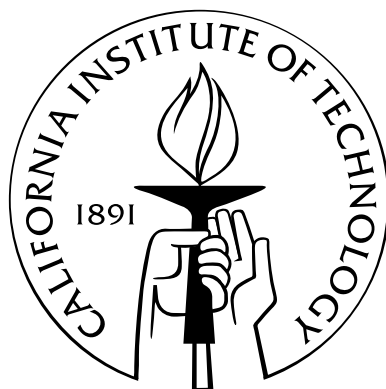
Thesis by

Nneka Njeri Akosua Williams

In Partial Fulfillment of the Requirements

for the Degree of

Doctor of Philosophy



California Institute of Technology

Pasadena, California

2013

(Defended August 14, 2012)

© 2013

Nneka Njeri Akosua Williams

All Rights Reserved

# Acknowledgements

There are a whole lot of people I need to thank for helping me make it through Caltech. I would like to start off with my advisor Professor Brian Wernicke. He has always been incredibly supportive and understanding. I want to thank him for being tolerant of my flaws and being a generally fun person to be around. I also want to thank Professor Don Helmberger for posing brilliant questions that keep me thinking for weeks (and sometimes months!). He also has a great sense of humor that has always kept me at ease. Professor Joann Stock has always been had door open for me, whether I want to talk about science or life, and I am very thankful for that as well. I would also like to thank Professor Paul Asimow for asking tough questions that make me squirm but also make me think. I truly feel that he has helped me to become a better scientist. Lastly, I like to thank Professor Tom Heaton for helping me to improve my knowledge of seismology when I needed it most.

As for folks who are not professors, I would like to thank Shengji Wei for putting up with me and my incessant questions when I did not know how to code my way out of a paper bag and for helping me figure out why my microseismic data refused to run with CAP. Mike Black and Scott Dungan, the Linux Help guys have always been incredibly friendly and helpful and I am very thankful that they have helped me triumph over my Linux box, Magic. I would also like to thank Kim Klotz, Dian Buchness, Marcia Hudson, and my officemate and friend Nina Lin for chatting with me when it was time to procrastinate.

And last but certainly not least, I would like to thank my husband Geoff Hardy for commuting to Irvine for 5 years so that I could bike to school, for high quality companionship, and emotional support. I would also like to thank him for being my best friend and loving me even when my research made me grumpy or kept us apart. Thank you all!

# Abstract

In this thesis, I use source inversion methods to improve understanding of crustal deformation along the Nyainquentanglha (NQTL) Detachment in Southern Tibet and the Piceance Basin in northwestern Colorado. Broadband station coverage in both regions is sparse, necessitating the development of innovative approaches to source inversion for the purpose of studying local earthquakes.

In an effort to study the 2002-2003 earthquake swarm and the 2008  $M_w$  6.3 Damxung earthquake and aftershocks that occurred in the NQTL region, we developed a single station earthquake location inversion method called the SP Envelope method, to be used with data from LHSA at Lhasa, a broadband seismometer located 75 km away. A location is calculated by first rotating the seismogram until the azimuth at which the envelope of the P-wave arrival on the T-component is smallest (its great circle path) is found. The distance at which to place the location along this azimuth is measured by calculating the S-P distance from arrivals on the seismogram. When used in conjunction with an existing waveform modeling based source inversion method called Cut and Paste (CAP), a catalog of 40 regional earthquakes was generated.

From these 40 earthquakes, a catalog of 30 earthquakes with the most certain locations was generated to study the relationship of seismicity and NQTL region faults mapped in Google Earth<sup>TM</sup> and in *Armijo et al.* (1986) and *Kapp et al.* (2008). Using these faults and focal mechanisms, a fault model of the NQTL Region was generated using GOCAD, a 3D modeling suite. By studying the relationship of modeled faults to mapped fault traces at the surface, the most likely fault slip plane was chosen. These fault planes were then used to calculate slip vectors and a regional bulk stress tensor, with respect to which the low-angle NQTL Detachment was found to be badly misoriented. The formation of low-angle normal faults is inconsistent with the Anderson Theory of faulting, and

the presence of the NQTL Detachment in a region with such an incongruous stress field supports the notion that such faults are real.

The timing and locations of the earthquakes in this catalog with respect to an anomalous increase in the eastward component of velocity readings at the single cGPS station in Lhasa (LHAS) were analyzed to determine the relationship between plastic and brittle deformation in the region. The fact that cGPS velocities slow significantly after the 2002-2003 earthquake swarm suggests that this motion is tectonic in nature, and it has been interpreted as only the second continental slow slip event (SSE) ever to be observed. The observation of slow slip followed by an earthquake swarm within a Tibetan rift suggests that other swarms observed within similar rifts in the region are related to SSEs.

In the Piceance Basin, CAP was used to determine source mechanisms of microearthquakes triggered as a result of fracture stimulation within a tight gas reservoir. The expense of drilling monitor wells and installing borehole geophones reduces the azimuthal station coverage, thus making it difficult to determine source mechanisms of microearthquakes using more traditional methods. For high signal to noise ratio records, CAP produced results on par with those obtained in studies of regional earthquakes. This finding suggests that CAP could successfully be applied in studies of microseismicity when data quality is high.

# Contents

<b>Acknowledgements</b>	<b>iii</b>
<b>Abstract</b>	<b>iv</b>
<b>List of Figures</b>	<b>ix</b>
<b>List of Tables</b>	<b>xii</b>
<b>1 Introduction</b>	<b>1</b>
<b>2 Building an Earthquake Catalog for the Nyainquentanglha Detachment Region in Southern Tibet, Using a New Method of Single Station Location Inversion</b>	<b>5</b>
2.1 Introduction . . . . .	5
2.2 Single Station Earthquake Location—The State of the Art . . . . .	9
2.3 Previous Studies of Tibetan Seismicity . . . . .	9
2.4 Data . . . . .	11
2.5 Methods . . . . .	11
2.5.1 Source Mechanism Inversion using Cut and Paste (CAP) . . . . .	11
2.5.2 Preliminary CAP Results . . . . .	13
2.6 Earthquake Location Determination . . . . .	18
2.6.1 SP Envelope Method . . . . .	18
2.7 Results . . . . .	33
2.7.1 Characteristics of Located Earthquakes . . . . .	33
2.8 Discussion . . . . .	36

2.8.1	Single-Station CAP vs. 5 Station CAPloc Mechanisms and Locations . . . . .	36
2.8.2	$M_w$ 6.3 Damxung Earthquake Location from Joint Inversion of InSAR and Broadband Seismic (CAPloc) . . . . .	41
2.9	Conclusion . . . . .	43
<b>3</b>	<b>Crustal Deformation along the Nyainquentanglha Detachment Region, Southern Tibet, from Local seismicity and 3D Fault Modeling</b>	<b>44</b>
3.1	Introduction . . . . .	44
3.1.1	Geologic Setting of the NQTL Detachment . . . . .	46
3.2	Data . . . . .	48
3.2.1	Faults . . . . .	48
3.2.2	Earthquakes . . . . .	52
3.3	Analysis . . . . .	55
3.3.1	Defining Active Faults Using Alignments of Similar Focal Planes . . . . .	55
3.4	Slip Vector Patterns and Stress Tensor Calculations . . . . .	62
3.5	Discussion . . . . .	67
3.6	Conclusions . . . . .	69
<b>4</b>	<b>A Possible Continental Slow Slip Event in the Nyainquentanglha Detachment Region, Southern Tibet</b>	<b>71</b>
4.1	Introduction . . . . .	71
4.2	Data and Methods . . . . .	73
4.3	Results . . . . .	73
4.4	Discussion and Conclusions . . . . .	75
<b>5</b>	<b>Using Cut and Paste to Invert for Microearthquake Source Mechanisms – A Preliminary Study</b>	<b>80</b>
5.1	Introduction . . . . .	80
5.2	Geological Setting of the Piceance Basin . . . . .	83

5.3	Data . . . . .	83
5.3.1	Tools and Acquisition Geometry . . . . .	83
5.3.2	Piceance Microearthquakes and Their Locations . . . . .	87
5.4	Methods . . . . .	89
5.4.1	Data Preparation . . . . .	89
5.4.2	Running CAP . . . . .	91
5.5	Results . . . . .	92
5.5.1	Event Mechanisms . . . . .	92
5.6	Discussion . . . . .	100
5.7	Conclusion . . . . .	109
	<b>Bibliography</b>	<b>110</b>

# List of Figures

2.1	Yadong Gulu Rift and surrounding area. . . . .	8
2.2	An example CAP output. . . . .	13
2.3	Five station CAPloc results for event 20081009175922, an aftershock of the 2008 $M_w$ 6.3 Damxung earthquake. . . . .	16
2.4	Comparison of CAP results obtained using various methods. . . . .	17
2.5	Schematic of seismogram rotation with rotated seismogram. . . . .	20
2.6	SP Envelope result for the 2008 $M_w$ 6.3 Damxung earthquake. . . . .	21
2.7	Degrees vs. Envelope Plot for the 2008 $M_w$ 6.3 Damxung earthquake. . . . .	22
2.8	SP Envelope Method workflow. . . . .	30
2.9	2002 earthquake swarm locations calculated using the SP envelope method. . . . .	34
2.10	2008 earthquake swarm locations calculated using the SP envelope method. . . . .	35
2.11	Four station CAPloc results for the 2008 $M_w$ 6.3 Damxung earthquake. . . . .	37
2.12	InSAR inversion results from <i>Wei et al. (2009)</i> . . . . .	42
3.1	Major Tibetan Faults. . . . .	47
3.2	The NQTL region and interpreted cross sections from <i>Cogan et al. 1998</i> . . . . .	50
3.3	Fault map of the NQTL Region. . . . .	51
3.4	Low LUR events from the 2002-2003 earthquake swarm. . . . .	54
3.5	Low LUR events from the 2008 mainshock and aftershock sequence. . . . .	55
3.6	NQTL Region earthquake locations with respect to the NQTL . . . . .	57
3.7	Group 1 earthquakes. . . . .	58
3.8	Group 2 earthquakes. . . . .	60

3.9	Group 3 and group 4 earthquakes. . . . .	61
3.10	Stereonet of the most likely fault planes of earthquakes in the LUR catalog and their associated slip vectors. . . . .	64
3.11	Slip Vectors associated with most likely planes plotted in map view. . . . .	65
3.12	Slip Vectors associated with most likely planes plotted in map view (continued). . . . .	66
4.1	cGPS records from LHAS at Lhasa Tibet from 1995 to 2004. . . . .	74
4.2	Velocity anomalies measured within the BARGEN network in the Basin and Range. . . . .	74
4.3	The east component of velocity measure at the cGPS station at LHAZ before and after the 2008 ( $M_w$ 6.3) Damxung earthquake. The red line indicates the timing of the Damxung earthquake. . . . .	76
4.4	Schematic of deformation within the Yadong Gulu Rift Valley and surrounding regions between 2000 and 2010. . . . .	77
5.1	The Piceance Basin of northwestern Colorado. . . . .	84
5.2	Piceance basin regional stratigraphy. . . . .	85
5.3	Schematic of geophone positioning, array locations, and microearthquakes. . . . .	86
5.4	Event locations calculated using P and S arrivals from geophones in both arrays (triangles) and array 2 P and S Picks and P-hodograms. . . . .	87
5.5	A 3-component record of event 5069 from geophone 13 in array 2. . . . .	90
5.6	CAP source mechanisms obtained using locations obtained from P and S arrivals and for all three runs. . . . .	93
5.7	CAP source mechanisms obtained using locations obtained from P and S arrivals and for all three runs (continued). . . . .	94
5.8	CAP source mechanisms obtained using locations obtained from array 2's P and S arrivals and P-hodograms for all three runs. . . . .	95
5.9	CAP source mechanisms obtained using locations obtained from array 2's P and S arrivals and P-hodograms for all three runs. . . . .	96

5.10	The R-components of event 5169 records. . . . .	98
5.11	The R components of event 5547 records. . . . .	99
5.12	Event 5779 CAP result at 1.50 km depth. . . . .	106
5.13	Moveout imaged in the Z component of event 5779, recorded in array 2. . . . .	107
5.14	The R component of event 5740 recorded in array 2 is a good example of a noisy record.	108

# List of Tables

2.1	Velocity Model for the Tibetan Plateau . . . . .	13
2.2	Single Station CAP Results Obtained Using ISC Locations . . . . .	15
2.3	Single Station CAP Results Obtained Using Locations From All Methods . . . . .	19
2.4	Single Station CAP - Time Shifts and Fits from 2002-2003 Earthquakes . . . . .	23
2.5	Single Station CAP (Continued 1) - Time Shifts and Fits from 2002-2003 Earthquakes	24
2.6	Single Station CAP (Continued 2) - Time Shifts and Fits from 2002-2003 Earthquakes	25
2.7	Single Station CAP - Time Shifts and Fits from 2008 Earthquakes . . . . .	26
2.8	Single Station CAP (Continued 1) - Time Shifts and Fits from 2008 Earthquakes . . .	27
2.9	Single Station CAP (Continued 2) - Time Shifts and Fits from 2008 Earthquakes . . .	28
2.10	Single Station CAP (Continued 3) - Time Shifts and Fits from 2008 Earthquakes . . .	29
2.11	Single Station CAP Results Obtained Using Best Locations - 2002-2003 Events . . . . .	31
2.12	Single Station CAP Results Obtained Using Best Locations - 2008 Events . . . . .	32
2.13	10/6/2008 Damxung Earthquake Source Mechanisms and Fault Parameters . . . . .	38
2.14	10/6/2008 Damxung Earthquake - Time Shifts and Fits of all Methods . . . . .	40
3.1	Single Station CAP Results - Low Location Uncertainty Range (LUR) Catalog . . . . .	53
3.2	Slick program outputs . . . . .	70
5.1	Altcom Velocity Model . . . . .	88
5.2	CAP Time Shifts and Fits for locations from Array 2 P and S Picks and P-Hodograms	101
5.3	CAP Time Shifts and Fits for locations from P and S Picks . . . . .	102
5.4	Microearthquake Source Parameters - Locations from P and S Picks . . . . .	103

5.5 Microearthquake Source Parameters - Locations from Array 2 P and S Picks and P-  
Hodograms . . . . . 104

# Chapter 1

## Introduction

Regional deformation within the seismogenic zone of the crust manifests itself in the form of large-scale faults. Geologists performing field studies can determine fault geometries near the surface, but any thorough study of regional deformation requires that we know how faults behave at depth. The study of earthquake locations and source mechanisms can allow us to better understand fault behavior by revealing the orientations of faults and the sense of slip which occurs on them. Studies such as these help us to define the relationship between faulting and deformation and can be performed at regional and local scales.

One tool that can be used to obtain the source mechanisms of earthquakes is Cut and Paste (CAP), a waveform modeling method developed in the early 1990s here at the California Institute of Technology. This method, first outlined in Zhao and Helmberger [1994] calculates a source mechanism by splitting a broadband seismogram into body wave and surface wave sections and then cross correlating the resulting data to synthetic seismograms obtained by performing a grid search of optimum fault orientation characteristics. First applied in Southern California, this method has been successful in studies of seismicity and deformation in regions all over the world. In this thesis, I use CAP to determine the source mechanism of earthquakes which occur along the Nyainqentanglha (NQTL) Detachment in Southern Tibet. CAP is especially well suited for use in this region because it can obtain reliable results in regions where broadband station coverage is sparse. In the case of the NQTL region, there is only one permanent broadband seismometer, and it is situated in Lhasa, approximately 75 km away.

Using data from the single station at Lhasa (LHSA) I performed a series of studies which reveal the nature of crustal deformation in the NQTL region. In chapter 2, I develop a new single station earthquake location inversion method. This method, called SP Envelope, when used in conjunction with CAP allows for the determination of source mechanisms and locations. Both methods were applied to locate and determine the source characteristics of a swarm of earthquakes which occurred in and near the Yangbajain valley between 2002 and 2003. In 2008, the  $M_w$  6.3 Damxung Earthquake and aftershock series occurred in the same region and were recorded not only at LHSA, but also by multiple broadband stations installed by the Chinese government in the years after the earthquake swarm. In order to validate the SP envelope method, we applied CAPloc, a version of CAP which is able to invert for accurate source locations if given broadband data from multiple stations, to the data obtained from these new stations. By comparing CAPloc and CAP/SP envelope inversions of events recorded by both LHSA and the Chinese stations in 2008, I was able to confirm the efficacy of the new joint method. I then used CAP/SP Envelope to compile an earthquake catalog of 40 events which could be used to study crustal deformation in the NQTL Region and the large Yadong-Gulu Rift of which it is a small part.

In chapter 3, I use this earthquake catalog along with digitized maps of Quaternary faults and the results of seismic refraction surveys to generate a 3D fault model. The 3D faults within the model are simply extensions of the fault surfaces represented by the earthquake source mechanisms obtained by CAP. By comparing the strikes of these 3D faults with the trends of the digitized surface faults, I was able to make an educated guess as to which of the two fault planes represented by the source mechanism is the one on which slip occurred. Using this “most likely” fault plane information, I was then able to generate vectors showing sense of slip on each of these planes. The pattern of slip revealed by these vectors suggests that the earthquakes in this region are related to the isostatic rebound of the crust as a result of extension along the NQTL Detachment. Using software developed in *Michael* (1984), I was able to take my analysis one step further by calculating the bulk stress tensor for the region in which the earthquakes occurred. The results of this analysis indicate that the stress field in this region is oriented in a way that would discourage the formation of low-angle

normal faults such as the NQTL. The NQTL is also found to be misoriented with respect to the stress field. The formation of low-angle normal faults is inconsistent with the Anderson Theory of faulting and their existence is a hotly debated topic in the field of structural geology. The fact that we observe them in the NQTL region supports the notion that such faults are real.

In chapter 4, I focus on the timing and location of the 2002-2003 earthquake swarm and 2008 mainshock/aftershock series with respect to anomalous velocity readings at the single cGPS station in Lhasa (LHAS) in order to explore the possible relationship between brittle deformation along the NQTL and plastic deformation along a surface beneath it. Between 2001 and mid 2002 there was an increase in the eastward component of velocity recorded at LHAS. This increase in velocity was followed by the NQTL region swarm. After the swarm presumably released potential energy within the region, the eastward component of motion measured at LHAS slowed significantly. This finding is very exciting because the motion observed at the cGPS station is very similar to that observed at cGPS stations situated along subduction zones. These stations often record slow slip occurring along the subduction interface. Before Wernicke et al. [2008], published observations of such slow slip events (SSEs) occurring in the Basin and Range Province, these events were not thought to occur in continental settings. The observations at LHAS and the occurrence of earthquakes with source mechanisms consistent with eastward motion along an interface beneath the region suggest that SSE could be occurring in Tibet as well. This result is very exciting because this event would be only the second continental SSE ever observed. The fact that the mainshock/aftershock series 2008 event was not preceded by an anomalous change in cGPS recorded at LHAS suggests that such slow slip events are only associated with swarms. The observation of slow slip followed by an earthquake swarm within a Tibetan rift suggests that other swarms observed within similar rifts in the region are related to continental SSEs.

Chapter 5 is different from the others in that the study region has shifted from Tibet to northwestern Colorado. The Piceance Basin is another region in which the relationship between seismicity and crustal deformation can be studied. This basin contains a large tight gas reservoir from which hydrocarbons can only be produced if fracture stimulation is performed. Hydraulic fractur-

ing of tight sands, such as the Piceance Basin's Williams Fork Formation produces thousands of microearthquakes. Service companies that perform the hydraulic fracturing generally only provide the oil company with microearthquake locations. These locations, although useful for charting the progression of fracture formation, tell us nothing about the geometry of the fractures formed. Limitations in station coverage caused by the expense of drilling monitor wells and installing borehole geophones reduce the azimuthal coverage of the small area in which fracturing is occurring. This limited coverage makes it very difficult to determine the source mechanisms of microearthquakes using traditional methods such as plotting the first motions of P-wave arrivals measured at borehole geophones. In an effort to work around the problem of sparse station coverage, I have worked to use CAP in the inversion of microearthquake source mechanisms. CAP, although promising, produced mediocre results because the signal to noise ratio of the data was quite low. In cases where the data was less noisy, CAP produced results on par with those obtained in studies of regional earthquakes. This result suggests that CAP could successfully be applied in studies of microseismicity when data quality is high.

The results obtained in each of these chapters demonstrate how the study of seismicity in conjunction with geology can improve our understanding of regional and local crustal deformation.

## Chapter 2

# Building an Earthquake Catalog for the Nyainquentanglha Detachment Region in Southern Tibet, Using a New Method of Single Station Location Inversion

### 2.1 Introduction

When station coverage in a region is insufficient for the production of a reliable P-wave first motion plot, waveform modeling methods that model regional seismograms can be used to generate an earthquake's source mechanism. Such methods had their start in the early 1990s with the development of modern broadband instrumentation which would allow the study of long and short period responses (*Kanamori et al.*, 1992). Initial difficulties in separating faulting information from wave propagation effects within broadband records led to removal of the shorter period body waves during the inversion process (*Thio and Kanamori*, 1992; *Romanowicz et al.*, 1993; *Ritsema and Lay*, 1993). These methods, which used surface waves with periods of 5s to < 50s, worked best when azimuthal coverage was good and the signal to noise ratio was low. Difficulties experienced in the inversion of stronger low period surface waves led to the development of a waveform modeling method in which only body waves were used (*Dreger and Helmberger*, 1993; *Fan and Wallace*, 1991). Although this method worked well enough to determine stable source orientations with a single station, higher

frequency inversions proved to be problematic.

The Cut and Paste (CAP) waveform modeling method, detailed in *Zhao and Helmberger (1994)* and *Zhu and Helmberger (1996)*, was developed in an effort to maximize the benefits and minimize the limitations of using long and short period portions of broadband records. This waveform modeling method performs source mechanism inversions by dividing the seismogram into body wave and surface wave segments and then searching for each segment's best fitting synthetic waveform, while allowing differential time shifts between the synthetic and the seismogram segment. Splitting the seismogram into segments greatly reduces sensitivity of the inversion to the timing between crustal arrivals, and thus makes it possible to generate accurate source mechanisms with less than perfect Green's functions. The CAPloc method, developed in *Tan et al. (2006)* takes CAP one step further by including an inversion for the location of the event. This location inversion requires the calibration of regional paths and has been successfully implemented in Tibet and Southern California, where such calibrations have been performed (*Zhu et al., 2006; Tape, 2009*).

Both CAP and CAPloc allow for source inversion with a minimal number of stations, and accurate mechanisms have been obtained using as few as two. *Tan et al. (2006)* proved the effectiveness of the new CAPloc method by comparing the inversions performed using two Tibetan stations (LHSA and TUNL) 500 km away from each other with inversions performed using the whole PASSCAL array, present in central Tibet from 1991 to 1992. *Tan et al. (2010)* obtained a similarly impressive result in Southern California when inverting for the source mechanisms of historical events using stations PAS and GSC. CAPloc, when run with a single station and a fixed source mechanism, can obtain a location, but this location will have a wider range of azimuthal uncertainty (*Wei et al., 2009, unpublished manuscript*). If velocity structure is well constrained, CAP and its long period body-wave inversion predecessor are both able to perform inversions that obtain accurate source mechanisms with as little as one station (*Dreger and Helmberger, 1993*).

One station CAP could be very useful in determining focal mechanisms of earthquakes that occur in regions with low broadband seismic station coverage. In these regions, only moderate to large sized earthquakes, which can be recorded by global networks, are widely studied, and any investigation

into smaller earthquakes' mechanisms and locations is nearly impossible. In an effort to improve our ability to locate earthquakes in regions of sparse station coverage, we have worked to develop a new single station earthquake location method dubbed the SP Envelope method. This method calculates the location of an earthquake by first determining the optimum azimuthal location by finding the smallest envelope of the P-arrival on the record's T-component then determining the radial distance from the difference between S and P-arrival times. This method, when used in conjunction with CAP, allows for the determination of a source's mechanism, depth, magnitude, and location once the most likely azimuth is known.

In order to test the efficacy of this new method, we performed a study of small to moderate sized earthquakes in the Yadong-Gulu Rift of Southern Tibet (figure 2.1). An earthquake swarm occurred within the rift between 2002 and 2003 and was only recorded by the nearby ( $\sim 75$  km away) broadband station at Lhasa (LHSA). The 2008  $M_w$ 6.3 Damxung earthquake and its aftershocks occurred in the same region as the swarm. This later sequence of earthquakes was not only recorded by LHSA, but also by five local Chinese stations. By comparing CAPloc results obtained using records from these five stations to source mechanism and location results obtained by applying CAP and SP Envelope to records from LHSA, we are able to determine that the new combined method is very effective at calculating earthquake source characteristics. Further comparison of geodetic and INSAR inversions of the Damxung earthquake to our single station inversion result, also supports the efficacy of our new combined method. Using CAP along with the SP Envelope method, we compile an earthquake catalog of the 2002-2003 swarm and 2008 mainshock and aftershock series which can be used in future studies of faulting and crustal deformation within the Yadong-Gulu Rift.

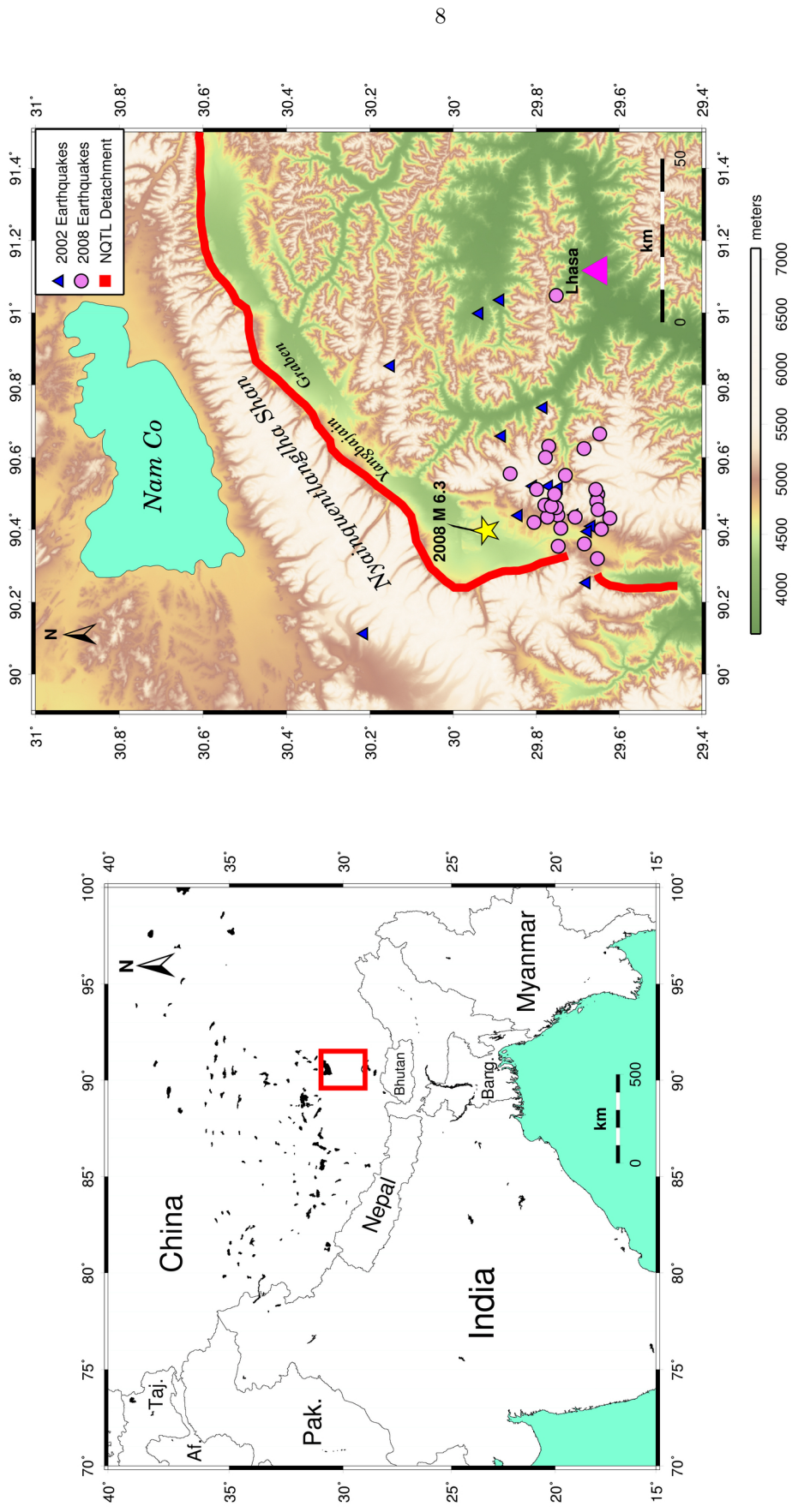


Figure 2.1: Yadong Gulu Rift and surrounding area. Locations obtained from the ISC and the map of the NQTL found in *Deng et al. (2003)* are shown. The Yangbajain Graben or Valley bounds the NQTL to the southeast.

## 2.2 Single Station Earthquake Location—The State of the Art

In methods of single-station earthquake location, azimuth is most often determined from polarization analysis or on artificial-intelligence based pattern-recognition methods (*Dai and MacBeth*, 1995, 1997; *Zhizhin et al.*, 2006; *Frohlich and Pulliam*, 1999; *Agius and Galea*, 2011). These polarization analysis methods determine the location of earthquakes by first using a three-component broadband signal to build a data covariance matrix. The largest eigenvalue of this matrix and its associated eigenvector define the azimuth (*Agius and Galea*, 2011). (*Magotra et al.*, 1989) pioneered this method by using only horizontal components of the broadband records and *Park et al.* [1987], *Jurkevics* (1988); *Ruud et al.* (1988); *Ruud and Husebye* (1992) and *Kim and Gao* (1997) used all three broadband components. *Roberts et al.* (1989) and *Agius and Galea* (2011) demonstrated that similar azimuth values could be obtained from auto- and cross-correlation functions of the three components calculated over short time windows, thus avoiding the computationally expensive covariance matrix inversion. Azimuth determination is often quite difficult when P-wave polarization is influenced by scattering effects and signal to noise ratios are low.

Earthquake distances are easier to determine than azimuths. Phase arrivals and their separations along with travel time tables and estimates of slowness allow distances to be quickly calculated (*Zhao and Helmberger*, 1991; *Dreger and Helmberger*, 1991, 1993). The only caveat is that regional crustal structure must be well constrained. In an effort to develop a better earthquake early warning system using a single station, *Lockman and Allen* (2005) determined distance by developing a scaling relationship between P-wave amplitude and period and an earthquake's hypocentral location.

## 2.3 Previous Studies of Tibetan Seismicity

Because of sparse coverage of broadband stations, most previous studies of Tibetan seismicity have focused on teleseismic data or data acquired from temporary arrays. *Molnar and Chen* (1983) used long period teleseismic data acquired by the World Wide Standardized Seismograph Network

(WWSSN) to determine the focal mechanisms and focal depths of 16 earthquakes occurring beneath the highest elevation portions of the plateau. They found all of their earthquakes to be either strike-slip or normal events with focal depths between 5 and 10 km and with t-axes oriented to support the theory that east-west extension is dominant across the plateau. *Molnar and Lyon-Caen* (1989) also inverted teleseismic data to determine the mechanisms of earthquakes that occurred within Tibet and along its margins. They found that, where elevations are higher than 5 km, deformation is split between normal and strike-slip faulting. This split allows the east-west extension in the area to be partitioned into equal parts east-west crustal thinning and roughly north-south crustal shortening. They also note that the seemingly random locations of normal and strike-slip faults supports the idea that Tibet is split up into many small discrete blocks.

In the 1990s, Project INDEPTH (INternational DEep Profiling of Tibet and the Himalayas), a multidisciplinary study of the crustal structure of the region, installed broadband and short period seismic arrays, which made it possible to study regional Tibetan seismicity at close range. INDEPTH I and II's arrays were studies located close to the Yadong Gulu Rift system. There, *Makovsky et al.* (1996) and discovered seismic bright spots, and *Chen et al.* (1996) found a region of high conductivity. Both findings are consistent with the presence of a zone of partial melting which could provide an explanation for ranges of focal depths observed in the region. The original goal of INDEPTH III goal was to image the lithosphere through monitoring teleseismic events, but many local and regional earthquakes were recorded as well. *Langin et al.* (2003) performed an extensive study of these events. They located 267 earthquakes and calculated 50 focal mechanisms. Most earthquakes were strike-slip and normal and occurred along the large grabens in the region. These events displayed east-west extension and were shallow enough ( $< 25$ ) km to support the earlier finding that a zone of partial melting is located in the upper crust. Some thrust events were also observed. The authors concluded that these earthquakes were a result of north-south shortening occurring as Tibet is being extended.

More recently, *Liang et al.* (2008), using data obtained from an array of 37 stations running from Tangra Yum Co to Yadong-Gulu Rift in southern Tibet, determined mechanism and hypocenter

locations using Hypoinverse2000 and a joint hypocenter determination method. They found that 250 of the 885 quakes observed were clustered north of the Yalu-Indus structure and west of the Pumpqu Xianza rift and were able to map crustal and upper mantle events associated with subducted lithosphere. In 2010, Elliott et al. used body wave modeling techniques to determine the mechanism of five earthquakes with  $M_w$  5.9 – 7.1 that occurred in 2008 and three other events that occurred between 1992 and 2008. Through the use of INSAR, they were able to determine fault locations and determine which of the mechanism’s fault planes represent the event. They also found that fault slip occurred on planes dipping ( $40^\circ$ - $50^\circ$  at depths of 10-15 km.

## 2.4 Data

Broadband records obtained from LHASA at Lhasa were used in all CAP inversions. Initial CAP inversions were performed using locations obtained from the International Seismological Centre (ISC) catalog. Although there were many earthquakes in the NQTL/YGR region during the time of the 2002-2003 swarm and 2008 earthquake/aftershock series, only 40 of these events were clearly recorded by LHASA. By 2008, five additional broadband stations were installed by the Chinese government. Data from these stations (LKZ, SNA, NMU, MZG, and DXI) made it possible to perform a set of multi-station inversions on seven of the largest events in the earthquake series using CAPloc.

## 2.5 Methods

### 2.5.1 Source Mechanism Inversion using Cut and Paste (CAP)

The CAP method was chosen for this study because it is excellent at inverting regional broadband seismograms for source mechanisms. This method allows us to invert short period body waves and long period surface waves separately and thus allows us to correct for imperfections propagated during the inversion process by inaccurate Green’s functions and the velocity model from which they were derived (*Zhao and Helmberger, 1994; Zhu and Helmberger, 1996*). Body waves have a smaller signal to noise ratio, whereas surface waves studies are more sensitive to subsurface structural het-

erogeneities and thus are less stable than body waves. In whole waveform inversion, the limitations of both wave types would lead to inaccuracies. CAP provides a better result than these methods because it is much less sensitive to lateral and vertical heterogeneities.

CAP inverts for a source mechanism by solving the equation  $f(t) = g(t)$ , where  $g(t)$  is a synthetic seismogram and  $f(t)$  is data. The seismogram represented by  $g(t)$  is built by convolving a trapezoid shaped source time function  $s(t)$  with sum of radiation pattern from the radial, tangential and vertical Green's functions representing the three fundamental faults – dip slip, 45° dip slip, and strike-slip – at the source location (*Zhao and Helmberger, 1994*). The synthetic seismograms are generated using the equations

$$g(t) = S(t) * \sum_{i=1}^{i=2} Q_i(t) A_{i+3}(\theta, \lambda, \delta) \quad (2.1)$$

for the radial component

$$g(t) = S(t) * \sum_{i=1}^{i=2} V_i(t) A_{i+3}(\theta, \lambda, \delta) \quad (2.2)$$

for the tangential component,

$$g(t) = S(t) * \sum_{i=1}^{i=2} W_i(t) A_{i+3}(\theta, \lambda, \delta) \quad (2.3)$$

for the vertical component.

In these equations,  $S(t)$  a trapezoidal source time function and  $Q(t)$ ,  $V(t)$ , and  $W(t)$  are the radial, tangential, and vertical Green's functions for the three fundamental faults (strike slip, dip slip, and 45° dip slip at the source's distance and depth. The radiation pattern is represented by the variable  $A_i$  and is a function of  $\Theta$ ,  $\delta$ , and  $\lambda$ .  $\Theta$  is the station azimuth minus the strike  $\theta$  and  $\delta$  and  $\lambda$  are dip and rake (*Zhao and Helmberger, 1994*).

The focal mechanism is determined by first performing a grid search over a range of strike, dip rake, and magnitude values. Next, the synthetic is shifted in time until the cross correlation coefficient between the synthetic and the data is the highest. Time shifts and cross correlation fits

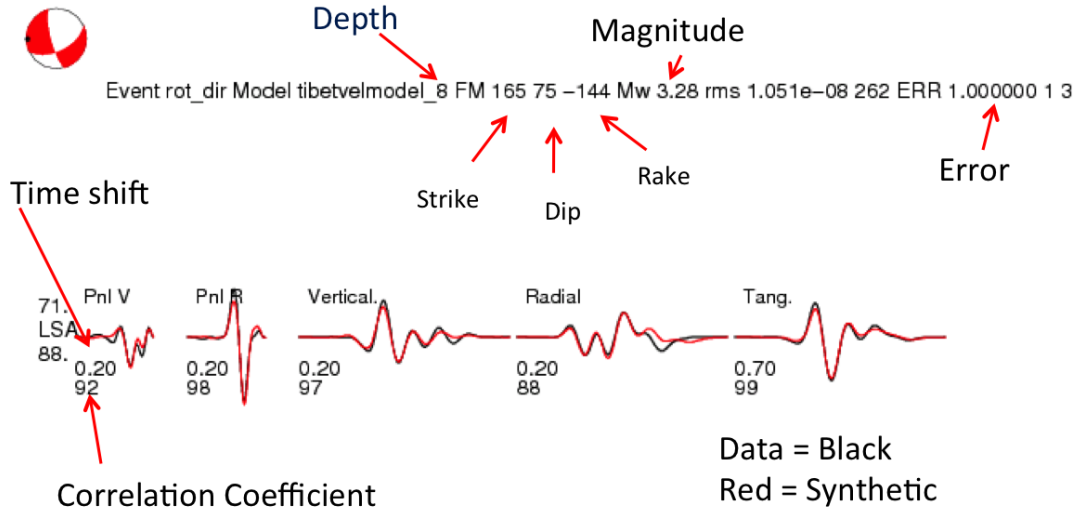


Figure 2.2: An example CAP output. The best results will have small time shifts and high correlation coefficients.

Table 2.1: Velocity Model for the Tibetan Plateau

Layer Thickness (km)	P Velocity ( $km/s$ )	S Velocity ( $km/s$ )	Density ( $g/m^3$ )	Qp	Qs
2	4.70	2.70	2.274	100	150
60	6.25	3.50	2.770	300	800
6316	8.08	4.72	3.355	700	1200

are recorded for both Pnl and surface wave portions of the record. The best location is the one with the lowest misfit error, and this low error results from the smallest time shifts and highest cross-correlation fits. Small time shifts indicate an accurate source location. The depth of the mechanism is determined by cycling through a set of Green's functions calculated for the source and velocity model. As detailed in Zhao and Helmberger [1994], event magnitude is determined from record amplitudes using the equation

$$M_0 = \text{Max}(|f(t)|)/\text{Max}(|g(t)|) \quad (2.4)$$

## 2.5.2 Preliminary CAP Results

In order to get an initial impression of source mechanism type and locations, we ran single station CAP using broadband data from LHSa at the locations obtained from the ISC catalog (figure 2.2).

We used a 1D velocity model developed in *Zhu (1998)* to perform the inversions (table 2.1). Twelve of the 40 records were noisy and were filtered using a bandpass filter between 0.2 and 2 Hz. Green's functions were built using F-K factorization and were made at 1 km intervals. Because molten crust is observed in southern Tibet beneath 30 km depth, we chose to cycle through green's functions between 1-30 km (*Langin et al., 2003*). The resulting depths are accurate to +/- 1 km. Maximum shifts for Pnl and surface waves were 5 s and 9 s respectively. The search interval within the grid search was ( $5^\circ$  for values of strike, dip, and rake and was 0.2 for magnitude. The resulting fault information is accurate to +/- ( $5^\circ$  and the resulting magnitude information is accurate to within +/- 0.2 units of  $M_w$  .

Locations provided by the ISC gave some good results (table 2.2). Most waveform components had cross correlation fits above 70 and shifts that indicated that the ISC catalog locations were < 8 km away from the actual location of the event. Considering data limitations, these results were good; however, we believe that we can only get an understanding of active faulting and deformation in the NQTL/YGR region if locations used in CAP are no more than 3-4 km away from the actual locations. We chose 3-4 km as the maximum distance because the rift valley within the NQTL/YGR region is a maximum of 15 km wide. Larger radial location uncertainties would make it more difficult for us to determine where earthquakes are occurring with respect to the rift. Only 12 of the 40 ISC locations were within this range, and thus we had to determine a method of improving earthquake locations.

Before proceeding with improving earthquake locations, we needed to be able to assess the quality of the source mechanism produced using single station CAP. We did this by comparing our results with source mechanisms inverted with CAPloc, which is detailed in (*Tan et al., 2006*). CAPloc is a version of CAP that used multiple stations to invert for the location of the earthquake as well as its strike, dip, and rake. After performing the grid search for the source mechanisms, it performs a grid search for longitude and latitude. Using records obtained from Chinese stations LKZ, SNA, NMU, MZG, and DXI, (*Wei et al., 2009*) inverted for the source mechanisms of six of the same events recorded during October 2008 at LHSA (figure 2.3). These events ranged in magnitude from

Table 2.2: Single Station CAP Results Obtained Using ISC Locations

Event Name	Longitude (°)	Latitude (°)	Depth(km)	Strike	Dip	Rake	Magnitude ( $M_w$ )	LUR (km)
20021021072337	90.1119	30.2143	7	160	90	0	2.73	26.875
20021116085221	90.409	29.667	12	200	51	-124	3.71	5
20021116093129	90.853	30.1505	7	153	90	-85	3.15	8.75
20021116094013	90.52	29.77	30	104	82	-74	4.14	7.5
20021116094453	90.48	29.768	10	181	45	-94	2.93	5.625
20021116095023	91.0352	29.8873	3	184	90	-84	2.47	11.875
20021116120308	90.9979	29.9373	9	189	30	-74	2.44	13.125
20021116180440	90.407	29.694	16	186	60	-140	3.33	5
200211291646070	90.395	29.676	9	110	44	-81	3.68	6.875
200211291729440	90.2531	29.6789	8	150	54	-177	3.37	5.625
20021130002251	90.4389	29.8433	7	103	90	-87	3.72	8.125
20021204155928	90.0122	29.3724	11	189	71	-48	3.16	8.75
20021205125840	90.7375	29.7827	4	166	90	-149	2.64	10
<b>20021216004735</b>	<b>90.5204</b>	<b>29.8081</b>	<b>5</b>	<b>140</b>	<b>75</b>	<b>-101</b>	<b>3.05</b>	<b>0.625</b>
20021216004806	90.4408	29.7082	9	190	60	-134	3.29	6.25
20031310601240	90.515	29.746	9	200	39	-138	3.42	10
<b>20081006083045</b>	<b>90.35</b>	<b>29.807</b>	<b>5</b>	<b>157</b>	<b>90</b>	<b>-148</b>	<b>5.42</b>	<b>3.75</b>
20081006084349	90.44	29.748	4	200	49	-98	3.5	13.125
20081006084505	90.435	29.773	2	142	90	-91	3.86	7.52
20081006084510	90.461	29.752	4	100	30	-85	3.85	12.5
<b>20081006085910</b>	<b>90.665</b>	<b>29.647</b>	<b>6</b>	<b>124</b>	<b>70</b>	<b>-104</b>	<b>2.91</b>	<b>0.625</b>
20081006091506	90.435	29.706	2	134	90	-82	3.41	11.75
20081006092446	90.432	29.623	2	133	90	-76	3.22	9.87
<b>20081006101306</b>	<b>90.555</b>	<b>29.863</b>	<b>5</b>	<b>115</b>	<b>68</b>	<b>-88</b>	<b>2.64</b>	<b>3.75</b>
20081006101711	90.42	29.806	7	200	35	-104	4.05	5.625
20081006111130	90.354	29.747	15	180	30	-135	3.75	5.625
20081006121033	90.32	29.653	22	159	44	-145	4.49	10
<b>20081006124653</b>	<b>90.464</b>	<b>29.764</b>	<b>7</b>	<b>200</b>	<b>34</b>	<b>-95</b>	<b>3.73</b>	<b>1.25</b>
<b>20081006141607</b>	<b>90.404</b>	<b>29.741</b>	<b>12</b>	<b>196</b>	<b>41</b>	<b>-105</b>	<b>3.19</b>	<b>2.5</b>
20081006142622	91.048	29.752	16	180	73	-15	2.33	28.75
<b>20081006190301</b>	<b>90.631</b>	<b>29.77</b>	<b>10</b>	<b>200</b>	<b>60</b>	<b>-60</b>	<b>2.81</b>	<b>3.75</b>
20081006210814	90.498	29.756	29	174	71	-175	3.04	6.875
<b>20081006231224</b>	<b>90.498</b>	<b>29.652</b>	<b>3</b>	<b>187</b>	<b>79</b>	<b>-99</b>	<b>2.88</b>	<b>0.625</b>
<b>20081009032846</b>	<b>90.361</b>	<b>29.684</b>	<b>6</b>	<b>145</b>	<b>90</b>	<b>-139</b>	<b>3.85</b>	<b>4.375</b>
20081009132830	90.624	29.685	8	114	40	-180	2.9	8.75
<b>20081009175922</b>	<b>90.478</b>	<b>29.654</b>	<b>15</b>	<b>200</b>	<b>44</b>	<b>-107</b>	<b>3.23</b>	<b>1.875</b>
<b>20081011033227</b>	<b>90.511</b>	<b>29.799</b>	<b>4</b>	<b>139</b>	<b>80</b>	<b>-109</b>	<b>3.5</b>	<b>0.625</b>
20081019190644	90.455	29.651	7	170	40	-134	3.36	5
<b>20081023130029</b>	<b>90.6</b>	<b>29.778</b>	<b>3</b>	<b>176</b>	<b>86</b>	<b>-137</b>	<b>3.02</b>	<b>1.875</b>

Source mechanisms calculated by running CAP at locations obtained from the ISC. The records of the events in bold were filtered before running CAP. LUR stands for location uncertainty range and is the radius of a circle centered that the earthquake location. It is calculated by multiplying the Pnl time shift by the P-wave velocity.

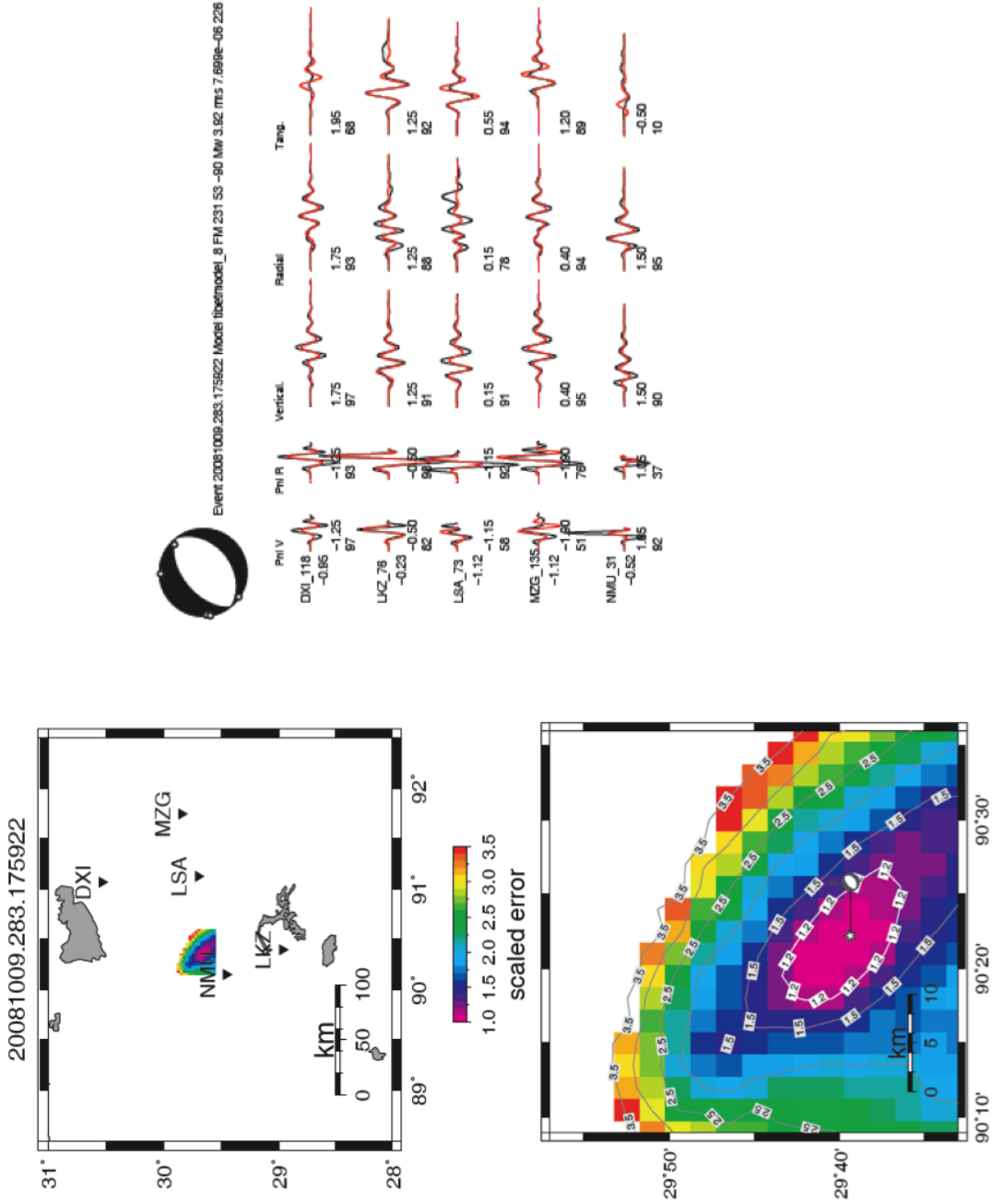


Figure 2.3: Five station CAPloc results for event 20081009175922, an aftershock of the 2008  $M_w$  6.3 Damxung earthquake.

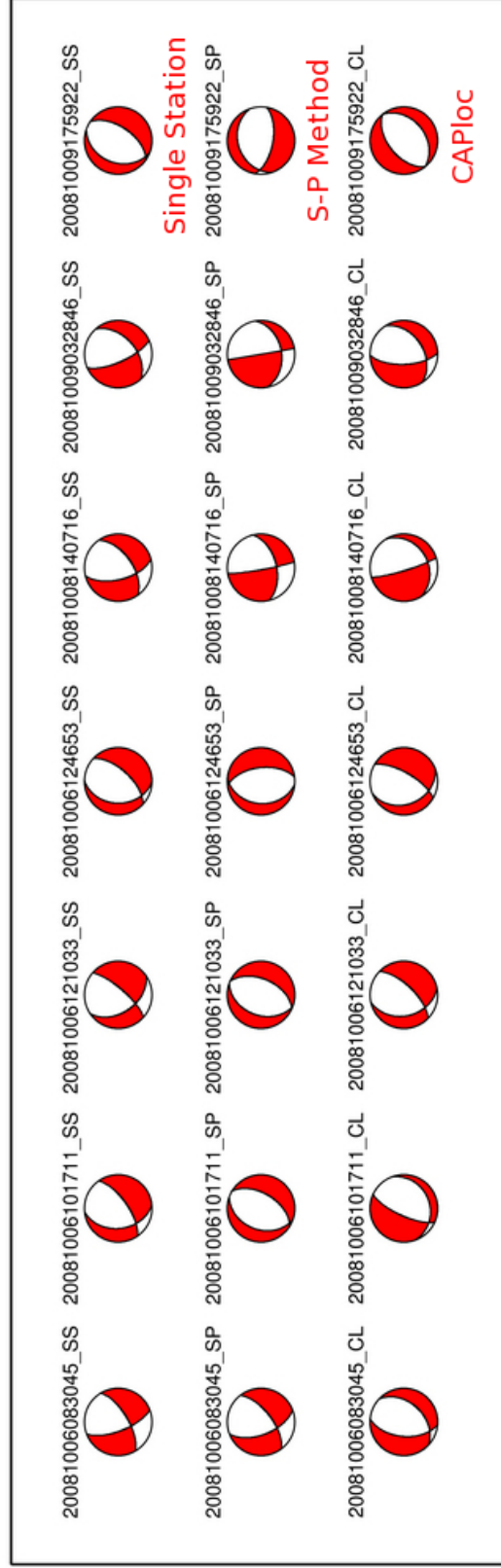


Figure 2.4: Comparison of CAP results obtained using various methods. Because CAPloc source mechanisms are obtained using information from multiple stations, it can be initially assumed that this method produces the most accurate results. The accuracy of source mechanisms produced by other methods can be assessed through comparison to CAPloc results. The average difference between strike, dip, and rake values of CAPloc and CAP run using ISC locations is  $(16.22^\circ, (13.45^\circ, \text{ and } (20.28^\circ$  respectively. When CAPloc results are compared with CAP run at locations obtained using the SP Envelope method, average differences between strike, dip, and rake values are  $(19.21^\circ, (12.61^\circ, (27.57^\circ$  respectively.

$M_w \sim 3$  to  $M_w \sim 6$ , and so were representative of the size events observed in both the swarm and the mainshock/aftershock series. Comparison of the mechanisms confirm that single station CAP does a good job of inverting for mechanisms observed in the NQTL/YGR region (figure 2.4)(table 2.3).

## 2.6 Earthquake Location Determination

### 2.6.1 SP Envelope Method

Data and station coverage limitations make single station CAP the best option for inverting for the source mechanisms of the 2002-2003 swarm and 2008 mainshock/aftershock series recorded at LHSA. While comparison of single station CAP and CAPloc results lead us to trust the accuracy of our source mechanism, the CAP time shifts suggest that the earthquake location's uncertainty is larger than we would like. For the purpose of associating source mechanisms with known faults, we would like locations with uncertainties of  $< 4$  km or Pnl time shifts of  $< 0.8$  s when P-wave velocity is 4.7 km/s and time shifts of  $< 0.8$  s when P-wave velocity is 6.25 km/s. We are less concerned with large time shifts in surface waves because the quality of their fits could be affected by shallow surface heterogeneities, but we would like to minimize these time shifts as well.

In order to improve ISC earthquake locations, we have developed the SP Envelope method. In this method, we find the great circle path between the source and station by determining optimal rotation azimuth for the data. Because we know the general location of the earthquakes in the swarm and mainshock/aftershock sequence, the  $(180^\circ)$  uncertainty in azimuth could be eliminated. As a result of this reduction of uncertainty, we could determine our final rotation azimuth by rotating broadband records to points in the western half of circle centered at LHSA. The circle contained 186 points and had a radius of 120 km (figure 2.6). At this distance, each point was approximately 3.6 km away from the next. At the distance of 78 km from  $(0.7^\circ)$  from LHSA, where many of the earthquakes' ISC catalog locations are clustered, the distance between points was 1.16 km. After rotating records recorded at LHSA, to back-azimuths corresponding to each of these points, we recorded the maximum absolute value of the P-wave arrival's envelope on the T component of the

Table 2.3: Single Station CAP Results Obtained Using Locations From All Methods

Event	Lon	Lat	Depth (km)	Strike (°)	Dip (°)	Rake (°)	Magnitude ( $M_w$ )	Method	Strike diff.	Dip diff.	Rake diff.	Mag. diff.	Depth diff.	Location diff. (km)
20081006083045	90.354	29.741	9.5	185.2	54.9	-114.2	6.19	CL5	—	—	—	—	—	—
	90.35	29.807	11.0	176.0	61.0	-60.0	5.53	ISC	9.16	6.41	54	0.66	1.5	7.339
	90.3161	29.7305	11.0	159.0	59.0	-150.0	6.77	SPE	26.16	4.41	36	0.58	1.5	4.365
20081006101711	90.452	29.727	4.8	204.4	72.4	-106.6	4.61	CL5	—	—	—	—	—	—
	90.42	29.8060	7.0	200.0	35.0	-104.0	5.36	ISC	4.42	37.41	3	0.75	2.2	9.461
	90.4764	29.7251	9.0	200.0	39.0	-94.0	5.36	SPE	4.42	33.41	13	0.75	4.2	2.717
20081006121033	90.349	29.677	9.3	168.1	37.1	-139.7	5.04	CL5	—	—	—	—	—	—
	90.32	29.6530	9.0	190.0	37.0	-109.0	4.38	ISC	21.91	0.14	31	0.66	0.3	4.178
	90.4516	29.7488	10.0	200.0	39.0	-93.0	4.39	SPE	31.91	1.82	47	0.65	0.7	13.900
20081006124653	90.370	29.65	6.5	158.8	31.5	-136.7	4.41	CL5	—	—	—	—	—	—
	90.464	29.7640	7.0	181.0	35.0	-126.0	3.74	ISC	22.17	3.53	9	0.67	0.5	16.401
	90.4577	29.5896	7.0	185.0	34.0	-80.0	5.07	SPE	26.17	2.53	57	0.66	0.5	11.820
20081008140716	90.447	29.789	5.5	163.2	82.8	-118.2	5.47	CL5	—	—	—	—	—	—
	90.3361	29.7678	11.0	166.0	61.0	-141.0	4.60	ISC	2.81	21.79	23	0.87	5.5	12.533
	90.5083	29.8631	7.0	170.0	85.0	-142.0	4.60	SPE	6.81	2.21	24	0.87	1.5	10.675
20081009032846	90.33	29.851	13.5	178.0	65.1	-125.0	4.53	CL5	—	—	—	—	—	—
	90.361	29.684	10.0	156.0	71.0	-135.0	3.86	ISC	22.04	5.90	10	0.67	3.5	18.854
	90.5261	29.9543	6.0	170.0	90.0	-129.0	3.86	SPE	8.04	24.90	4	0.67	7.5	24.602
20081009175922	90.37	29.656	7.5	231.0	53.0	-90.0	3.92	CL5	—	—	—	—	—	—
	90.478	29.654	15.0	200.0	34.0	-102.0	3.22	ISC	31	19.00	12	0.7	7.5	11.990
	90.4957	29.5724	9.0	100.0	61.0	-75.0	3.23	SPE	131	8.00	15	0.69	1.5	16.757

A Detailed comparison of source mechanisms obtained using CAPloc, SP Envelope and ISC locations. The differences (diff.) are measured with respect to CAPloc source mechanisms.



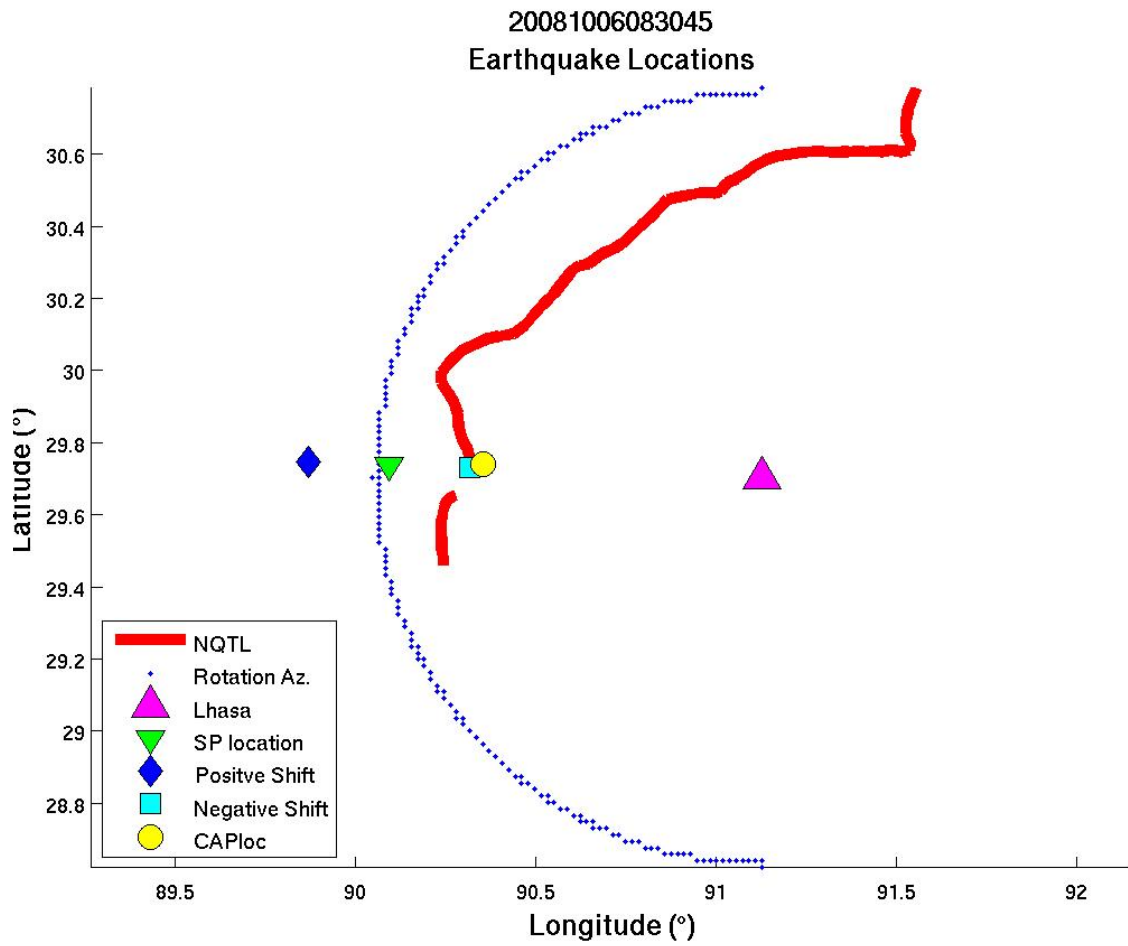


Figure 2.6: SP Envelope result for the 2008  $M_w$  6.3 Damxung earthquake. The blue dots represent the azimuths to which the records were rotated.

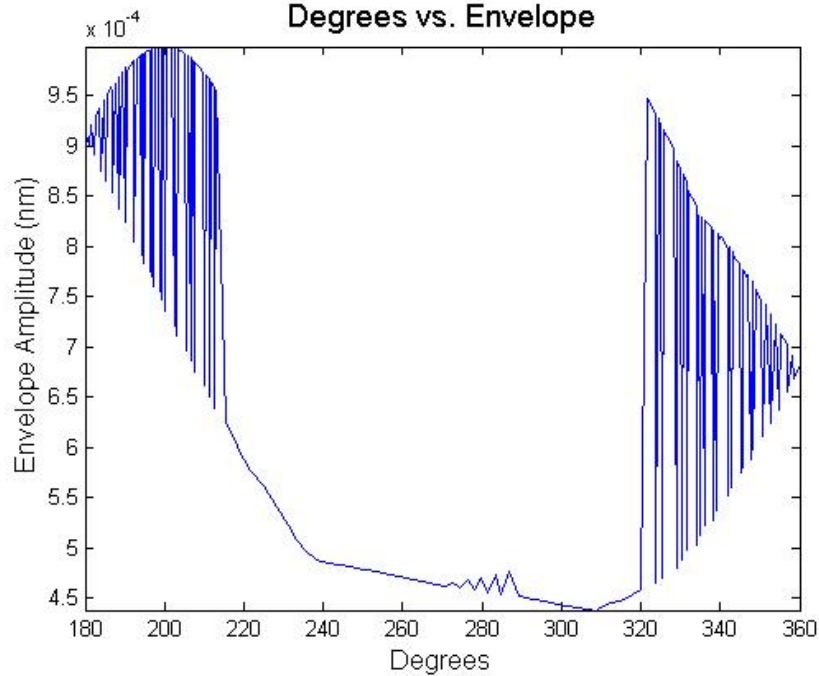


Figure 2.7: Degrees vs. Envelope Plot for the 2008  $M_w$  6.3 Damxung earthquake. The minimum T component envelope of the P-wave arrival is at  $(308^\circ)$

record. At the best azimuth, the P-wave arrival on T will be at its minimum (figure 2.7]. We then determine the event's distance from the source by measuring the time between the P-arrival and the SH arrival. The SP distance was then calculated using the equation,

$$D_{sp} = \frac{(t_s - t_p)}{(\sqrt{3} - 1)} \times \alpha \quad (2.5)$$

(Lay and Wallace, 1995). Where  $t_s$  and  $t_p$  are the S and P arrival times and  $\alpha$  is the P-wave velocity. The combination of azimuth and distance provides us with an earthquake location. From now on, we will refer to this new location as the SP location.

Large Pnl time shifts observed when CAP was run at SP locations suggested that many of the SP locations were not as accurate as we had hoped. In an effort to further improve these locations, we use the Pnl time shifts observed at the SP locations to calculate new locations at which to run CAP (figure 2.8. Since CAP time shifts at the SP location are a measure of earthquake location uncertainty, shifting the earthquake location forward and backward along the optimal rotation azimuth by the distance indicated by the SP location time shift should yield a better result. After running CAP

Table 2.4: Single Station CAP - Time Shifts and Fits from 2002-2003 Earthquakes

Event Name	Pnl V Shift	Pnl V Fit	Pnl R Shift	Pnl R Fit	V Shift	V Fit	R Shift	R Fit	T Shift	T Fit	Lon. (°)	Lat. (°)	Source
20021021072337	4.3	87	4.3	84	2.6	0	2.6	65	7.6	74	90.1119	30.2143	O
<b>20021021072337</b>	<b>-0.7</b>	<b>50</b>	<b>-0.7</b>	<b>85</b>	<b>4.5</b>	<b>73</b>	<b>4.5</b>	<b>46</b>	<b>-3.1</b>	<b>86</b>	<b>89.6726</b>	<b>30.1964</b>	<b>P</b>
20021021072337	-5	0	-5	30	7.9	66	7.9	36	5.8	88	89.9464	30.1035	SP
20021021072337	0.6	43	0.6	42	0.8	0	0.8	85	8.4	56	90.2203	30.0106	N
20021116085221	0.8	90	0.8	96	1.6	93	1.6	89	1.4	99	90.4090	29.6670	O
<b>20021116085221</b>	<b>0.6</b>	<b>88</b>	<b>0.6</b>	<b>96</b>	<b>1.6</b>	<b>98</b>	<b>1.6</b>	<b>95</b>	<b>2.2</b>	<b>98</b>	<b>90.4344</b>	<b>29.7617</b>	<b>P</b>
20021116085221	1.3	61	1.3	72	3.9	97	3.9	87	4.8	96	90.5341	29.7533	SP
20021116085221	1.1	0	1.1	29	8.1	88	8.1	80	7.5	96	90.6337	29.7449	N
20021116093129	-0.9	52	-0.9	57	0.6	75	0.6	83	-1.8	56	90.8530	30.1505	O
20021116093129	-3.3	57	-3.3	46	2.1	79	2.1	64	6.6	88	90.5864	29.6847	P
<b>20021116093129</b>	<b>0.1</b>	<b>70</b>	<b>0.1</b>	<b>82</b>	<b>1.9</b>	<b>72</b>	<b>1.9</b>	<b>78</b>	<b>6.6</b>	<b>88</b>	<b>90.5941</b>	<b>29.6850</b>	<b>SP</b>
20021116093129	1.7	79	1.7	49	2.6	83	2.6	38	6.7	90	90.6018	29.6852	N
20021116094013	1.2	40	1.2	75	9	71	9	72	5.1	98	90.5200	29.7700	O
20021116094013	-2	21	-2	90	-2.9	94	-2.9	69	-3.8	97	90.2460	29.8701	P
20021116094013	-0.9	83	-0.9	96	-2.5	88	-2.5	71	-2.3	98	90.3140	29.8572	SP
<b>20021116094013</b>	<b>-0.1</b>	<b>99</b>	<b>-0.1</b>	<b>97</b>	<b>0</b>	<b>98</b>	<b>0</b>	<b>69</b>	<b>-0.3</b>	<b>99</b>	<b>90.3820</b>	<b>29.8443</b>	<b>N</b>
20021116094453	0.9	76	0.9	91	2.7	98	2.7	89	3.7	97	90.4800	29.7680	O
<b>20021116094453</b>	<b>0.4</b>	<b>95</b>	<b>0.4</b>	<b>97</b>	<b>0.7</b>	<b>98</b>	<b>0.7</b>	<b>93</b>	<b>1.1</b>	<b>97</b>	<b>90.3954</b>	<b>29.8146</b>	<b>P</b>
20021116094453	2.6	35	2.6	31	1.5	93	1.5	57	6.6	94	90.5931	29.7845	SP
20021116094453	5	63	5	0	7.6	96	7.6	88	6	73	90.7908	29.7544	N

Table of time shifts and fits used to determine the best SP Envelope results for 2002-2003 Swarm. The source column indicates whether the location at which CAP was run was the original ISC location (O), the positive time shift location (P), the negative time shift location (N), or the SP location. The rows in bold are our choice for the best location result.

Table 2.5: Single Station CAP (Continued 1) - Time Shifts and Fits from 2002-2003 Earthquakes

Event Name	Pnl V Shift	Pnl V Fit	Pnl R Shift	Pnl R Fit	V Shift	V Fit	R Shift	R Fit	T Shift	T Fit	Lon. (°)	Lat. (°)	Source
20021116095023	3.1	52	3.1	45	7.5	81	7.5	86	3.5	54	91.0352	29.8873	O
<b>20021116095023</b>	<b>0</b>	<b>63</b>	<b>0</b>	<b>90</b>	<b>-4.3</b>	<b>78</b>	<b>-4.3</b>	<b>82</b>	<b>-0.9</b>	<b>91</b>	<b>90.5098</b>	<b>29.8077</b>	<b>P</b>
20021116095023	0.7	64	0.7	78	-3.1	85	-3.1	79	0.3	90	90.5497	29.8009	SP
20021116095023	-0.7	76	-0.7	73	2.3	88	2.3	68	2.2	89	90.5896	29.7941	N
20021116120308	-1.7	0	-1.7	92	9	83	9	90	-4.6	54	90.9979	29.9373	O
<b>20021116120308</b>	<b>0.3</b>	<b>78</b>	<b>0.3</b>	<b>90</b>	<b>-4.1</b>	<b>87</b>	<b>-4.1</b>	<b>86</b>	<b>-0.4</b>	<b>92</b>	<b>90.5319</b>	<b>29.8364</b>	<b>P</b>
20021116120308	1	83	1	84	-2.4	84	-2.4	90	1.1	90	90.5884	29.8238	SP
20021116120308	-1.8	48	-1.8	52	-0.9	81	-0.9	91	2.7	95	90.6448	29.8111	N
20021116180440	0.8	51	0.8	97	1.3	90	1.3	87	1	99	90.4070	29.6940	O
<b>20021116180440</b>	<b>0.1</b>	<b>48</b>	<b>0.1</b>	<b>97</b>	<b>0.7</b>	<b>98</b>	<b>0.7</b>	<b>95</b>	<b>2.1</b>	<b>96</b>	<b>90.4373</b>	<b>29.8199</b>	<b>P</b>
20021116180440	1.2	0	1.2	89	4.2	96	4.2	89	4.6	95	90.5283	29.8045	SP
20021116180440	1.7	49	1.7	56	7.3	92	7.3	86	6.8	97	90.6193	29.7891	N
<b>200211291646070</b>	<b>0.1</b>	<b>84</b>	<b>0.1</b>	<b>94</b>	<b>-1.3</b>	<b>88</b>	<b>-1.3</b>	<b>84</b>	<b>2.7</b>	<b>83</b>	<b>90.395</b>	<b>29.676</b>	<b>O</b>
200211291646070	0.7	59	0.7	95	0.1	81	0.1	89	4.6	90	90.4755	29.8135	P
200211291646070	1.4	74	1.4	72	3	79	3	83	7.6	89	90.5817	29.7955	SP
200211291646070	-3.5	47	-3.5	16	6.1	81	6.1	57	9	77	90.6879	29.7775	N
200211291729440	-0.9	40	-0.9	94	-2.5	95	-2.5	84	-2.8	95	90.2531	29.6789	O
200211291729440	-0.6	71	-0.6	96	-2.5	95	-2.5	85	-2.6	98	90.2823	29.8778	P
200211291729440	-0.4	15	-0.4	97	-1.3	94	-1.3	87	-1.7	97	90.3125	29.8715	SP
<b>200211291729440</b>	<b>-0.2</b>	<b>95</b>	<b>-0.2</b>	<b>93</b>	<b>-0.4</b>	<b>96</b>	<b>-0.4</b>	<b>93</b>	<b>-0.8</b>	<b>98</b>	<b>90.3426</b>	<b>29.8653</b>	<b>N</b>

Table of time shifts and fits used to determine the best SP Envelope results for 2002-2003 Swarm. The source column indicates whether the location at which CAP was run was the original ISC location (O), the positive time shift location (P), the negative time shift location (N), or the SP location. The rows in bold are our choice for the best location result.

Table 2.6: Single Station CAP (Continued 2) - Time Shifts and Fits from 2002-2003 Earthquakes

Event Name	Pnl V Shift	Pnl V Fit	Pnl R Shift	Pnl R Fit	V Shift	V Fit	R Shift	R Fit	T Shift	T Fit	Lon. (°)	Lat. (°)	Source
20021130002251	-1.3	47	-1.3	87	-0.3	74	-0.3	88	1	55	90.4389	29.8433	O
<b>20021130002251</b>	<b>-0.3</b>	<b>76</b>	<b>-0.3</b>	<b>95</b>	<b>2</b>	<b>89</b>	<b>2</b>	<b>63</b>	<b>2.3</b>	<b>95</b>	<b>90.5907</b>	<b>29.8325</b>	<b>P</b>
20021130002251	-0.2	89	-0.2	89	9	80	9	47	2.8	93	90.6057	29.8289	SP
20021130002251	-0.3	78	-0.3	90	8.6	84	8.6	28	3.2	95	90.6206	29.8253	N
20021204155928	-1.4	62	-1.4	56	-9	88	-9	83	-9	47	90.0122	29.3724	O
<b>20021204155928</b>	<b>-0.1</b>	<b>97</b>	<b>-0.1</b>	<b>97</b>	<b>2.4</b>	<b>95</b>	<b>2.4</b>	<b>80</b>	<b>1.6</b>	<b>97</b>	<b>90.5558</b>	<b>29.6062</b>	<b>P</b>
20021204155928	0.1	87	0.1	96	2.7	94	2.7	78	1.8	97	90.5634	29.6075	SP
20021204155928	0.1	93	0.1	96	3.2	89	3.2	75	2.1	96	90.5710	29.6088	N
20021205125840	-1.6	0	-1.6	75	1.7	0	1.7	80	9	89	90.7375	29.7827	O
<b>20021205125840</b>	<b>-0.7</b>	<b>87</b>	<b>-0.7</b>	<b>93</b>	<b>-3</b>	<b>73</b>	<b>-3</b>	<b>90</b>	<b>-7.7</b>	<b>96</b>	<b>90.1343</b>	<b>29.7703</b>	<b>P</b>
20021205125840	-4	19	-4	87	-4.8	51	-4.8	86	-0.3	97	90.4412	29.7495	SP
20021205125840	0.7	52	0.7	92	1.8	68	1.8	93	6.8	97	90.7482	29.7287	N
<b>20021216004735</b>	<b>-0.1</b>	<b>83</b>	<b>-0.1</b>	<b>91</b>	<b>1.7</b>	<b>97</b>	<b>1.7</b>	<b>80</b>	<b>7.2</b>	<b>79</b>	<b>90.5204</b>	<b>29.8081</b>	<b>O</b>
20021216004735	0.2	63	0.2	89	0.6	93	0.6	85	7.2	78	90.5360	29.7932	P
20021216004735	0.7	53	0.7	81	1.5	94	1.5	86	8.5	84	90.5760	29.7871	SP
20021216004735	1.3	81	1.3	75	0.1	95	0.1	73	9	78	90.6160	29.7810	N
20021216004806	1	0	1	90	2.6	94	2.6	90	2.9	93	90.4408	29.7082	O
<b>20021216004806</b>	<b>0.7</b>	<b>0</b>	<b>0.7</b>	<b>91</b>	<b>1.8</b>	<b>99</b>	<b>1.8</b>	<b>93</b>	<b>3.1</b>	<b>92</b>	<b>90.4402</b>	<b>29.7147</b>	<b>P</b>
20021216004806	1.6	22	1.6	36	6	91	6	80	6.4	93	90.5632	29.7126	SP
20021216004806	-3.6	0	-3.6	48	4.3	93	4.3	68	9	93	90.6863	29.7105	N
20031310601240	1.6	69	1.6	87	3.3	92	3.3	80	3.6	98	90.5150	29.7460	O
<b>20031310601240</b>	<b>0.3</b>	<b>92</b>	<b>0.3</b>	<b>95</b>	<b>-0.8</b>	<b>69</b>	<b>-0.8</b>	<b>90</b>	<b>-0.7</b>	<b>60</b>	<b>90.6975</b>	<b>29.1422</b>	<b>P</b>
20031310601240	1.4	71	1.4	84	2.7	74	2.7	96	2.6	60	90.7629	29.2277	SP
20031310601240	3.2	11	3.2	60	7	75	7	94	5.9	67	90.8284	29.3132	N

Table of time shifts and fits used to determine the best SP Envelope results for 2002-2003 Swarm (Continued). The rows in bold are our choice for the best location result.

Table 2.7: Single Station CAP - Time Shifts and Fits from 2008 Earthquakes

Event Name	Pnl V Shift	Pnl V Fit	Pnl R Shift	Pnl R Fit	V Shift	V Fit	R Shift	R Fit	T Shift	T Fit	Lon. (°)	Lat. (°)	Source
20081006083045	-0.6	90	-0.6	90	-0.8	90	-0.8	58	0.3	94	90.3500	29.8070	O
20081006083045	-0.5	81	-0.5	93	-0.3	96	-0.3	92	-0.6	89	90.3534	29.9338	P
20081006083045	-0.3	77	-0.3	93	0.3	97	0.3	91	0.1	88	90.3755	29.9272	SP
<b>20081006083045</b>	<b>-0.1</b>	<b>82</b>	<b>-0.1</b>	<b>93</b>	<b>0.8</b>	<b>95</b>	<b>0.8</b>	<b>93</b>	<b>0.7</b>	<b>88</b>	<b>90.3976</b>	<b>29.9206</b>	<b>N</b>
20081006084349	-2.1	58	-2.1	68	9	24	9	29	-2.3	64	90.4400	29.7480	O
20081006084349	-2.6	53	-2.6	55	-8.5	59	-8.5	25	-5.4	61	90.1631	29.6540	P
<b>20081006084349</b>	<b>-1.2</b>	<b>50</b>	<b>-1.2</b>	<b>69</b>	<b>-6.3</b>	<b>69</b>	<b>-6.3</b>	<b>46</b>	<b>-7.8</b>	<b>67</b>	<b>90.2553</b>	<b>29.6587</b>	<b>SP</b>
20081006084349	-2.8	60	-2.8	69	-8.6	33	-8.6	59	-0.3	60	90.3475	29.6634	N
20081006084505	1.6	73	1.6	86	6.8	71	6.8	63	3.2	78	90.4350	29.7730	O
20081006084505	-0.6	68	-0.6	66	-8.3	67	-8.3	63	-7.4	66	89.9931	29.5877	P
20081006084505	-3.1	29	-3.1	52	-0.5	67	-0.5	62	-1.5	82	90.1714	29.6058	SP
<b>20081006084505</b>	<b>-0.2</b>	<b>22</b>	<b>-0.2</b>	<b>79</b>	<b>4.5</b>	<b>80</b>	<b>4.5</b>	<b>75</b>	<b>1.1</b>	<b>85</b>	<b>90.3498</b>	<b>29.6240</b>	<b>N</b>
20081006084510	-2	48	-2	87	-3.5	25	-3.5	55	2.5	76	90.4610	29.7520	O
20081006084510	-0.2	76	-0.2	70	-0.9	54	-0.9	64	-2	85	90.3545	29.7030	P
<b>20081006084510</b>	<b>0.3</b>	<b>60</b>	<b>0.3</b>	<b>75</b>	<b>0.6</b>	<b>76</b>	<b>0.6</b>	<b>69</b>	<b>-2.7</b>	<b>91</b>	<b>90.3719</b>	<b>29.7030</b>	<b>SP</b>
20081006084510	0.3	73	0.3	65	-0.3	57	-0.3	58	-1.1	85	90.3892	29.7030	N
20081006085910	-0.1	51	-0.1	92	1.8	48	1.8	39	4.4	50	90.6650	29.6470	O
20081006085910	-3.9	51	-3.9	86	-7.1	54	-7.1	52	-2.5	83	90.9474	30.3430	P
<b>20081006085910</b>	<b>-1.8</b>	<b>82</b>	<b>-1.8</b>	<b>91</b>	<b>-1.1</b>	<b>54</b>	<b>-1.1</b>	<b>66</b>	<b>1.7</b>	<b>86</b>	<b>90.9848</b>	<b>30.2097</b>	<b>SP</b>
20081006085910	0.3	28	0.3	76	3	66	3	79	6	89	91.0222	30.0764	N
<b>20081006091506</b>	<b>2.5</b>	<b>77</b>	<b>2.5</b>	<b>88</b>	<b>4.3</b>	<b>54</b>	<b>4.3</b>	<b>79</b>	<b>-0.2</b>	<b>85</b>	<b>90.4350</b>	<b>29.7060</b>	<b>O</b>
20081006091506	-0.3	15	-0.3	79	6.4	71	6.4	71	2.9	89	90.5358	29.6730	P
20081006091506	1.2	0	1.2	69	2	85	2	61	6.8	86	90.6279	29.6777	SP
20081006091506	-2.1	13	-2.1	80	4.2	75	4.2	23	9	86	90.7201	29.6824	N

Table of time shifts and fits used to determine the best SP Envelope results for the 2008 mainshock/aftershock series. The rows in bold are our choice for the best location result.

Table 2.8: Single Station CAP (Continued 1) - Time Shifts and Fits from 2008 Earthquakes

Event Name	Pnl V Shift	Pnl V Fit	Pnl R Shift	Pnl R Fit	V Shift	V Fit	R Shift	R Fit	T Shift	T Fit	Lon. (°)	Lat. (°)	Source
20081006092446	2.1	62	2.1	83	3.8	75	3.8	80	0.2	81	90.4320	29.6230	O
<b>20081006092446</b>	<b>-5</b>	<b>83</b>	<b>-5</b>	<b>12</b>	<b>7.3</b>	<b>83</b>	<b>7.3</b>	<b>89</b>	<b>4.3</b>	<b>82</b>	<b>90.5883</b>	<b>29.6009</b>	<b>P</b>
20081006092446	0.4	57	0.4	35	8.5	80	8.5	86	5.4	82	90.6185	29.6066	SP
20081006092446	-4.4	17	-4.4	48	9	75	9	85	6.2	78	90.6488	29.6124	N
20081006101306	-0.6	53	-0.6	95	-0.7	82	-0.7	52	3.1	59	90.5550	29.8630	O
20081006101306	0.8	44	0.8	67	1.3	83	1.3	73	5.4	67	90.6171	29.6512	P
<b>20081006101306</b>	<b>0.1</b>	<b>85</b>	<b>0.1</b>	<b>73</b>	<b>1.1</b>	<b>77</b>	<b>1.1</b>	<b>59</b>	<b>4.8</b>	<b>75</b>	<b>90.6229</b>	<b>29.6518</b>	<b>SP</b>
20081006101306	-4.4	55	-4.4	56	1.5	82	1.5	80	5.8	73	90.6287	29.6524	N
20081006101711	-0.9	86	-0.9	97	-0.3	96	-0.3	92	-0.7	99	90.4200	29.8060	O
20081006101711	-1.6	72	-1.6	94	-2.2	98	-2.2	89	-2.2	98	90.3534	29.7293	P
20081006101711	-0.8	90	-0.8	97	-0.4	98	-0.4	93	-0.6	99	90.4149	29.7272	SP
<b>20081006101711</b>	<b>0</b>	<b>92</b>	<b>0</b>	<b>98</b>	<b>0.8</b>	<b>98</b>	<b>0.8</b>	<b>89</b>	<b>1.1</b>	<b>99</b>	<b>90.4764</b>	<b>29.7251</b>	<b>N</b>
20081006111130	-0.9	91	-0.9	97	-1.5	97	-1.5	94	-1.4	98	90.3540	29.7470	O
<b>20081006111130</b>	<b>0.6</b>	<b>83</b>	<b>0.6</b>	<b>97</b>	<b>2.2</b>	<b>96</b>	<b>2.2</b>	<b>95</b>	<b>2</b>	<b>98</b>	<b>90.4815</b>	<b>29.7906</b>	<b>P</b>
20081006111130	1.5	60	1.5	61	5.9	94	5.9	93	-1.5	65	90.5958	29.7751	SP
20081006111130	-0.4	97	-0.4	10	8.3	91	8.3	90	7.9	95	90.7101	29.7596	N
20081006121033	-1.6	60	-1.6	95	-3.5	77	-3.5	80	-3.7	96	90.3200	29.6530	O
<b>20081006121033</b>	<b>0.1</b>	<b>96</b>	<b>0.1</b>	<b>98</b>	<b>1.3</b>	<b>97</b>	<b>1.3</b>	<b>90</b>	<b>0.8</b>	<b>98</b>	<b>90.4569</b>	<b>29.7258</b>	<b>P</b>
20081006121033	1.3	64	1.3	95	4.9	89	4.9	76	3.5	98	90.5568	29.7224	SP
20081006121033	2.9	41	2.9	67	8.6	83	8.6	75	0.3	68	90.6567	29.7190	N
20081006124653	0.2	97	0.2	98	1.4	98	1.4	90	1.3	97	90.4640	29.7640	O
20081006124653	-3.6	36	-3.6	78	-7.7	93	-7.7	78	-7.3	87	90.1805	29.5235	P
20081006124653	-1.8	64	-1.8	92	-3.3	96	-3.3	87	-8.6	80	90.3165	29.5493	SP
<b>20081006124653</b>	<b>-0.1</b>	<b>98</b>	<b>-0.1</b>	<b>98</b>	<b>0.8</b>	<b>99</b>	<b>0.8</b>	<b>93</b>	<b>0.6</b>	<b>89</b>	<b>90.4525</b>	<b>29.5751</b>	<b>N</b>

Table of time shifts and fits used to determine the best SP Envelope results for the 2008 mainshock/aftershock series. The rows in bold are our choice for the best location result.

Table 2.9: Single Station CAP (Continued 2) - Time Shifts and Fits from 2008 Earthquakes

Event Name	Pnl V Shift	Pnl V Fit	Pnl R Shift	Pnl R Fit	V Shift	V Fit	R Shift	R Fit	T Shift	T Fit	Lon. (°)	Lat. (°)	Source
<b>20081006141607</b>	<b>-0.4</b>	<b>94</b>	<b>-0.4</b>	<b>97</b>	<b>-0.5</b>	<b>95</b>	<b>-0.5</b>	<b>79</b>	<b>0</b>	<b>99</b>	<b>90.4040</b>	<b>29.7410</b>	<b>O</b>
20081006141607	-3	37	-3	78	-5.9	93	-5.9	77	-5.4	96	90.2021	29.6246	P
20081006141607	5	11	5	89	6.8	89	6.8	69	-0.4	69	90.5853	29.6571	SP
20081006141607	2.7	0	2.7	6	8.3	81	8.3	85	9	73	90.9685	29.6897	N
20081006142622	-0.4	98	-0.4	46	1	0	1	92	5.7	88	91.0480	29.7520	O
20081006142622	-5	68	-5	68	-9	42	-9	74	-2.8	9	89.9697	29.7030	P
20081006142622	-3.5	53	-3.5	69	-0.8	47	-0.8	75	-7.3	72	90.2389	29.7030	SP
<b>20081006142622</b>	<b>-1.4</b>	<b>84</b>	<b>-1.4</b>	<b>94</b>	<b>-2.5</b>	<b>92</b>	<b>-2.5</b>	<b>85</b>	<b>1.2</b>	<b>90</b>	<b>90.5081</b>	<b>29.7030</b>	<b>N</b>
<b>20081006190301</b>	<b>0.6</b>	<b>87</b>	<b>0.6</b>	<b>92</b>	<b>2.4</b>	<b>76</b>	<b>2.4</b>	<b>86</b>	<b>-2.4</b>	<b>82</b>	<b>90.6310</b>	<b>29.7700</b>	<b>O</b>
20081006190301	-5	0	-5	58	-9	86	-9	83	-8.2	86	90.1960	29.9970	P
20081006190301	-2.8	48	-2.8	87	-4	82	-4	83	-9	81	90.4013	29.9322	SP
20081006190301	0.3	57	0.3	95	1.9	78	1.9	85	-3.4	75	90.6067	29.8673	N
20081006210814	-1.1	79	-1.1	96	-2.1	39	-2.1	75	-1	98	90.4980	29.7560	O
<b>20081006210814</b>	<b>0</b>	<b>91</b>	<b>0</b>	<b>97</b>	<b>1.9</b>	<b>93</b>	<b>1.9</b>	<b>78</b>	<b>1.9</b>	<b>99</b>	<b>90.5467</b>	<b>29.7030</b>	<b>P</b>
20081006210814	0.9	79	0.9	98	2.6	85	2.6	77	3.6	99	90.6159	29.7031	SP
20081006210814	1	89	1	96	1.9	44	1.9	78	3.9	99	90.6852	29.7031	N
<b>20081006231224</b>	<b>0.1</b>	<b>65</b>	<b>0.1</b>	<b>93</b>	<b>1.5</b>	<b>98</b>	<b>1.5</b>	<b>95</b>	<b>2</b>	<b>96</b>	<b>90.4980</b>	<b>29.6520</b>	<b>O</b>
20081006231224	0.2	57	0.2	90	1.7	98	1.7	95	2.2	97	90.5016	29.6818	P
20081006231224	0.5	48	0.5	87	2.9	97	2.9	91	3.1	98	90.5401	29.6831	SP
20081006231224	0.6	21	0.6	67	4.6	93	4.6	81	4.3	98	90.5785	29.6845	N
20081008140716	-1.4	69	-1.4	90	-1.7	98	-1.7	89	-1.9	97	90.3361	29.7678	O
<b>20081008140716</b>	<b>0.5</b>	<b>93</b>	<b>0.5</b>	<b>95</b>	<b>1.5</b>	<b>99</b>	<b>1.5</b>	<b>95</b>	<b>2.5</b>	<b>95</b>	<b>90.5083</b>	<b>29.8631</b>	<b>P</b>
20081008140716	0.6	83	0.6	93	2.3	98	2.3	93	4	90	90.5529	29.5652	SP
20081008140716	1.4	38	1.4	84	4.5	95	4.5	85	4.9	91	90.5976	29.8400	N

Table of time shifts and fits used to determine the best SP Envelope results for the 2008 mainshock/aftershock series (Continued). The rows in bold are our choice for the best location result.

Table 2.10: Single Station CAP (Continued 3) - Time Shifts and Fits from 2008 Earthquakes

Event Name	Pnl V Shift	Pnl V Fit	Pnl R Shift	Pnl R Fit	V Shift	V Fit	R Shift	R Fit	T Shift	T Fit	Lon. (°)	Lat. (°)	Source
20081009032846	-0.7	75	-0.7	97	-1.8	98	-1.8	84	-0.9	96	90.3610	29.6840	O
<b>20081009032846</b>	<b>0.5</b>	<b>87</b>	<b>0.5</b>	<b>94</b>	<b>2</b>	<b>99</b>	<b>2</b>	<b>96</b>	<b>3.2</b>	<b>89</b>	<b>90.5279</b>	<b>29.8922</b>	<b>P</b>
20081009032846	1.1	60	1.1	78	4.6	96	4.6	88	-1	77	90.6086	29.8668	SP
20081009032846	3.3	0	3.3	57	7.6	85	7.6	79	7.4	87	90.6892	29.8413	N
20081009132830	1.4	76	1.4	92	8.4	74	8.4	82	8	81	90.6240	29.6850	O
<b>20081009132830</b>	<b>-1</b>	<b>79</b>	<b>-1</b>	<b>88</b>	<b>0.6</b>	<b>88</b>	<b>0.6</b>	<b>72</b>	<b>4.4</b>	<b>78</b>	<b>90.5362</b>	<b>29.7731</b>	<b>P</b>
20081009132830	1.3	58	1.3	93	8.8	76	8.8	86	8.3	81	90.6355	29.7614	SP
20081009132830	-0.6	0	-0.6	68	7.3	86	7.3	81	8.4	86	90.7348	29.7496	N
20081009175922	0.3	95	0.3	98	0.5	95	0.5	73	1.1	99	90.4780	29.6540	O
<b>20081009175922</b>	<b>0.3</b>	<b>95</b>	<b>0.3</b>	<b>98</b>	<b>1.6</b>	<b>95</b>	<b>1.6</b>	<b>84</b>	<b>1.4</b>	<b>98</b>	<b>90.4957</b>	<b>29.5724</b>	<b>P</b>
20081009175922	1.6	3	1.6	48	6.2	87	6.2	85	-1.1	67	90.6162	29.5974	SP
20081009175922	1.5	20	1.5	18	8.9	83	8.9	76	2.4	71	90.7367	29.6223	N
<b>20081011033227</b>	<b>0.1</b>	<b>87</b>	<b>0.1</b>	<b>95</b>	<b>1.6</b>	<b>98</b>	<b>1.6</b>	<b>94</b>	<b>1.5</b>	<b>98</b>	<b>90.5110</b>	<b>29.7990</b>	<b>O</b>
20081011033227	0.1	83	0.1	94	1.5	98	1.5	92	-4	84	90.5372	29.5912	P
20081011033227	0.2	80	0.2	92	2.7	96	2.7	95	2	85	90.5523	29.5941	SP
20081011033227	0.4	82	0.4	93	3.6	95	3.6	90	2.7	80	90.5675	29.5969	N
<b>20081019190644</b>	<b>-0.8</b>	<b>90</b>	<b>-0.8</b>	<b>97</b>	<b>0.2</b>	<b>95</b>	<b>0.2</b>	<b>86</b>	<b>0.3</b>	<b>99</b>	<b>90.4550</b>	<b>29.6510</b>	<b>O</b>
20081019190644	-2.8	77	-2.8	73	-6.6	56	-6.6	89	-9	83	90.0806	29.8626	P
20081019190644	-3	47	-3	85	-4	93	-4	72	-3.9	99	90.3087	29.8278	SP
20081019190644	0.1	96	0.1	98	1.6	92	1.6	78	2.2	97	90.5369	29.7931	N
20081023130029	0.3	0	0.3	91	2.4	89	2.4	82	3.7	96	90.6000	29.7780	O
<b>20081023130029</b>	<b>0.1</b>	<b>58</b>	<b>0.1</b>	<b>94</b>	<b>1.5</b>	<b>86</b>	<b>1.5</b>	<b>89</b>	<b>3.3</b>	<b>90</b>	<b>90.6103</b>	<b>29.8784</b>	<b>P</b>
20081023130029	0.9	80	0.9	92	2.8	81	2.8	83	4.9	90	90.6596	29.8616	SP
20081023130029	2.1	62	2.1	82	0.9	87	0.9	65	5.6	92	90.7089	29.8449	N

Table of time shifts and fits used to determine the best SP Envelope results for the 2008 mainshock/aftershock series (Continued). The rows in bold are our choice for the best location result.

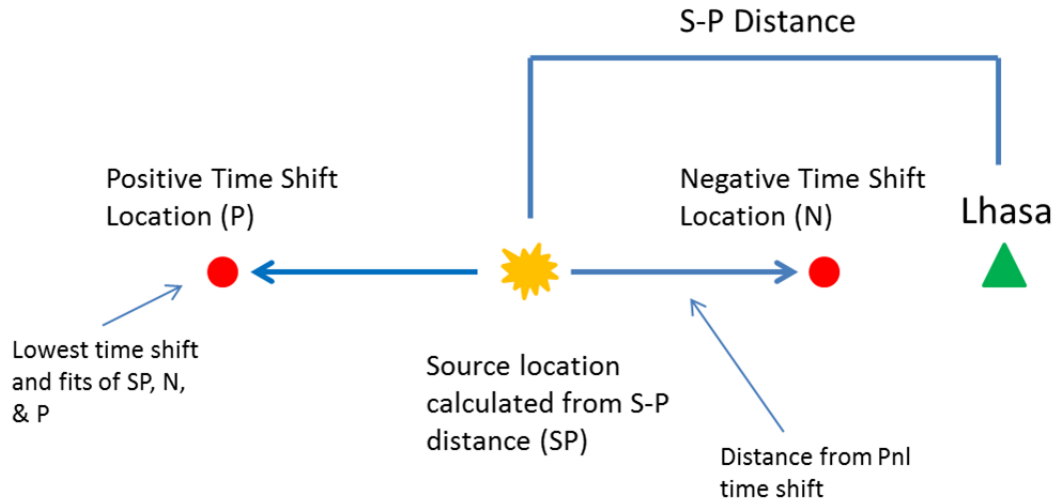


Figure 2.8: SP Envelope Method workflow.

at the forward-shifted location (P or positive time shift location) and the negative-shifted location (N or negative time shift location), we determine the best location by comparing the time shifts and fits for each component of the wave form for CAP results obtained at P, SP, N and O (original ISC) locations. The best locations were generally the ones with the lowest time shifts and highest fits (tables 2.4, 2.5, 2.6, 2.7, 2.8, 2.9 2.10). For earthquakes for which there was no location at which all time shifts were lower and all fits were higher than all others, we had to choose the best location by evaluating each Pnl and surface wave shift and fit separately. For example, in a case in which all fits for all phases were high but the time shifts were high and low, the location at which 3 or more of the 5 time shifts were lowest would be chosen as the best. In cases where all time shifts and fits were very close in quality, we chose the location with the slightly smaller time shifts. Also in these close cases, because of surface waves' possible interaction with shallow subsurface heterogeneities, locations with better Pnl shifts and fits were chosen over those with better surface wave shifts and fits.

Table 2.11: Single Station CAP Results Obtained Using Best Locations - 2002-2003 Events

Event Name	Longitude ( $^{\circ}$ )	Latitude ( $^{\circ}$ )	Depth (km)	Strike	Dip	Strike	Rake	Magnitude ( $M_w$ )	LUR (km)	Filtered	Source
20021021072337	89.6726	30.1964	11	145	90	145	0	2.61	4.375	No	P
20021116085221	90.4344	29.7617	6	195	65	195	-126	3.63	3.75	No	P
20021116093129	90.5941	29.6850	4	125	64	125	-71	2.45	0.625	Yes	SP
20021116094013	90.3820	29.8443	8	200	34	200	-130	4.59	0.625	No	N
20021116094453	90.3954	29.8146	8	195	60	195	-128	3.47	2.5	No	P
20021116095023	90.5098	29.8077	2	144	86	144	-76	2.73	0	Yes	P
20021116120308	90.5319	29.8364	2	162	90	162	-82	2.75	1.41	Yes	P
20021116180440	90.4373	29.8199	3	171	90	171	-119	3.39	0.625	No	P
200211291646070	90.3950	29.6760	9	110	44	110	-81	3.68	0.625	Yes	O
200211291729440	90.3426	29.8653	7	180	40	180	-158	4.74	1.25	No	N
20021130002251	90.5907	29.8325	8	200	41	200	-129	2.77	1.875	No	P
20021204155928	90.5558	29.6062	7	195	30	195	-101	3.13	0.625	No	P
20021205125840	90.1343	29.7703	24	135	75	135	0	3.16	4.375	No	P
20021216004735	90.5204	29.8081	5	140	75	140	-101	3.05	0.625	No	O
20021216004806	90.4402	29.7147	4	168	84	168	-131	3.27	4.375	No	P
20031310601240	90.6975	29.1422	15	155	40	155	-61	3.39	1.875	No	P

Single station CAP results obtained using best locations. These locations have been calculated using the SP envelope method or locations from the ISC. The source of the location (O,P,SP,or N) is noted in column 11. The location uncertainty range (LUR) is noted in column 9. Bolded columns indicate that the event's records were filtered before determining its source mechanism running CAP.

Table 2.12: Single Station CAP Results Obtained Using Best Locations - 2008 Events

Event Name	Longitude (°)	Latitude (°)	Depth (km)	Strike	Dip	Strike	Rake	Magnitude ( $M_w$ )	LUR (km)	Filtered	Source
20081006083045	90.3976	29.9206	10	181	61	181	-140	6.77	0.625	No	N
<b>20081006084349</b>	<b>90.2553</b>	<b>29.6587</b>	<b>18</b>	<b>125</b>	<b>86</b>	<b>125</b>	<b>-4</b>	<b>3.57</b>	<b>7.5</b>	<b>Yes</b>	<b>SP</b>
20081006084505	90.3498	29.6240	2	131	90	131	-79	3.67	0.94	Yes	N
20081006084510	90.3719	29.7030	2	139	90	139	-73	3.73	1.41	Yes	SP
<b>20081006085910</b>	<b>90.9848</b>	<b>30.2097</b>	<b>9</b>	<b>115</b>	<b>40</b>	<b>115</b>	<b>-74</b>	<b>3.02</b>	<b>11.25</b>	<b>Yes</b>	<b>SP</b>
<b>20081006091506</b>	<b>90.4350</b>	<b>29.7060</b>	<b>2</b>	<b>134</b>	<b>90</b>	<b>134</b>	<b>-82</b>	<b>3.41</b>	<b>11.75</b>	<b>Yes</b>	<b>O</b>
<b>20081006092446</b>	<b>90.5883</b>	<b>29.6009</b>	<b>3</b>	<b>118</b>	<b>86</b>	<b>118</b>	<b>-91</b>	<b>3.03</b>	<b>31.25</b>	<b>Yes</b>	<b>P</b>
20081006101306	90.6229	29.6518	2	107	81	107	-86	2.46	0.47	Yes	SP
20081006101711	90.4764	29.7251	9	200	39	200	-94	5.36	0	No	N
20081006111130	90.4815	29.7906	13	200	30	200	-123	3.72	3.75	No	P
20081006121033	90.4569	29.7258	9	195	37	195	-99	4.39	0.625	No	P
20081006124653	90.4525	29.5751	7	185	35	185	-76	5.07	0.625	No	N
20081006141607	90.4040	29.7410	12	196	41	196	-105	3.19	2.5	No	O
<b>20081006142622</b>	<b>90.5081</b>	<b>29.7030</b>	<b>2</b>	<b>135</b>	<b>90</b>	<b>135</b>	<b>-82</b>	<b>2.91</b>	<b>6.58</b>	<b>Yes</b>	<b>N</b>
20081006190301	90.6310	29.7700	10	200	60	200	-60	2.81	3.75	No	O
20081006210814	90.5467	29.7030	8	174	45	174	-164	2.98	0	No	P
20081006231224	90.4980	29.6520	3	187	79	187	-99	2.88	0.625	No	O
20081009032846	90.5279	29.8922	5	166	90	166	-124	3.86	3.125	No	P
<b>20081009132830</b>	<b>90.5362</b>	<b>29.7731</b>	<b>3</b>	<b>136</b>	<b>90</b>	<b>136</b>	<b>-99</b>	<b>3.2</b>	<b>6.25</b>	<b>No</b>	<b>P</b>
20081009175922	90.4957	29.5724	10	200	39	200	-93	3.23	1.875	No	P
<b>20081011033227</b>	<b>90.5110</b>	<b>29.7990</b>	<b>4</b>	<b>139</b>	<b>80</b>	<b>139</b>	<b>-109</b>	<b>3.5</b>	<b>5</b>	<b>No</b>	<b>O</b>
20081019190644	90.4550	29.6510	7	170	40	170	-134	3.36	1.875	No	O
20081023130029	90.6103	29.8784	2	200	81	200	-112	3.11	0.47	No	P

Single station CAP results obtained using best locations. These locations have been calculated using the SP envelope method or locations from the ISC. The source of the location (O,P,SP,or N) is noted in column 11. The location uncertainty range (LUR) is noted in column 9. Bolded columns indicate that the event's records were filtered before determining its source mechanism running CAP.

## 2.7 Results

### 2.7.1 Characteristics of Located Earthquakes

The SP Envelope method has allowed us to greatly improve the locations of earthquakes by obtaining results using single station CAP (table 2.11 and 2.12). Using the method of comparing time shifts and fits of O, P, SP, and N locations, we found that 32 of 40 picked earthquake locations were the P, SP, or N locations determined using the SP Envelope method. The original ISC locations which provided the best location results for their event were included in our final set of locations and will no longer be referred to separately.

Earlier we stated that in order to draw reliable conclusions about faulting and deformation in the region, we would need earthquake locations to be no more than 3-4 km from the actual location. In the case of CAP run at ISC locations, only 12 of 40 events have a location uncertainty range (LUR) of  $< 4.375$  km. With 33 of 40 events having a LUR of  $< 4.375$  km, SP Envelope locations are a great improvement over this result. Fifteen of these 32 have a LUR  $< 1$  km, 9 of 32 events with LUR between 1 and 3 km and 8 of 33 events with a LUR between 3 and 4.375 km. Of the 7 events with LUR  $> 4.375$  km, 5 have records which had to be filtered to make it possible to pick the arrivals needed to run the SP Envelope method. Although much care was taken to use filters which allowed arrivals to be picked correctly, filtering may have added artifacts which were incorrectly picked S-arrivals. 20081009132830 and 20081011033227, the other two events with LURs  $> 4.375$  km did not have records which required filtering. This probably resulted from P-waves interacting with small scale deep heterogeneities or in smaller arrival picking errors than those made with filtered records.

Most of the focal mechanisms calculated at the new locations were oblique slip events with normal and strike-slip components (figures 2.9, 2.10). Very few were pure strike-slip or pure normal events. There were some earthquakes which were found to have occurred in the Yangbajain Valley, but most are clustered in a region east of the valley which has not been well mapped in previous studies. There was no clear chronological trend in the location of earthquakes or types of mechanisms. Most events were quite shallow and were clustered between 2 and 10 km depth. This finding backs up previous

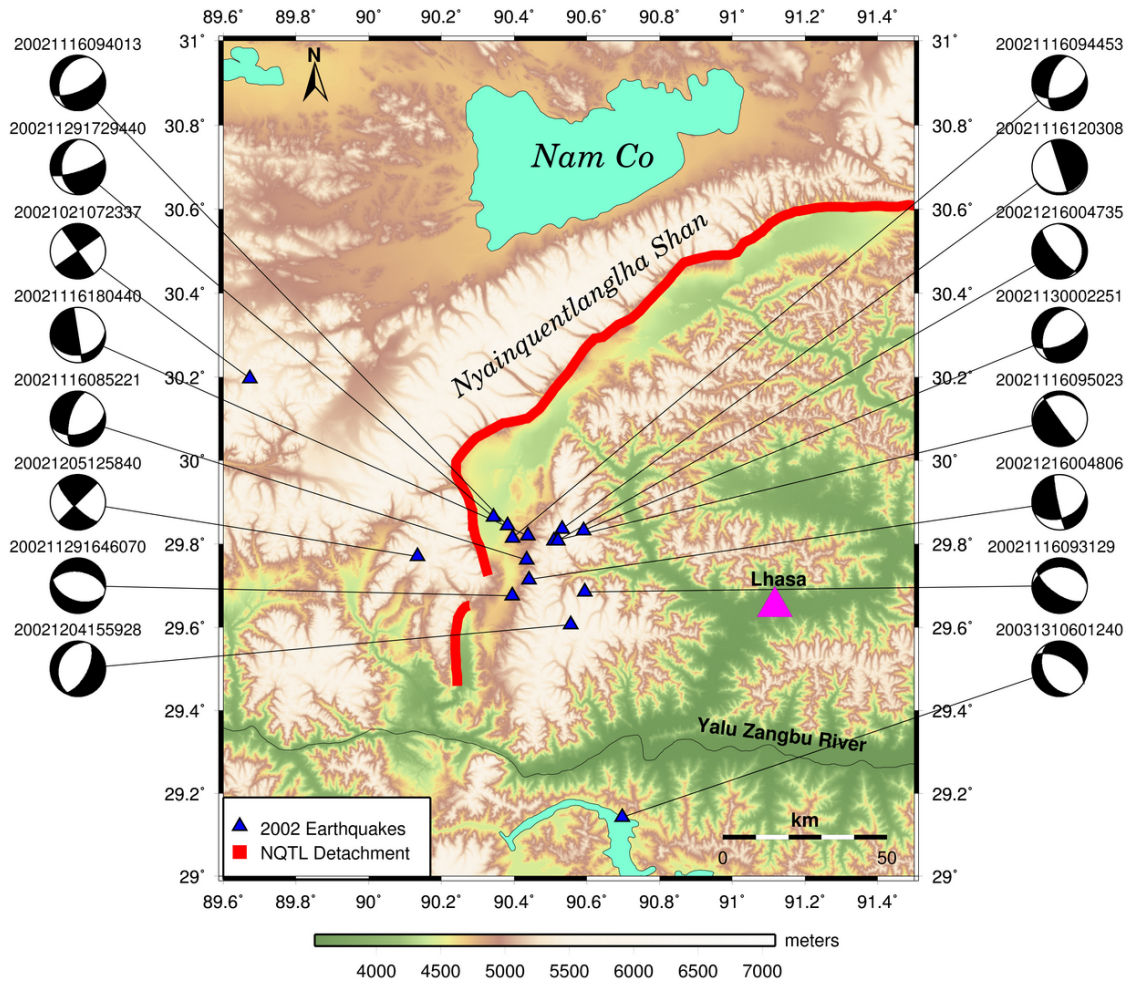


Figure 2.9: 2002 earthquake swarm locations calculated using the SP envelope method. The earthquakes occur in the Yangbajain valley and in the mountains bounding the valley. Events 20021021072337 and 20031310601240 occur far away from the rest of the swarm and thus may be unrelated.

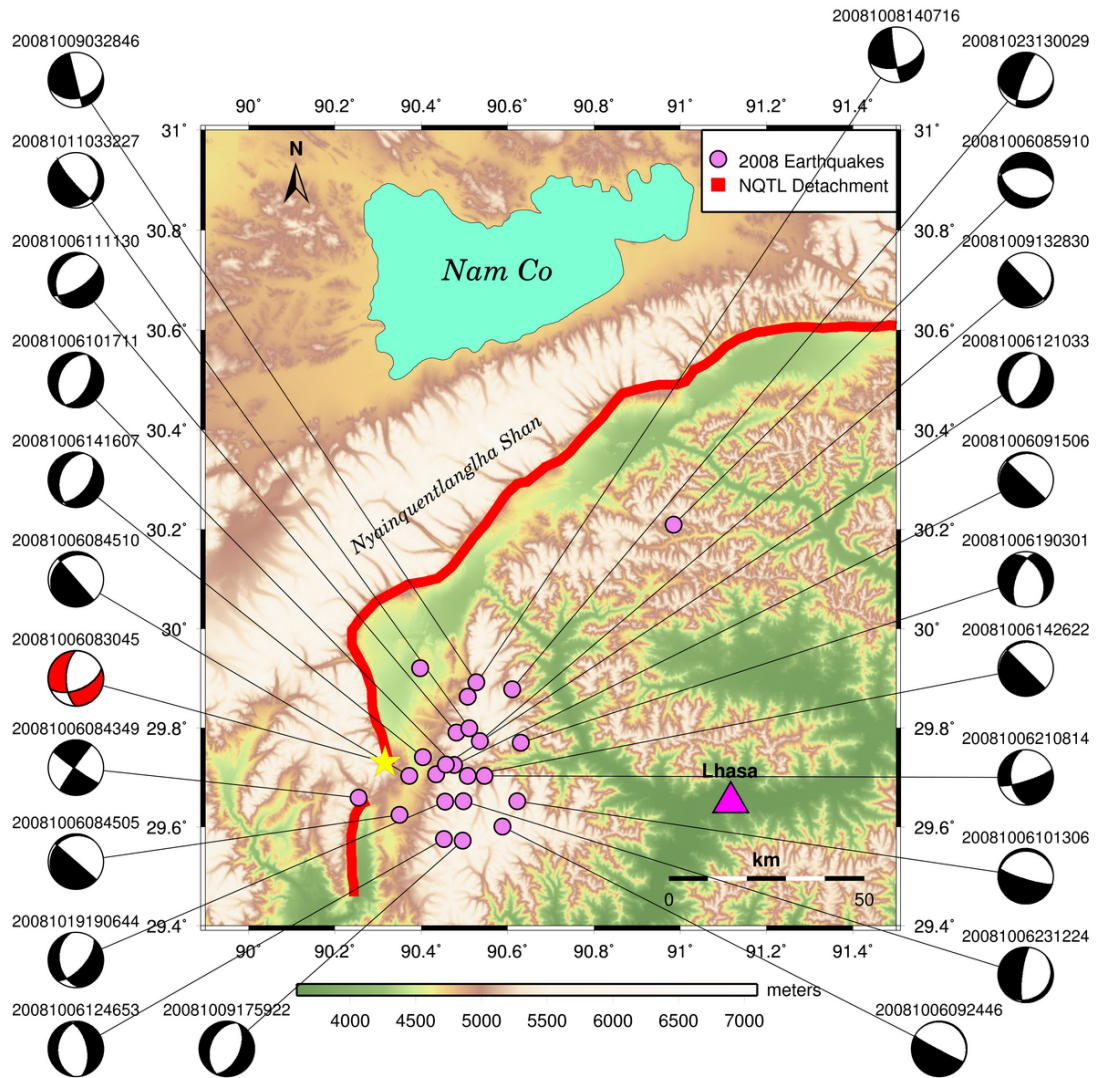


Figure 2.10: 2008 earthquake swarm locations calculated using the SP envelope method. The main shock is shown in red. These earthquakes mostly occur in the mountains bounding the east side of the Yangbajain valley, but are in the same general region as the 2002 earthquake swarm events.

studies' findings that a region of partial melting limits the seismogenic zone to the upper third of the crust in southern Tibet and that there is a zone of partial melting in the mid-crust along the NQTL where earthquakes cannot occur (*Chen and Molnar, 1981; Brown et al., 1996; Chen et al., 1996; Makovsky et al., 1996; Wei et al., 2001*). (*Langin et al., 2003*) saw very few events deeper than 25 km and we saw none. Only 6 of our events had focal depths of  $> 10$  km. The deepest one of these, 200211161205125840, had a depth of 24 km and was located far west of the rest of the swarm in the NQTL range and outside the region where partial melting had been observed. The same was true of 20031310601243, the 15 km deep event that occurred south of the Yalu Zangbo River, also far from the NQTL Range. The second deepest event, 20081006084349, was one of the filtered events whose location and CAP result could not be trusted because of possible arrival picking errors.

## 2.8 Discussion

### 2.8.1 Single-Station CAP vs. 5 Station CAPloc Mechanisms and Locations

In order to assess the accuracy of the locations and source mechanisms determined by CAP run at SP Envelope locations, we must compare the results we obtained with those obtained using 5 station CAPloc. Broadband records from Chinese stations, installed in the NQTL region before 2008, were used to perform inversions of seven of the largest events. Because the stations used in the CAPloc inversion are located in a rough circle around the locations of the NQTL swarm and mainshock aftershock series, coverage of the focal sphere was more complete (figure 2.10, table 2.13). As a result the CAPloc mechanisms are likely to be more accurate. Single-station CAP produced mechanisms that were quite similar to CAPloc (figure 2.11) (table 2.14). The differences between the strike, dip, and rake of mechanisms inverted using the two methods ranged from  $(4^\circ$  to  $(35^\circ$ . The average differences between strike, dip, and rake values are  $(19.21^\circ, (12.61^\circ, (27.57^\circ$  respectively. These values are not negligible, but they are not large enough to completely change the sense of motion represented by the source mechanism. For example, if adjustments of these magnitudes were

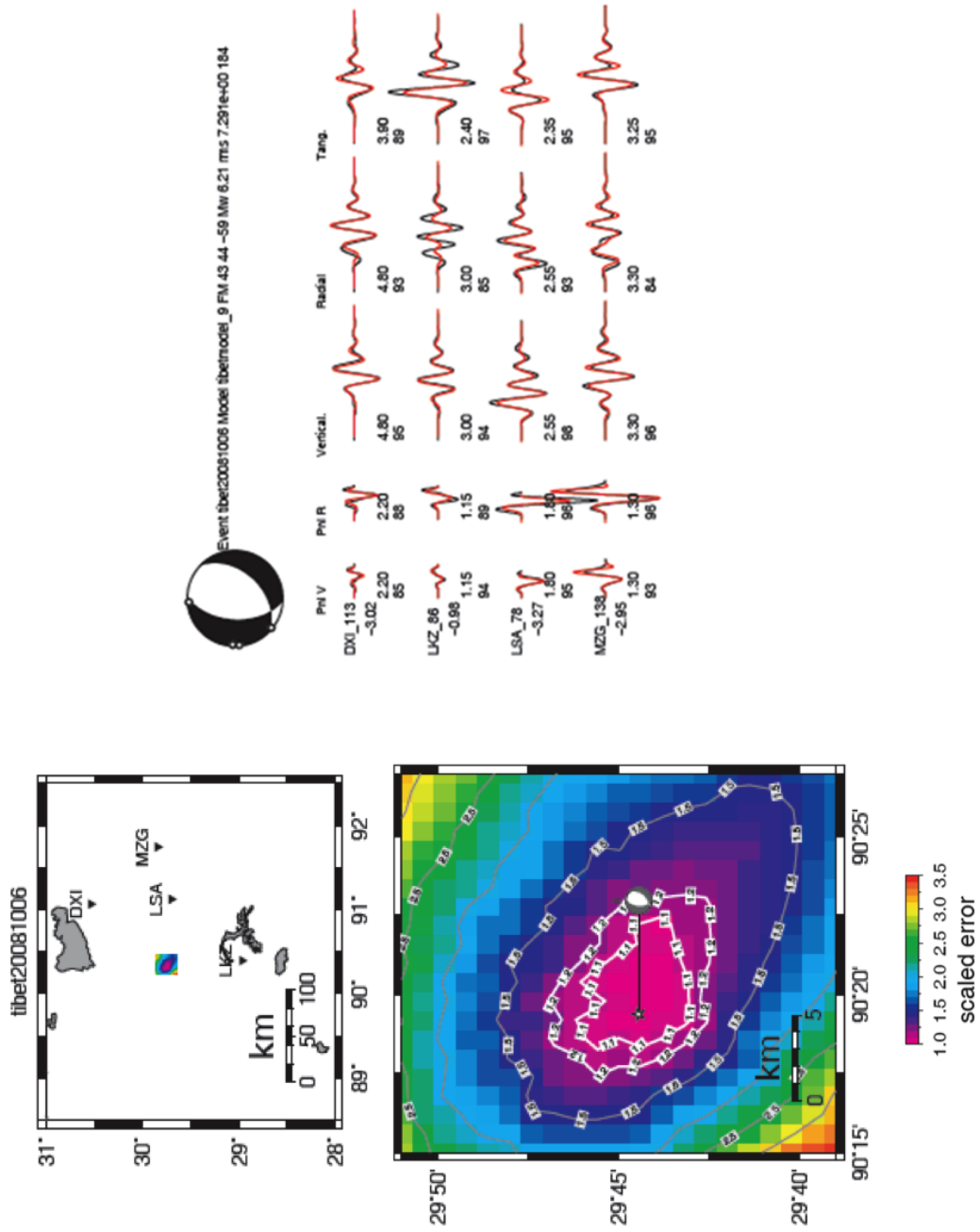


Figure 2.11: Four station CAPloc results for the 2008  $M_w$  6.3 Damxung earthquake. A map of the study area and Chinese stations and the fit error of the locations are shown on the right. Time shifts and fits are shown on the left.

Table 2.13: 10/6/2008 Damxung Earthquake Source Mechanisms and Fault Parameters

Event Name	Longitude (°)	Latitude (°)	Depth (km)	Strike	Dip	Rake	Magnitude ( $M_w$ )	Method
20081006083045	90.354	29.741	9.5	185.16	54.59	-114.24	6.19	5 Station CAPloc
20081006083045	90.3161	29.7305	11	159	59	-150	6.77	CAP/SP Envelope
20081006083045	90.43	29.76	7	185	51	-113	6.2	Elliott et al., 2010 Body Wave
20081006083045	90.43	29.76	4-11	181	47	-129 - -115	6.2	Elliott et al., 2010 InSAR
20081006083045	90.37	29.815	8.5	180	56	4	6.2	Wei et al., 2009 InSAR

Comparison of source mechanisms and locations obtained for the Damxung earthquake using the methods described in various publications.

made to the strike, dip, and rake of oblique-slip event displaying normal and strike-slip motion, the new source mechanism may appear to have a greater strike-slip or normal component, but would not be transformed into a thrust event. For this reason, we believe that we can be confident of the sense of motion represented by the focal mechanisms generated by single-station CAP.

The accuracy of the locations generated by CAPloc and the SP Envelope method can be assessed by running single-station CAP at these locations and comparing the time shifts and fits (table 2.14). The best locations generated by the SP Envelope method and CAPloc were, on average, 11.91 km apart. The best SP Envelope location produced the lowest time shifts and highest fits for 4 of 7 of the 2008 events held in common between the data sets. For 20081006083045 and 20081006101711, two events for which CAPloc produced a better location, the time shifts and fits suggest that the CAPloc location was only slightly better than the SP Envelope location. In addition, the distance between CAPloc and SP Envelope locations for 20081006083045 and 20081006101711 are 4.37 and 2.72 km respectively. The nearness of these two sets of locations reinforce the assertion the SP Envelope produces accurate locations. The only event for which CAPloc produced a location which was clearly better than SP Envelope was 20081008140716. Although the time shifts and fits were only slightly different, the distance between the two locations was 13.98 km. This large distance suggests that these small differences and time shifts and fits can occasionally represent large differences in location. The average differences between depths and magnitudes calculated using the CAPloc and SP Envelope locations were 2.34 km and  $M_w$ 0.69 respectively. The differences in depths are related to the fact that different locations produce different fit errors. The depth at which the lowest fit errors occur is the depth which is chosen for the event, and thus the differences in depths between the two methods is unrelated to the accuracy of the location. The event magnitude is calculated from the maximum amplitude of the broadband record. Because the data used in the CAPloc and SP Envelope methods were obtained from different sets of broadband stations within different networks, recorded amplitudes may be slightly different. These differences are also unrelated to the location accuracy.

Table 2.14: 10/6/2008 Damxung Earthquake - Time Shifts and Fits of all Methods

Event Name	Pnl V Shift	Pnl R Shift	Pnl R Fit	V Shift	V Fit	R Shift	R Fit	T Shift	T Fit	Lon. (°)	Lat. (°)	Source
20081006083045	<b>-0.1</b>	<b>-0.1</b>	<b>92</b>	<b>0.9</b>	<b>95</b>	<b>0.9</b>	<b>92</b>	<b>0.3</b>	<b>97</b>	<b>90.354</b>	<b>29.741</b>	<b>5 Station CAPloc</b>
20081006083045	-0.4	-0.4	91	0	94	0	90	-0.8	97	90.316	29.731	CAP/SP Envelope
20081006083045	-1.3	-1.3	0	-5.9	93	-5.9	4	6.5	71	90.43	29.76	Wei et al., 2009 InSAR
20081006083045	0.3	0.3	92	2.2	96	2.2	91	2.3	96	90.37	29.815	Elliott et al., 2010 InSAR

Comparison of time shifts and fits when CAP is run Damxung earthquake locations obtained from all methods. CAPloc produces the best result, but the SP Envelope method is a close second. The fact that these locations are only 4.37 km apart suggests that the SP Envelope method does a good job of locating earthquakes when station location is sparse.

### 2.8.2 $M_w$ 6.3 Damxung Earthquake Location from Joint Inversion of InSAR and Broadband Seismic (CAPloc)

The accuracy of the location and source mechanism of the  $M_w$ 6.3 Damxung Earthquake calculated using CAP and SP Envelope can also be assessed through comparison with the results of joint inversion of InSAR and broadband seismic data presented in *Elliott et al. (2010)* and *Wei et al. (2009)*. In *Elliott et al. (2010)*, the authors estimated the source mechanisms and fault parameters of 8 large Tibetan earthquakes through the study of teleseismic body waves and interferometric measurements. Their body wave study yielded an approximately north-south striking fault with a westward dip of  $(51^\circ)$  and a centroid depth of 7 km. The sense of motion on the fault was normal with a moderate right-lateral component. The model that best fits the slip displayed in the interferogram was also north-south striking, westward dipping fault with a component of right lateral slip. There was no surface rupture and slip occurred along a  $(47^\circ)$  dipping surface which extended from 4 to 11 km. The fault location was determined by projecting the midpoint of the best-fitting fault plane determined by InSAR, to the surface. Joint inversion of interferometric data and broadband seismic data in *Wei et al. (2009)* yielded very similar results (figure 2.12). The best fitting plane was also a north-south striking fault with a westward dip of  $(56^\circ)$  and a depth of 8.5 km. The fault plane model used to generate this result had dimensions of 16.5 km along strike and 19.5 km along dip and also did not rupture the surface.

Because the source mechanisms obtained by all five methods are quite similar, the way in which we can assess their relative quality is by determining which of their locations produces the lowest time shifts and highest fits. When run through CAP, we find that five-station CAPloc still produces the best location of the group and SP Envelope is a close second. This result supports the notion that in situations where data coverage is sparse, the SP Envelope method when used with CAP can be trusted to produce very good source mechanisms and locations.

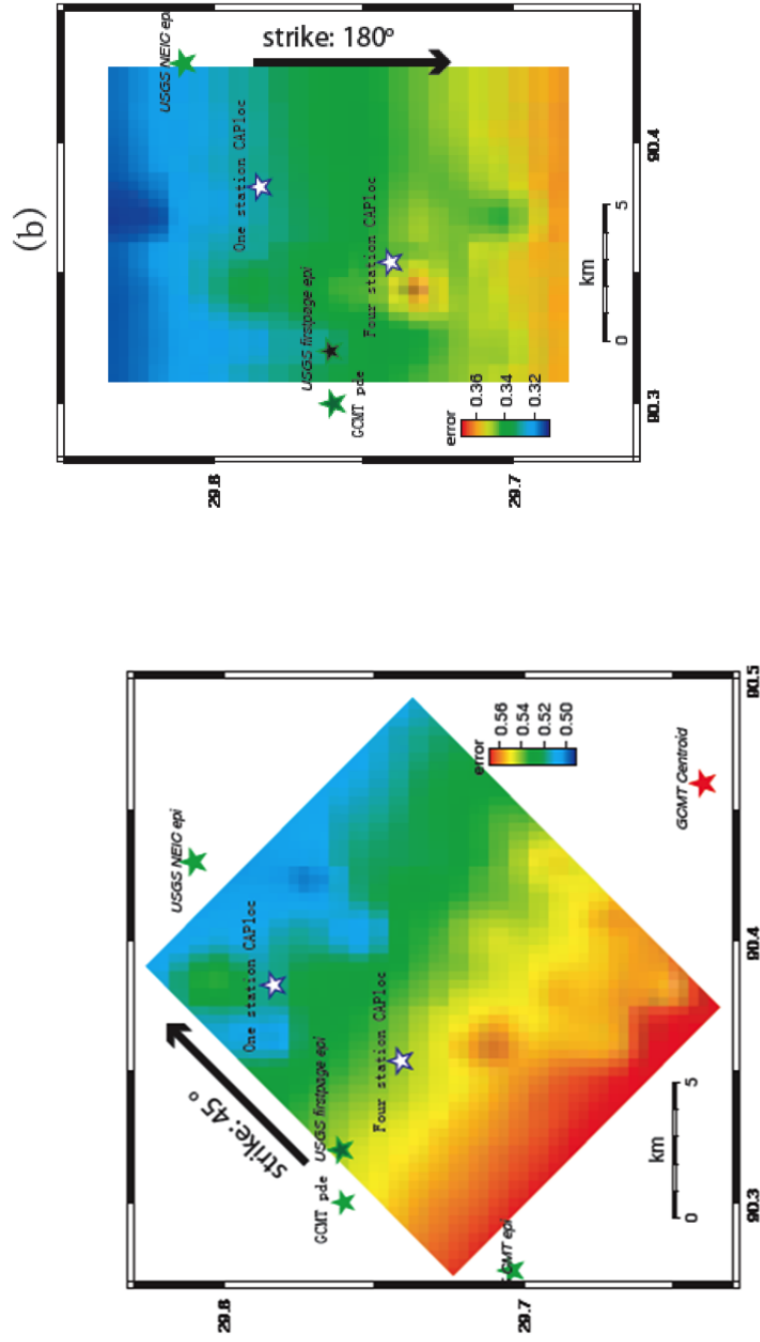


Figure 2.12: InSAR inversion results from *Wei et al.* (2009). The inversion for the 45° striking plane (right) and the 180° striking planes are shown. USGS (NEIC) and GCMT earthquake locations are shown with respect to locations obtained using 4 station and 1 station CAPloc. The errors associated with inversion on the 180° striking plane are lower than those associated with the 45° striking plane. This finding suggests that the  $M_w$  6.3 Damxung earthquake occurred on the 180° striking plane.

## 2.9 Conclusion

In this chapter we have demonstrated that a new single-station earthquake location method, SP Envelope, can be used in conjunction with CAP to produce an accurate earthquake catalog for a region with sparse broadband station coverage. When azimuth can be confidently assigned to a prior range of  $>18^\circ$ , this method allows us to determine high quality earthquake locations in regions where earthquakes are too small to be detected and located teleseismically. This joint method is especially useful in regions like Tibet, where the velocity model is well constrained.

In an effort to demonstrate the efficacy of this method, we implemented it in southern Tibet's Yadong-Gulu Rift. Only one station, LHSA, recorded both the 2002-2003 earthquake swarm and 2008  $M_w$ 6.3 Damxung earthquake and its aftershocks. The fact that the 2008 mainshock/aftershock series was covered by additional 5 Chinese stations allowed us to compare multistation CAPloc source mechanisms and locations to those calculated using single-station CAP. The similarity of the source mechanisms and the low time shifts and high fits between broadband and synthetic data suggests that the CAP/SP Envelope method works well. In the comparison of SP Envelope and CAPloc locations, there may be a positive bias given to the SP envelope locations because the method used to pick the best SP Envelope locations (assessing time shifts and fits) is the same as the method used to compare CAPloc and SP Envelope locations. This means that, because we have determined the best SP Envelope location result by comparing the time shifts and fits of multiple locations (P, SP, N, and original ISC locations) to each other, we are able to pick a result that may be better than that produced by CAPloc simply because we have more options. Although this slight positive bias exists, we believe that the SP Envelope method remains a viable and reliable option of locating earthquakes when station coverage is sparse.

The main limitation of the SP Envelope method is that it requires that the azimuth be known. This requirement restricts the method's use to regions where the general location of seismicity is well constrained. Future work should expand the method to include the automatic picking of azimuths.

## Chapter 3

# Crustal Deformation along the Nyainquentanglha Detachment Region, Southern Tibet, from Local seismicity and 3D Fault Modeling

### 3.1 Introduction

Among the most longstanding, unresolved problems in tectonics is the discrepancy between experimental and theoretical approaches to fault mechanics on one hand, and observations of crustal fault zones on the other. Experiment and theory predict that the formation and continued slip on faults occurs when the ratio of shear stress to normal stress is maximized, i.e., on planes oriented at a moderate angle ( $30^\circ$  to  $60^\circ$ ) to the principal stresses in the crust (*Scholz, 2002*). The discrepancy was first recognized in the case of thrust faulting, where intracrustal shortening is accommodated primarily on decollement planes oriented at a high angle to the least principal stress (*Hubbert and Rubey, 1959*). A more severe problem is reflected in the “stress paradox” on the San Andreas Fault. It has long been noted that the orientation of the fault appears to be at high angle to the maximum horizontal stress (*Townend and Zoback, 2004*), and that the lack of a heat flow anomaly near the fault zone indicates low shear stress on the fault (*Lachenbruch and Sass, 1988*). Mechanisms invoking high pore fluid pressure and stress rotation in the vicinity of the fault zone, accompanied by

strong spatial and temporal variations in permeability, have been proposed as possible resolutions (Rice, 1992).

Tectonic reconstructions of continental rifts over the last three decades have generally included a significant role for low-angle normal faults within the upper 15 km of the continental crust, particularly where horizontal extension is large (Davis and Coney, 1979; Gibbs, 1984; Wernicke *et al.*, 1985; Howard and John, 1987; Lister and Davis, 1989; Davis and Lister, 1988; Xiao *et al.*, 1991; Axen, 1993; Froitzheim and Manatschal, 1996; Reston, 2007; Kapp *et al.*, 2008). These faults present the same problem as the San Andreas: Even with hydrostatic pore pressure, neither initiation nor slip on planes dipping less than  $30^\circ$  is possible in materials obeying Coulombic or Byerlee failure criteria. Further, strike-slip faults and low-angle thrusts are clearly illuminated in the historic record of earthquake focal mechanisms. A number of studies have focused on data that support seismogenic low-angle normal faulting (Johnson and Loy, 1992; Abers *et al.*, 1997; Wernicke, 1995) and have inspired a generation of physical models attempting to explain low-angle normal faults and shear zones (Axen, 1992; Forsyth, 1992; Melosh, 1996; Regenauer-Lieb *et al.*, 2006).

One of the limitations of many recent studies of the origin of low-angle normal faults is the fact that the best exposed, reconstructable examples of these faults are mainly inactive. The best documented examples of active low-angle normal faults, in particular large structures with active slip that appears to be resolvably well below the  $30^\circ$  threshold for Coulombic slip in an Andersonian fault system (i.e.  $\sigma_1$  vertical), include (1) north-dipping faults in the Gulf of Corinth, Greece ( $15^\circ$  to  $20^\circ$ ; Rietbrock *et al.* (1996); Taylor *et al.* (2011)); (2) the Altotiberna detachment in the Apennine Mountains of central Italy ( $< 20^\circ$ ; Collettini and Holdsworth (2004); Smith *et al.* (2007)); (3) the Sevier Desert detachment in the Basin and Range province, western USA ( $\sim 10 - 20^\circ$ ; Allmendinger *et al.* (1983); Planke and Smith (1991); McBride *et al.* (2010)); and (4) the Nyainqentanglhe detachment of southern Tibet ( $15^\circ$  to  $37^\circ$ ; Pan and Kidd (1992); Harrison *et al.* (1995); Cogan *et al.* (1998); Kapp *et al.* (2005)).

To investigate the stress paradox as it applies to low-angle normal faults, we have chosen to study the relatively intense seismicity over the last decade associated with the Nyainqentanglhe (NQTL)

example (*Harrison et al.*, 1995; *Kapp et al.*, 2005). The Altotibernia and Gulf of Corinth detachments are associated with relatively frequent microearthquakes, some of which have been inferred to accommodate active low-angle slip (*Rietbrock et al.*, 1996; *Chiaraluce et al.*, 2007). Evidence for slip during large earthquakes with dip of  $< \sim 30^\circ$  has thus far not been observed in these areas. However, in both the Gulf of Corinth and in the D'Entrecasteaux islands of Papua New Guinea, mainshock focal mechanisms with planes dipping as little as  $20^\circ$  to  $15^\circ$  have been observed (*Rigo et al.* (1996); *Abers et al.* (1997), respectively). Near southern exposures of the NQTL detachment, a vigorous earthquake swarm, typical of Tibetan rift valleys, occurred in 2002-2003. Beginning with the  $M_w$  6.3 mainshock on October 6, 2008, the Damxung earthquake and its aftershocks occurred in the same area (*Elliott et al.*, 2010). Locations and focal mechanisms were determined for a number of events, including both the  $M_w$  2002-2003 swarm ( $M_w$  2 to 4) and the 2008 mainshock and aftershock events ( $M_w$  2 to 5.5; chapter 2). This earthquake catalog presents an opportunity to investigate the NQTL detachment from a seismotectonic point of view, in particular to assess whether any of the events occurred on the NQTL detachment plane, and to determine the state of stress in the upper crust.

### 3.1.1 Geologic Setting of the NQTL Detachment

The neotectonics of southern Tibet reflects the on-going northward movement of India into Asia, and is dominated by east-west extension (*Molnar and Tapponnier*, 1977; *Armijo et al.*, 1986; *Taylor and Yin*, 2009) which manifests itself in the form of relatively localized zones of north-trending normal faulting and related seismicity. In the southern portion of the plateau, extension is accommodated along a system of widely spaced, approximately 300 km long north-trending rift systems defined by en echelon normal faults of variable polarity (*Armijo et al.*, 1986, 1989; *Kapp et al.*, 2005). Field studies of active faults indicate that these rifts contain numerous grabens and half grabens with conjugate normal faults. Grabens generally trend north-south along the rifts, but are locally transected by strike-slip faults trending NE-SW and NW-SE (*Armijo et al.*, 1986; *Cogan et al.*, 1998).

Among the most prominent of these rift systems is the Yadong-Gulu Rift (YGR), located just west Lhasa, Tibet, and stretching from the northern margin of the High Himalaya in the south to

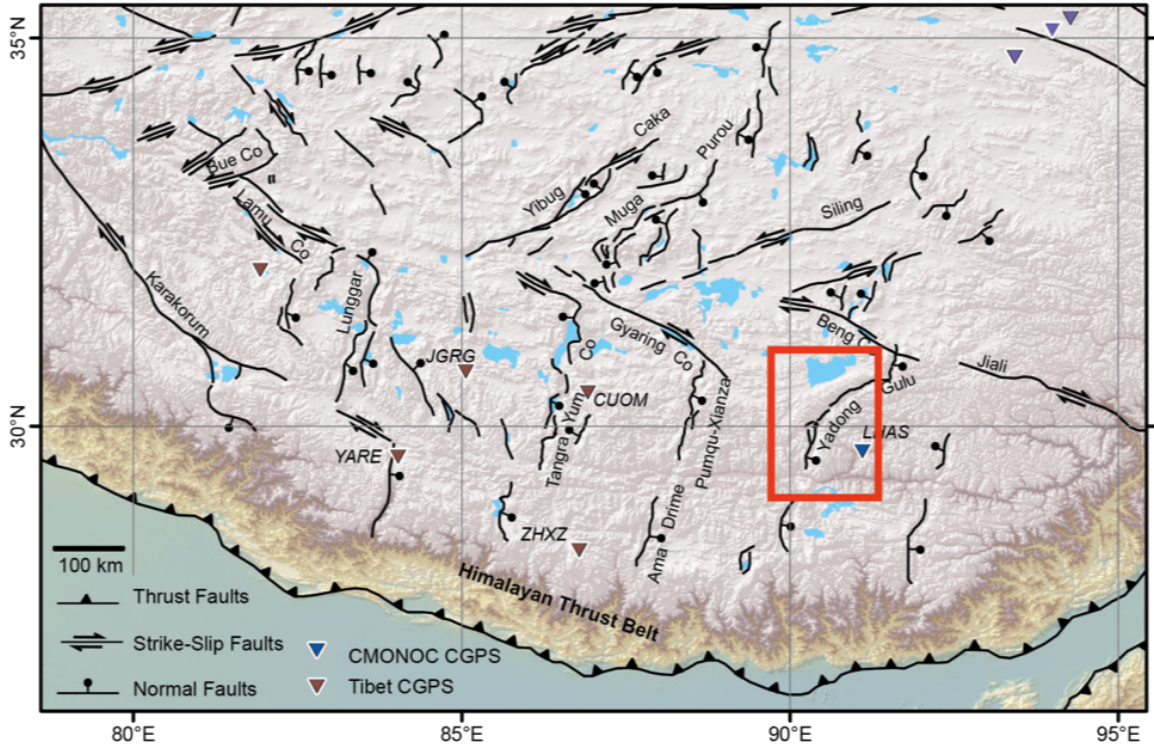


Figure 3.1: Major Tibetan Faults. The study region is located within the red box. The triangles represent the locations of cGPS stations that are currently active.

the Bangong suture zone in the north (figure 3.1; e.g. *Pan and Kidd (1992); Nelson et al. (1996)*). The Yadong- Gulu Rift is one of the rifts on which Neogene extension in southern Tibet is focused, being only one of two rifts that contain exhumed mid-crustal rocks (metamorphic core complexes), the other being the Lunggar rift of western Tibet (*Kapp et al., 2008*). The average opening rate of the YGR since 10 Ma is estimated from geochronological data to be 3 mm/yr. Relatively sparse campaign GPS coverage suggests the rate may be as great as 5 to 8 mm/yr (*Chen et al., 2004*), interpreted by some workers to be the result of the weakness due to the presence of a partially molten zone within the upper crust (*Makovsky et al., 1996; Chen et al., 1996; Kind et al., 1996; Alsdorf and Nelson, 1999*). In the northern portion of the YGR, the NQTL detachment crops out as an east-to southeast-dipping normal fault (*Armijo et al., 1986; Pan and Kidd, 1992; Harrison et al., 1995; Kapp et al., 2005*). The NQTL detachment forms the SE boundary of the NQTL Range, and forms the NW boundary of the Yangbajain-Damxung graben (YDG). Along the range front, a discrete brittle normal fault zone is roughly parallel to an extensive zone of mylonitic gneisses with shallowly

dipping foliation (*Kapp et al.*, 2005). Within the YDG, numerous faults with dips of  $> 60^\circ$  and with offsets of 10s to 100s of meters cut the alluvium and glacial till that fills it (*Armijo et al.*, 1986; *Kapp et al.*, 2005). Chloritic breccias along the fault surface, a uniform shear sense in the mylonites, strongly sheared rocks adjacent to alluvial graben fill, the similarity of orientation and kinematics of hanging wall normal faults and the NQTL detachment are all typical elements of metamorphic core complexes (*Davis*, 1983). The rapid Late Cenozoic cooling history of mylonites and ultramylonites found within the central low angle shear zone (cooling from  $> 300^\circ\text{C}$  to  $< 100^\circ\text{C}$  from 6 to 3 Ma; *Pan and Kidd* (1992)) suggest that the NQTL Range is among the youngest known metamorphic complexes on earth.

In this chapter, we examine the neotectonics and deformation of the NQTL region, comparing mapped faults and other structures with a catalog of earthquakes obtained using a waveform-modeling method called Cut and Paste (CAP), in conjunction with a new earthquake location method called SP Envelope. These techniques enable characterization of smaller events such as swarms and aftershock sequences, which would otherwise be impossible because of the sparse coverage of broadband instruments in the region. We build upon the results shown in chapter 2 which details how, when used together, CAP and the SP envelope method can be used to invert for source mechanisms and locations of small magnitude earthquakes in a region with sparse broadband seismic station coverage.

## 3.2 Data

### 3.2.1 Faults

In August 2009, approximately ten months after the October 2008 Damxung mainshock, we conducted a field reconnaissance in the epicentral region of the earthquake to search for evidence of surface rupture. We inspected most of the region of the 2002-2003 swarm, including the NQTL range front, for fresh ruptures. Interviews with local residents (largely shepherds) as to any changes in the land surface that occurred in association with the earthquake led to recognition of some small

landslides ( $< 50m^2$  in area), but otherwise there were no observed surface disturbances associated with the earthquake, in agreement the analysis of InSAR images by *Elliott et al.* (2010).

In order to understand the relationship between the earthquakes and regional faulting, we constructed a fault model using the GOCAD modeling suite. The advantage of this approach, particularly where there is significant complexity, is that the focal mechanisms can be easily visualized in three dimensions relative to both subsurface faults and to one another, to look for possible alignments. It also allows for the evaluation of whether any given nodal plane, or group of similar nodal planes, is most consistent with the overall pattern of surface faulting. The fault model contains Quaternary fault traces from *Armijo et al.* (1986); *Pan and Kidd* (1992); *Sun et al.* (2011); *Kapp et al.* (2005), which were georeferenced within ArcGIS. In an effort to supplement the sparse fault coverage afforded by these maps, we mapped shorter length faults using the satellite images within Google Earth™, which were verified by brief field reconnaissance in the summer of 2009. Faults within the southern Yanbajain Valley are relatively small but numerous, and cut Quaternary valley fill deposits. Faults within the mountains east of the valley were much more difficult to detect. The fault traces in the model were draped onto a topographic surface generated from a digital elevation model (DEM) with 90 m pixel spacing. The DEM, known as SRTM 90, is from the Space-Shuttle Radar Topography Mission (SRTM) in 2000 (*Farr et al.*, 2007).

In addition to the traces of surface faults, we have included in the fault model the subsurface projection of the NQTL detachment based on seismic imaging and interpretive cross sections of *Cogan et al.* (1998)(figure 3.2). In each one of the cross sections (figure 3.3), the location of the NQTL detachment surface trace was visible and its average dip at the surface ranges from  $22^\circ$  to  $37^\circ$  (*Kapp et al.*, 2005). The dips measured from the three interpretive sections in *Cogan et al.* (1998), based on the imaged contact between valley fill and bedrock, are somewhat shallower than the measured surface dips, at  $20^\circ$ ,  $26^\circ$ , and  $22^\circ$ , from north to south.

After georeferencing the cross section locations in ArcGIS, the NQTL detachment surface trace points were imported into GOCAD. Once within GOCAD, elevation data from the topography surface was transferred to the surface trace points. Dipping lines originating from these surface

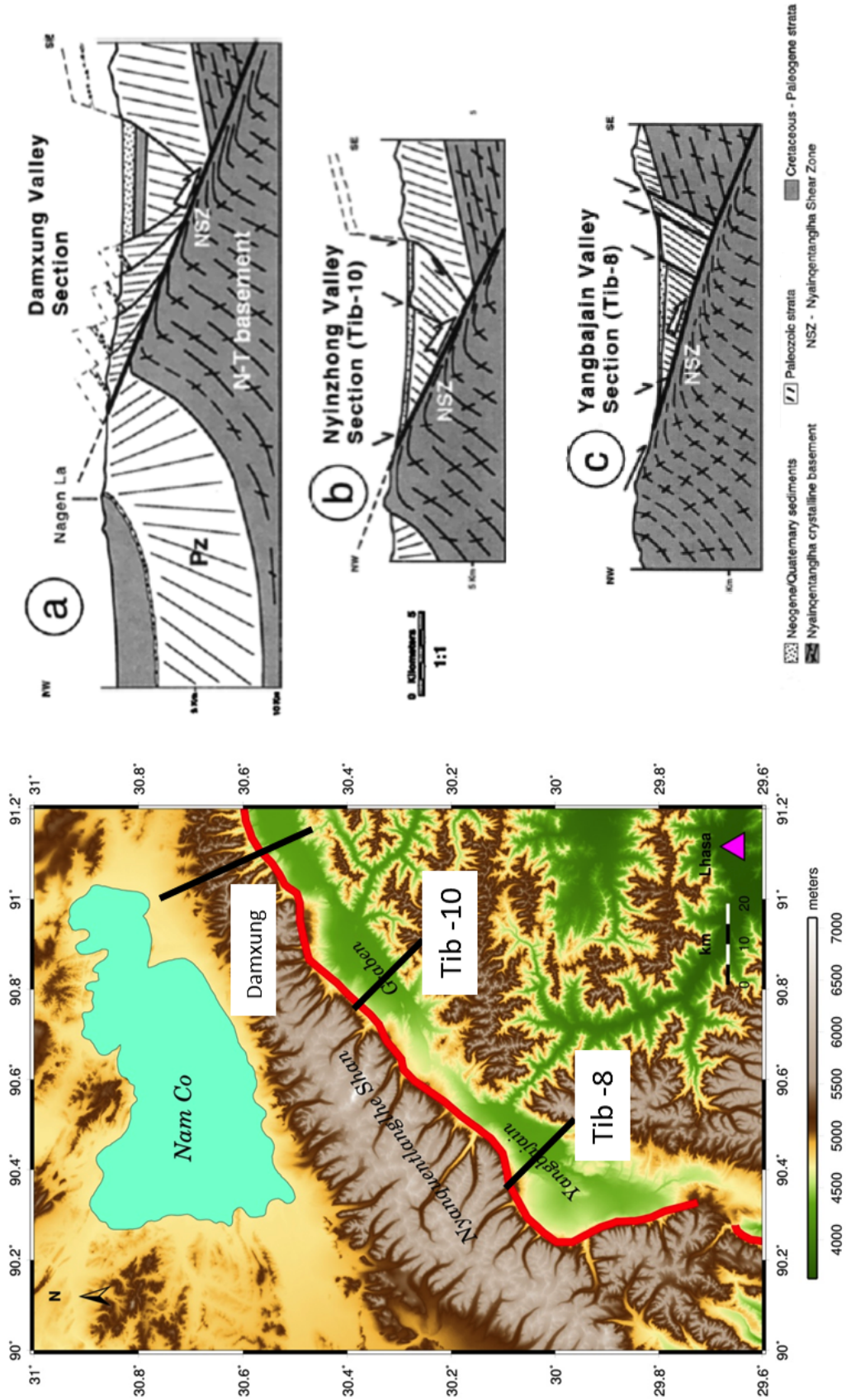


Figure 3.2: The NQTL region (left) and interpreted cross sections from *Cogan et al.*, 1998 (right). The section locations are represented by the black lines crossing the Yangbajain valley. The cross sections were generated by interpreting seismic refraction profiles across the valley. Measurements of the dip of the NQTL obtained from these cross sections were used to construct a model of the NQTL within the GOCAD 3D modeling suite.

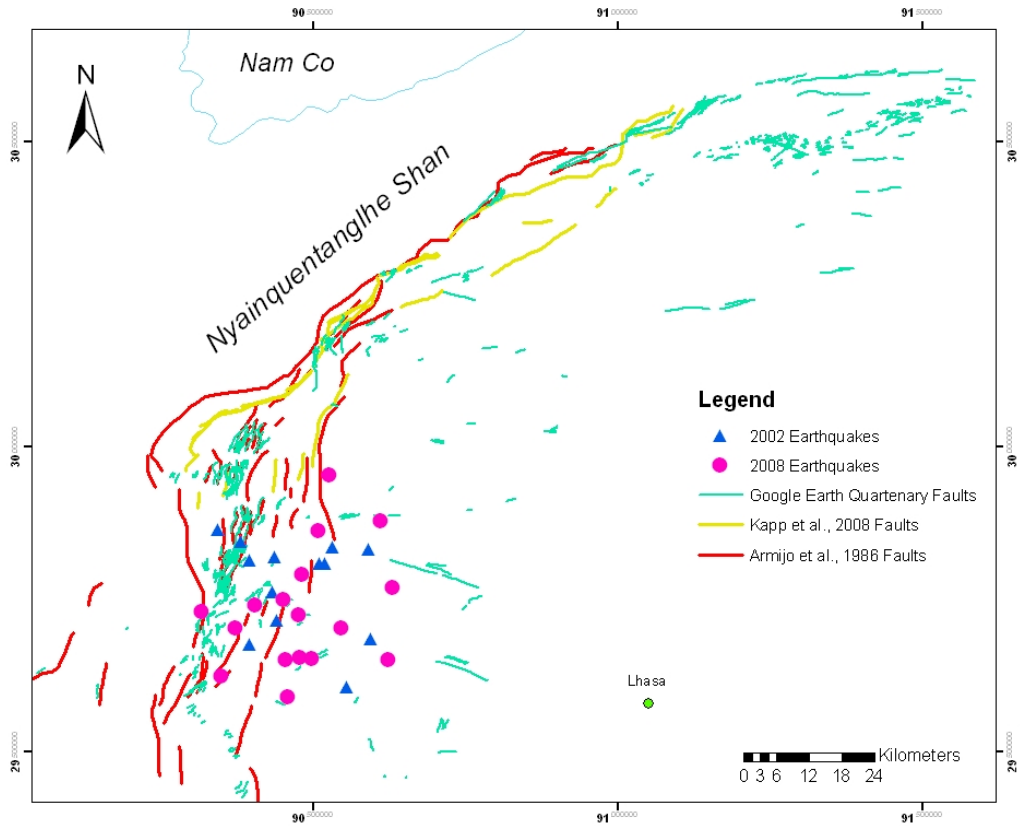


Figure 3.3: Faults in yellow and red were digitized from maps found in *Kapp et al. (2008)* and *Armijo et al. (1986)* respectively. The locations of the earthquakes contained in the low LUR catalog are shown as blue triangles (2002 events) and magenta dots (2008). The thin green faults were digitized from satellite images found in Google Earth<sup>TM</sup>.

trace points were then used to generate a simplified, multisegment surface with variable dips. We extrapolated the fault southward from the Yangbajain Valley section in *Cogan et al.* (1998), using the surface trace to constrain the strike of the fault. We built lines with the same dip as was measured at southern Yangbajain ( $22^\circ$ ) and generated a surface with a uniform dip from them that follows the surface trace. It is possible that the southward trace of the detachment differs from this value, but we presume below that it continues southward at a dip somewhere within the total measured range of dips of the detachment ( $20^\circ$  to  $37^\circ$ ).

### 3.2.2 Earthquakes

Our inversions from chapter 2 produced in a catalog of 30 earthquakes with reliable radial locations (“low uncertainty range” or LUR catalog, table 3.1), with a maximum mislocation error threshold set at 4.4 km (chapter 2, tables 2.11 and 2.12). This catalog includes 13 earthquakes from the 2002-2003 swarm (all 13 occurred in 2002) and 17 from 2008. Earthquake focal mechanisms, their fault planes, and their P and T axes were visualized within GOCAD using a plugin detailed in *Plesch* (2000). The depths of the focal mechanisms and planes are reported with respect to an elevation of 3660 m, the elevation of the broadband station LHA, at Lhasa. For each nodal plane, synthetic planar fault surfaces were constructed as 8 km squares centered on the earthquake location, so that their intersections with surface topography, surface faults, and the subsurface model of the NQTL detachment could be evaluated, so as to provide a criterion for determining which nodal plane was the most likely slip plane.

Some earthquakes, including the 2008 Damxung mainshock, have epicenters in the rift valley (Yangbajain Valley) just E of the southern NQTL Range, but most are clustered beneath uplands east of the valley, which have not been well mapped in previous studies (figure 3.1). The depth range of events is 2 to 13 km. Most of the focal mechanisms within our LUR catalog were oblique slip events with normal and strike-slip components (figures 3.3 and 3.4). Very few are pure strike-slip or pure normal events. There are no clear chronological trends in the location of events or types of mechanisms (e.g., normal mechanisms preceding strike-slip mechanisms, etc.), nor any distinction

Table 3.1: Single Station CAP Results - Low Location Uncertainty Range (LUR) Catalog

Abbrev. Name	Event Name	Longitude (°)	Latitude (°)	Depth(km)	Strike	Dip	Rake	Magnitude ( $M_w$ )	LUR (km)
S1	20021116085221	90.434	29.762	6	195	65	-126	3.63	3.75
S2	20021116093129	90.594	29.685	4	267	32	-124	2.45	0.625
S3	20021116094013	90.382	29.844	8	200	34	-130	4.59	0.625
S4	20021116094453	90.395	29.815	8	72	47	-43	3.47	2.5
S5	20021116095023	90.510	29.808	2	250	15	-164	2.73	0
S6	20021116120308	90.532	29.836	2	162	90	-82	2.75	1.41
S7	20021116180440	90.437	29.820	3	171	90	-119	3.39	0.625
S8	200211291646070	90.395	29.676	9	110	44	-81	3.68	0.625
S9	200211291729440	90.343	29.865	7	180	40	-158	4.74	1.25
S10	20021130002251	90.591	29.833	8	200	41	-129	2.77	1.875
S11	20021204155928	90.556	29.606	7	195	30	-101	3.13	0.625
S12	20021216004735	90.520	29.808	5	-3	19	-235	3.05	0.625
S13	20021216004806	90.440	29.715	4	168	84	-131	3.27	4.375
<b>D1</b>	<b>20081006083045</b>	<b>90.316</b>	<b>29.731</b>	<b>11</b>	<b>159</b>	<b>59</b>	<b>-150</b>	<b>6.77</b>	<b>0.625</b>
D2	20081006084505	90.350	29.624	2	221	11	-180	3.67	0.94
D3	20081006084510	90.372	29.703	2	229	17	-180	3.73	1.41
D4	20081006101306	90.623	29.652	2	263	10	-114	2.46	0.47
D5	20081006101711	90.476	29.725	9	200	39	-94	5.36	0
D6	20081006111130	90.482	29.791	13	200	30	-123	3.72	3.75
D7	20081006121033	90.452	29.749	10	200	39	-93	4.39	0.625
D8	20081006124653	90.458	29.590	7	-7	57	-97	5.07	0.625
D9	20081006141607	90.404	29.741	12	36	51	-77	3.19	2.5
D9.5	20081006142622	90.5081	29.7030	2	135	90	-82	2.91	6.58
D10	20081006190301	90.631	29.770	10	-29	41	-131	2.81	3.75
D11	20081006210814	90.547	29.703	8	73	79	-46	2.98	0
D12	20081006231224	90.498	29.652	3	47	14	-51	2.88	0.625
D13	20081008140716	90.508	29.863	7	170	85	-142	4.6	3.125
D14	20081009032846	90.526	29.954	6	170	90	-129	3.86	3.125
D15	20081009175922	90.478	29.654	8	200	34	-102	3.23	1.875
D16	20081019190644	90.455	29.651	7	42	62	-60	3.36	1.875
D17	20081023130029	90.610	29.878	2	200	81	-112	3.11	0.47

Low location uncertainty range (LUR) earthquake catalog. This catalog contains NQTL region earthquakes with LUR < 4.375. The  $M_w$  6.3 Damxung earthquake is in bold.

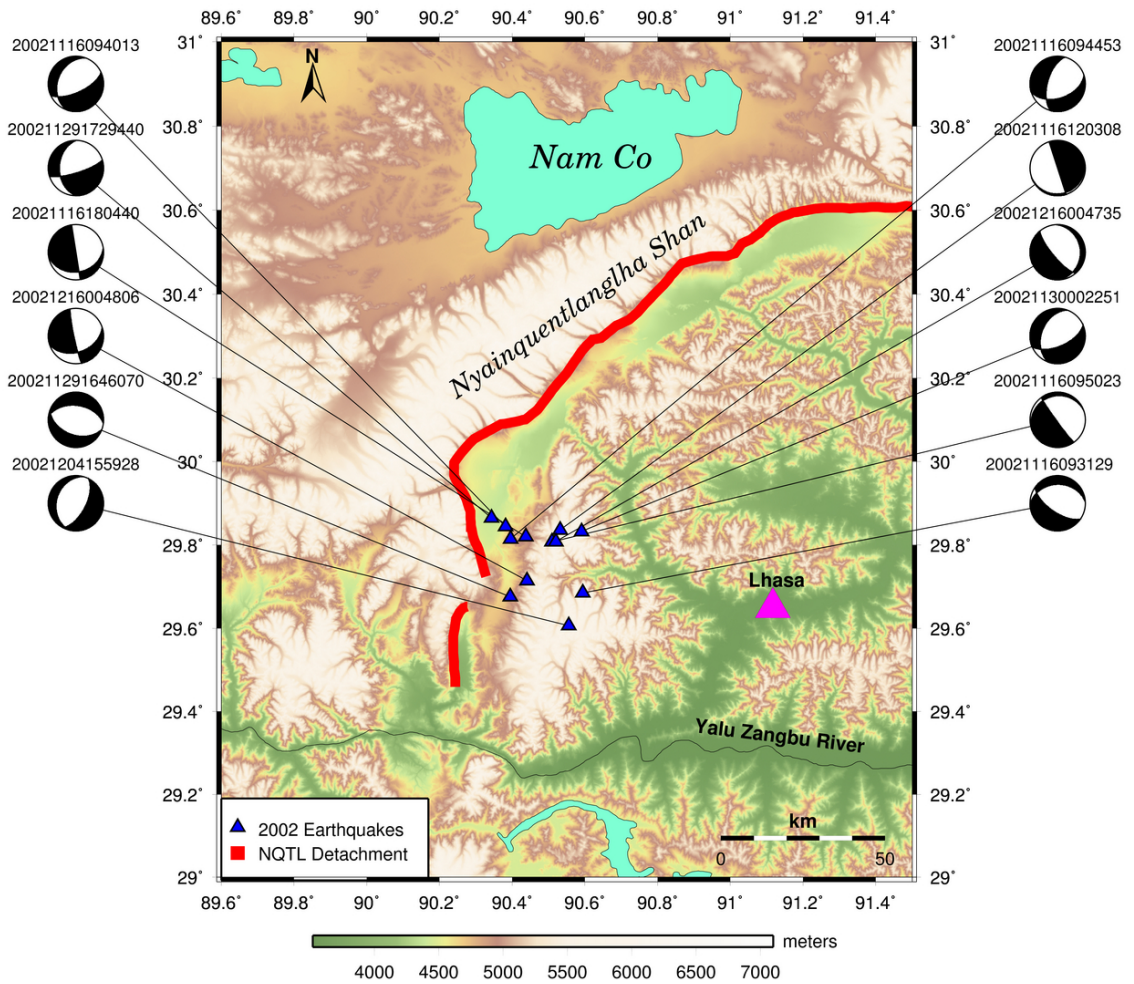


Figure 3.4: Low LUR events from the 2002-2003 earthquake swarm. All events pictured occurred in 2002.

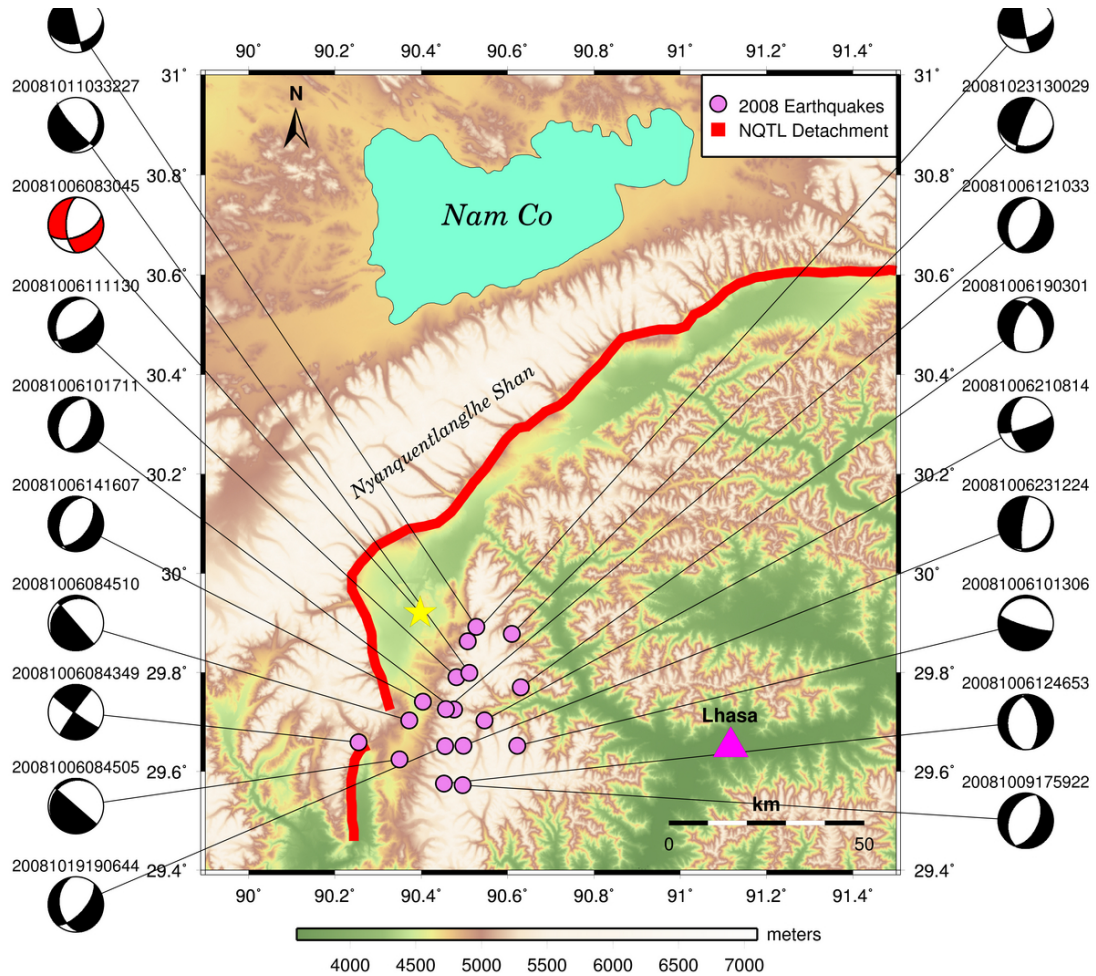


Figure 3.5: Low LUR events from the 2008 mainshock and aftershock sequence. The mainshock location is represented by the yellow star.

between the distribution and mechanisms of the 2002 and 2008 events, except that the five deepest events (10-13 km) occurred in 2008, including the mainshock at 11 km depth (Table 3.1, figures 3.3 and 3.4).

### 3.3 Analysis

#### 3.3.1 Defining Active Faults Using Alignments of Similar Focal Planes

The mechanisms fit our general expectation of east- to east-southeast extension and associated strike-slip faulting. To first order, the swarm events and the aftershocks fill a large volume of crust (most of them within a 40 km by 40 km by 13 km volume), rather than clustering along the

plane of the mainshock, the subsurface trace of the NQTL detachment, or some other planar zone (figure 3.5). Most are located in the area of the  $20^\circ$ -dipping projection of the detachment, but do not have shallowly east-dipping nodal planes that would align with the fault (figure 3.6). For the relatively shallow dip ( $20^\circ$ ), most events lie below the fault plane, including the  $M_w$ 6.3 2008 Damxung mainshock, which lies  $> 10$  km below the detachment plane. The likely fault plane for the mainshock strikes  $159^\circ$  and dips  $59^\circ$  to the west. This orientation is consistent with the best fit plane ( $180^\circ$  strike,  $56^\circ$  dip) obtained from joint inversion of INSAR broadband seismic data discussed in chapter 2.

Based on the complex distribution of events and mechanisms (figures 3.2 and 3.3) it is not obvious that any of them bear a clear relationship to surface faulting, and as shown below, it appears that many of the events, including the 2008 Damxung mainshock, define previously unknown active faults in the subsurface (*Elliott et al.*, 2010). In order to better define the overall structural geometry and kinematics at depth, we have attempted to group events with similar mechanisms and locations, and then use GOCAD visualization to “fly through” the data set to determine if there are sets of events that define a subsurface fault plane, and evaluate any potential relationship with surface faulting. Based on analysis earthquake locations and mechanisms on maps and in GOCAD, we have identified four groups of earthquakes with similar mechanism and locations (figures 3.5 and 3.7). We will refer to the events below by sequence (swarm or Damxung mainshock) and order within the sequence (table 3.1), such that “S5” refers to the 5th event determination during the 2002-2003 swarm, “D3” is the third event in the 2008 Damxung sequence, etc.

The first group includes two aftershocks, events D2 and D3, under the southern Yangbajian Valley, which appear to define a shallowly NW-dipping, left-lateral oblique-slip fault (figure 3.7A). These earthquakes occurred within 5 seconds of each other the same day as the mainshock, have nearly the same mechanism, and occur at very shallow depth (2 km). Two very similar events (D9.5 and S5) are located on the western edge of the range to the west (figure 3.7A). They are also very shallow (2 km), with one occurring on the same day as the mainshock, and the other in 2002. When viewed looking to the NNW of the subsurface projection of the NQTL detachment (figure 3.7B),

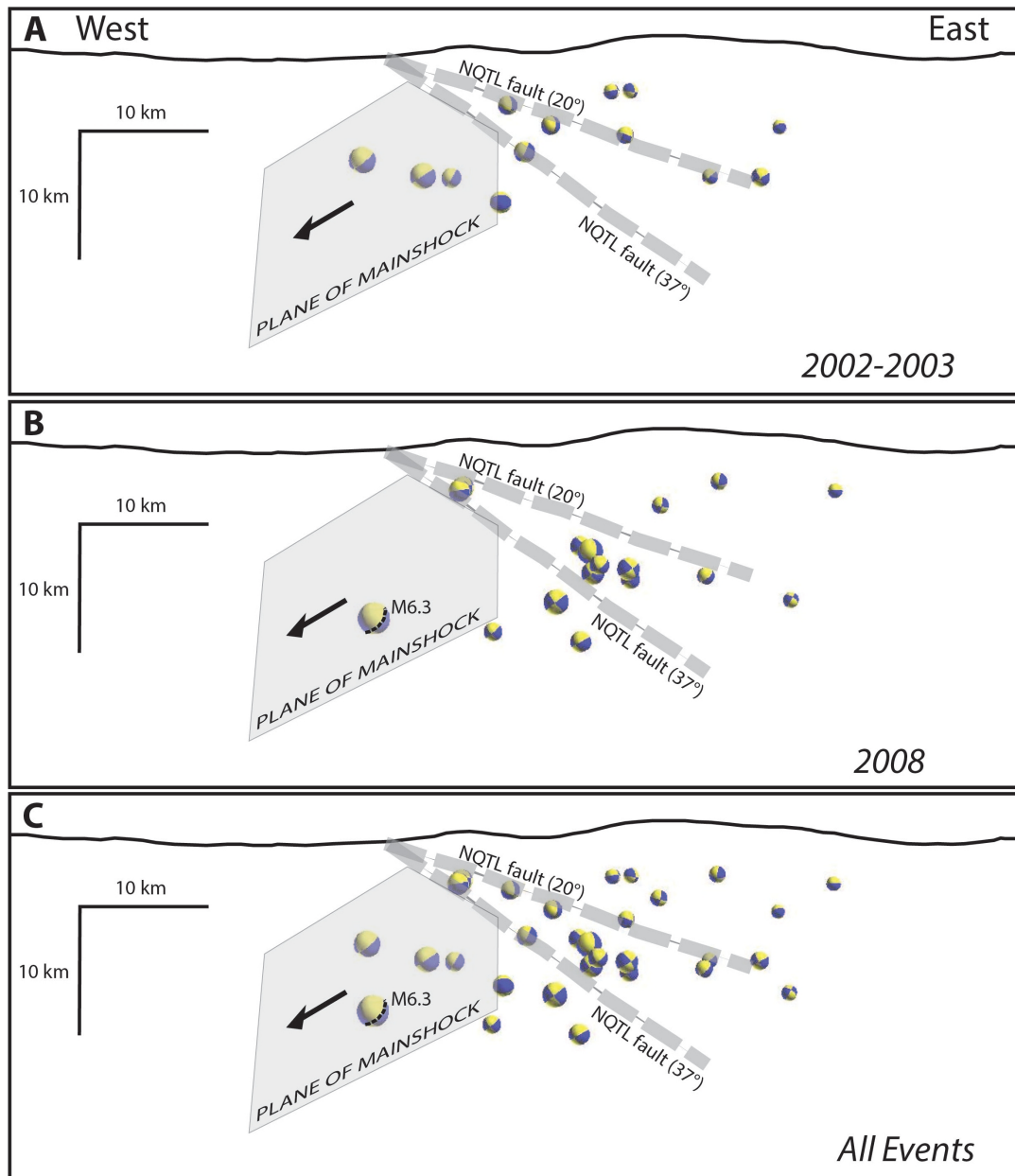


Figure 3.6: NQTL Region earthquake locations with respect to the NQTL. In these GOCAD screen captures, the earthquakes are shown with respect to the  $M_w 6.3$  Damxung Earthquake plane and lines representing the minimum and maximum possible dips of the NQTL (gray dotted lines). Topography is represented by the black line at the top of the A. 2002-3 swarm events. B. 2008 mainshock/aftershock series. C. 2002-3 swarm and mainshock/aftershock series.

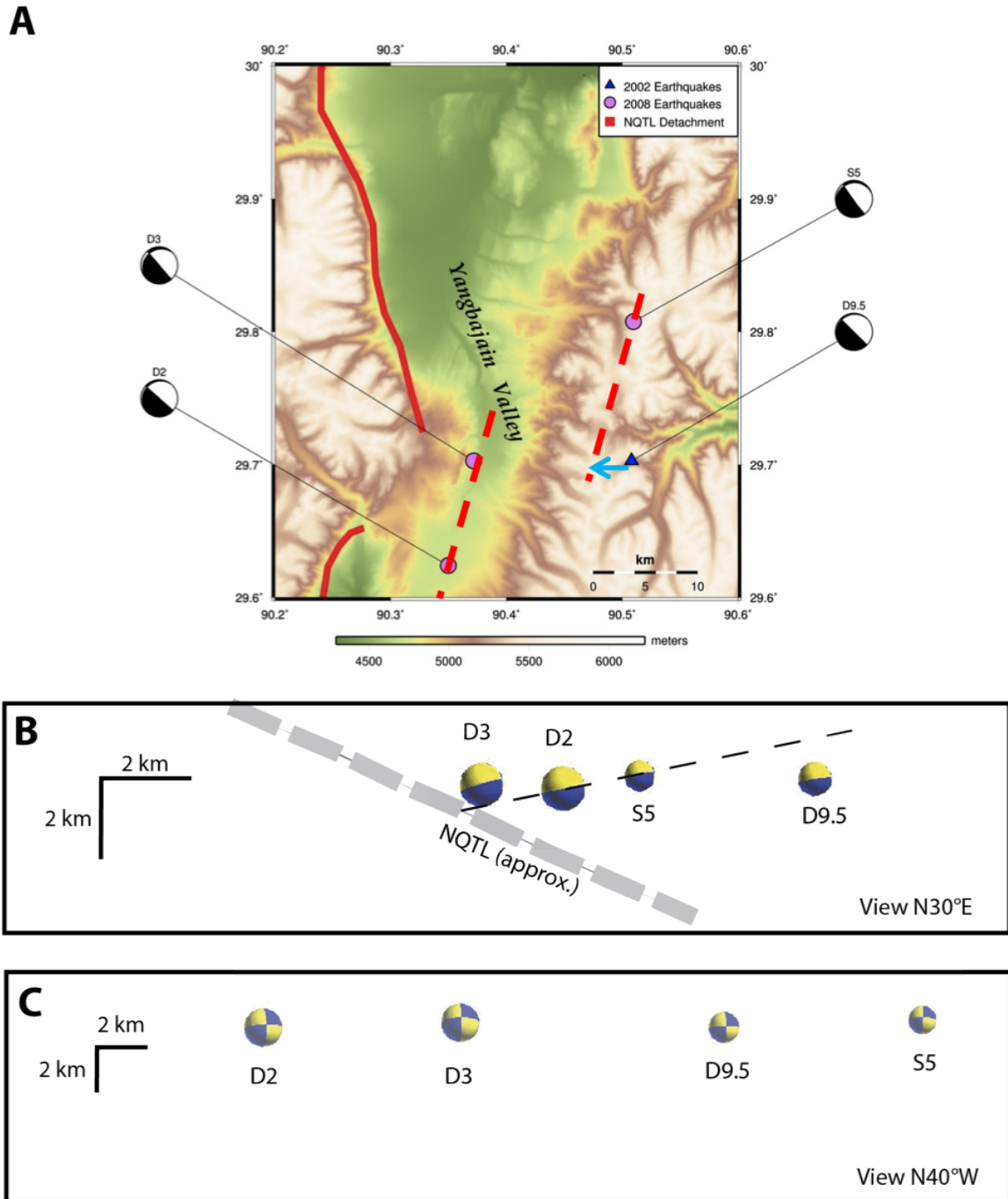


Figure 3.7: Group 1 earthquakes. A. Possible faults mapped within the Yangbajain Valley and Eastern Mountains. The fault mechanisms suggest that these earthquakes are occurring on either the same plane or on faults with similar orientations. B. GOCAD screen capture of group 1 events. The cross section of the NQTL fault surface is shown in gray. The fault plane common to all four events seems to be conjugate to the NQTL. C. A second GOCAD screen capture from a different view supports the notion that these earthquakes are occurring on a single fault plane.

the three best-located events (S5, D2 and D3) define a shallowly NW dipping plane that is well aligned with the subhorizontal plane of the mechanisms. Event D9.5 falls slightly below the plane, but also has a large location error. Viewed in cross section relative to slip along the most likely planes, the four events appear on average to define a shallow crustal, top-NE low-angle fault zone (decollement?), which we infer, based on figure 3.7B, to lie structurally above the NQTL detachment.

A second group of three events is also oblique slip, defined by events S1, S7 and S13 (figure 3.8A). A GOCAD view looking northward suggests that they define a steep, N-striking, west-side-down normal fault (figure 3.8B). This fault is a bit less convincing because the strike of event S1 differs slightly from the strike of the fault plane in the other two events. In addition, the location errors of S1 and S13 are relatively high, at 3.75 km and 4.375 km, respectively, which, given their N-S spacing of 5 to 10 km, introduces significant error in strike. Both the orientation and sense of offset of the steep planes are highly consistent with surface faulting in the southeastern Yangbajian Valley (figure 3.2). However, because the events occur at depths of 3 to 6 km, they appear to lie in the footwall of the subsurface projection of the NQTL detachment. All three events would all lie in the hanging wall of the NQTL detachment if it had a dip of  $> 30^\circ$  beneath southern Yangbajian Valley.

A third group of five similar events is located along the eastern edge of the valley. Based on their map view projection, events D5, D6, D7, D15 and D16 appear to define a NNE-striking normal fault (figure 3.9A). The events are all relatively deep (7 to 13 km), and reside in the footwall of the NQTL detachment (figure 3.9B). The mechanisms are predominantly normal, but do not define a simple plane when viewed in cross section across strike (figure 3.9B). The deepest event (D6) has a large location error (3.75 km), and thus may be coplanar with the better located, shallower events. The largest events of the entire aftershock sequence are events D5 and D7. They are the best located events (errors  $< 1$  km, table 3.1), and their moderately NW-dipping focal planes are well aligned (figure 3.9B). Events D15 and D16 are misaligned with the D5-D7 plane by 1 and 3 km, respectively, but occur near one another about 10 km along strike of D5 and D7. Thus some combination of their location error (both 1.9 km, table 3.1) and non-planarity of the fault may account for their position slightly off of the D5-D7 plane.

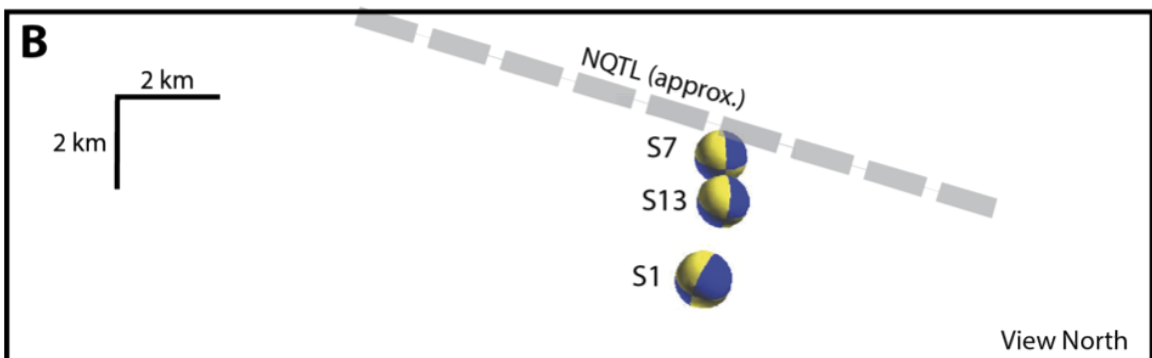
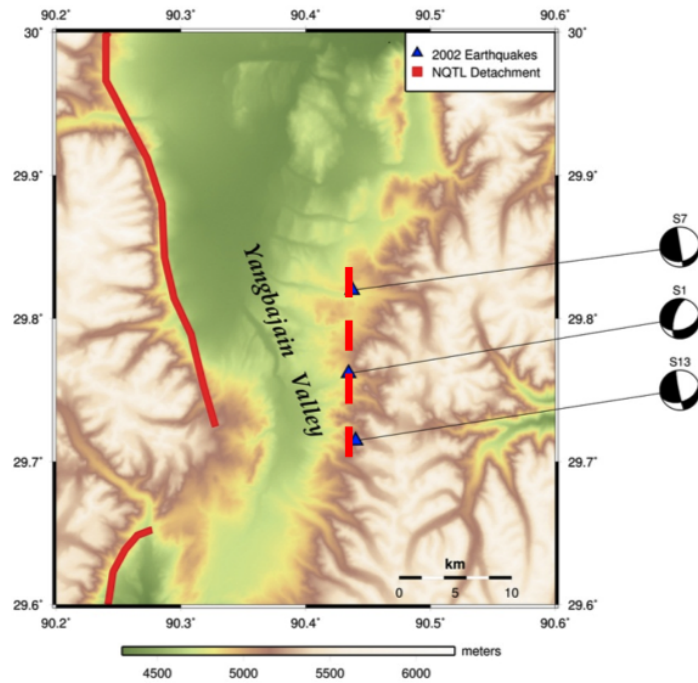
**A**

Figure 3.8: Group 2 earthquakes. A. A possible fault defined by events occurring along the western edge of the Eastern Mountains. B. GOCAD capture of the range bounding fault. An approximation of the NQTL surface is shown in gray. The fault on which these events likely occur seems to be slightly curved.

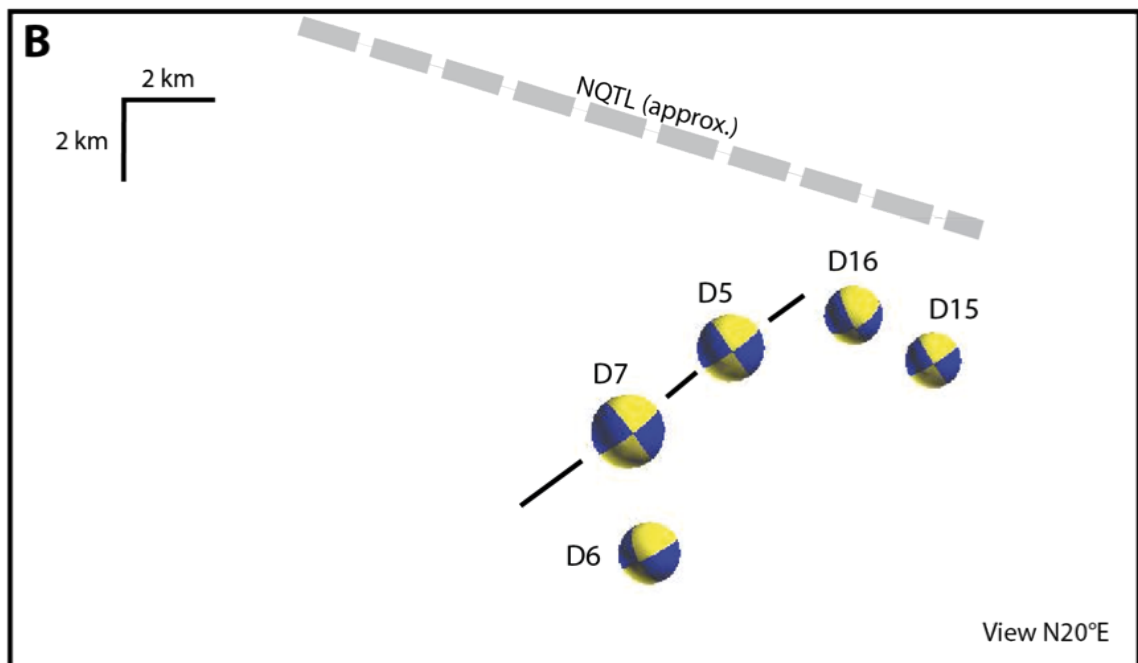
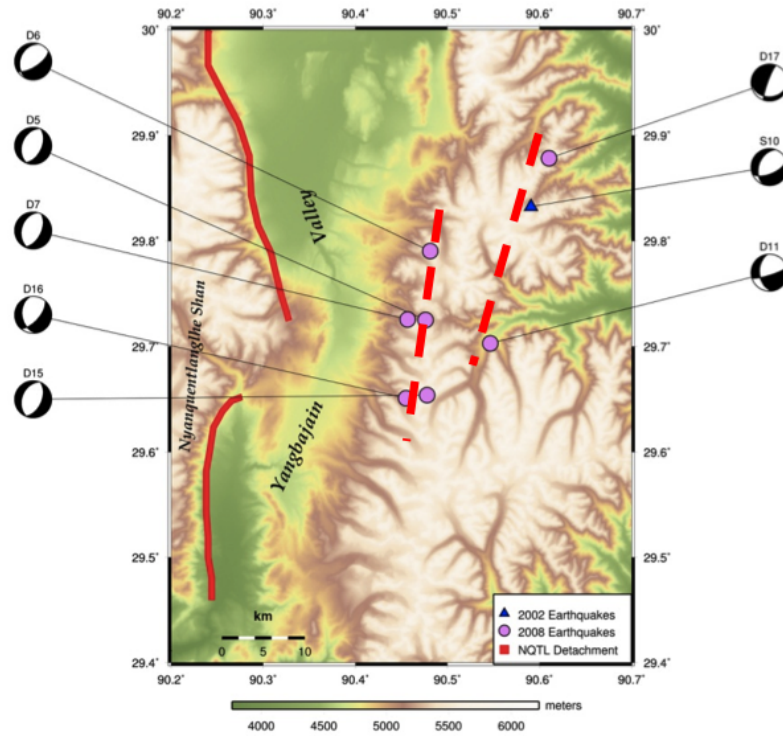
**A**

Figure 3.9: Group 3 and group 4 earthquakes. A. The events in group 3 line up along the fault in the western portion of the Eastern Mountains. The events in group 4 line up along the fault in the eastern part of the Eastern Mountains. Only the events in group 3 seem to line up along a likely fault plane when viewed in GOCAD. B. GOCAD capture of the group 3 earthquakes. A cross section of the NQTL fault surface is shown in gray. Although the mechanisms of these events look very similar and line up nicely in map view, only D5 and D7 seem to line up along a plane when viewed in 3D.

A fourth group of events located beneath the mountains east of Yangbajian (S10, D11 and D17) form a quasi-linear array of normal events whose steep, west-dipping nodal planes are much better aligned than their auxiliary planes (figure 3.9). The NNE strike of these events is similar to the third group of events, and thus appear to define a similar structure. No known active surface faults with this trend or offset have been identified in the surface geology. Given their eastern position and relatively shallow depth (2 to 8 km), these events occurred in the hanging wall of the NQTL detachment.

These groups of events, which include about half of the events in the LUR catalog, thus appear to define four structures, a shallow “decollement” beneath the Yanbajian Valley, and at least three NNE-striking, west-side-down, right-oblique normal faults. This pattern is generally in agreement with active surface normal faulting in the southern Yangbajian Valley. For the remainder of the events, the mechanisms are similar to those in the groups, but their locations do not form any discernible patterns. For these events, we used a criterion for most likely slip plane wherein the projected surface trace of the nodal plane most closely aligns with the traces of surface faulting. This criterion is relatively weak, such that as many as half of these planes (i.e., a statistically random sample) are not the true slip plane.

### 3.4 Slip Vector Patterns and Stress Tensor Calculations

Slip vectors from the most likely focal planes (strike, dip and rake, table 3.1) were converted into direction cosines (*Stein and Wysession, 2003, p. 218*), using Matlab, and into trend and plunge for use in Stereonet software (*Allmendinger et al., 2011*). Focal mechanism data were used to calculate a regional stress tensor using the program SLICK, based on the methods described in (*Michael, 1984, 1987*). The method is based on minimizing the mismatch between observed slip vectors on any given plane with those predicted by a uniform stress field. The average angular mismatch between the observed slip vectors and the best-fit model slip vectors ( $\beta$  angle of *Michael (1984)*) can be used to assess the quality of the model. We chose to use SLICK even though it well known that deformation patterns of earthquakes (in the form of slip and stress field perturbation) are generally known to

be spatially heterogeneous over a region. Variation in the spatial and chronological distribution of earthquakes is responsible for this heterogeneity and resulting variations in the stress field have been successfully modeled when large numbers of regional earthquakes are available for study (*Smith and Heaton, 2011*). Because we only had access to a catalog of 30 earthquakes, we chose use a method which would give us a more general idea of stresses within the region.

Slip vectors calculated from the most likely fault planes of the 2002 and 2008 events fall into three sets, consonant with the subset of events that may be grouped spatially with one another (figure 3.10). These include vectors trending NE or nearly due east on shallowly dipping planes (similar to group 1), north to NW-trending vectors on steeply dipping, NNW-striking planes (similar to groups 2 and 4), and NW-trending vectors on moderately inclined planes (similar to group 3). A fourth set that includes six planes, not apparent in any of the spatial groupings, includes gently to moderately east- to south-plunging vectors that are nearly pure normal events on shallowly to steeply inclined planes. These events have the strongest potential to be auxiliary planes, and their conjugate planes and slip vectors would mostly lie in the orientations of the other sets of planes. Nonetheless, some of the shallowly dipping planes in this set may well represent slip on the NQTL detachment, or faults parallel to it in the hanging wall and footwall.

In map view, the vectors have a relatively complex overall pattern (figure 3.11). The 2002 vectors mostly trend northward, with a large subset of events making a seemingly random pattern. The 2008 vectors appear to define a more organized pattern, diverging from an area centered on the western margin of Yangbajian Valley, opposite the salient in the surface trace of the NQTL detachment. Viewed as a whole, especially when factoring out the very shallow vectors trending NE (i.e., group 1 faults), the vectors seem to reinforce uplift of the area along the western margin of Yangbajian Valley, more-or-less centered on the population of events (figure 3.12) . An examination of the 3D model of the vectors constructed using Matlab did not reveal any obvious relationship between depth and the orientation of the slip vectors.

Because of the possibility that many of the likely slip planes (table 3.1) may be in error, we calculated stress orientations using three different assumptions (table 3.1). The first assumes the

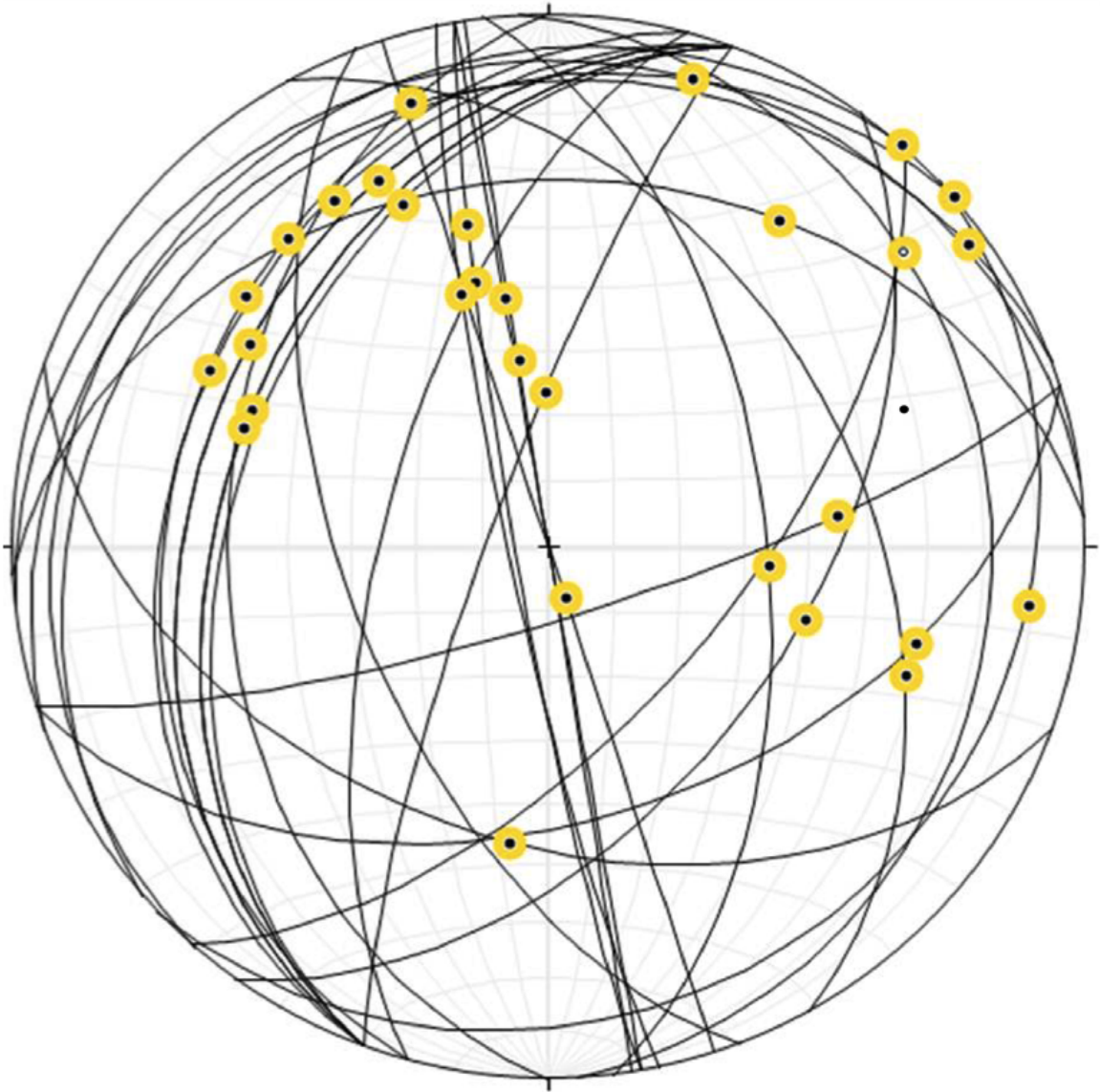


Figure 3.10: Stereonet of the most likely fault planes of earthquakes in the LUR catalog and their associated slip vectors.

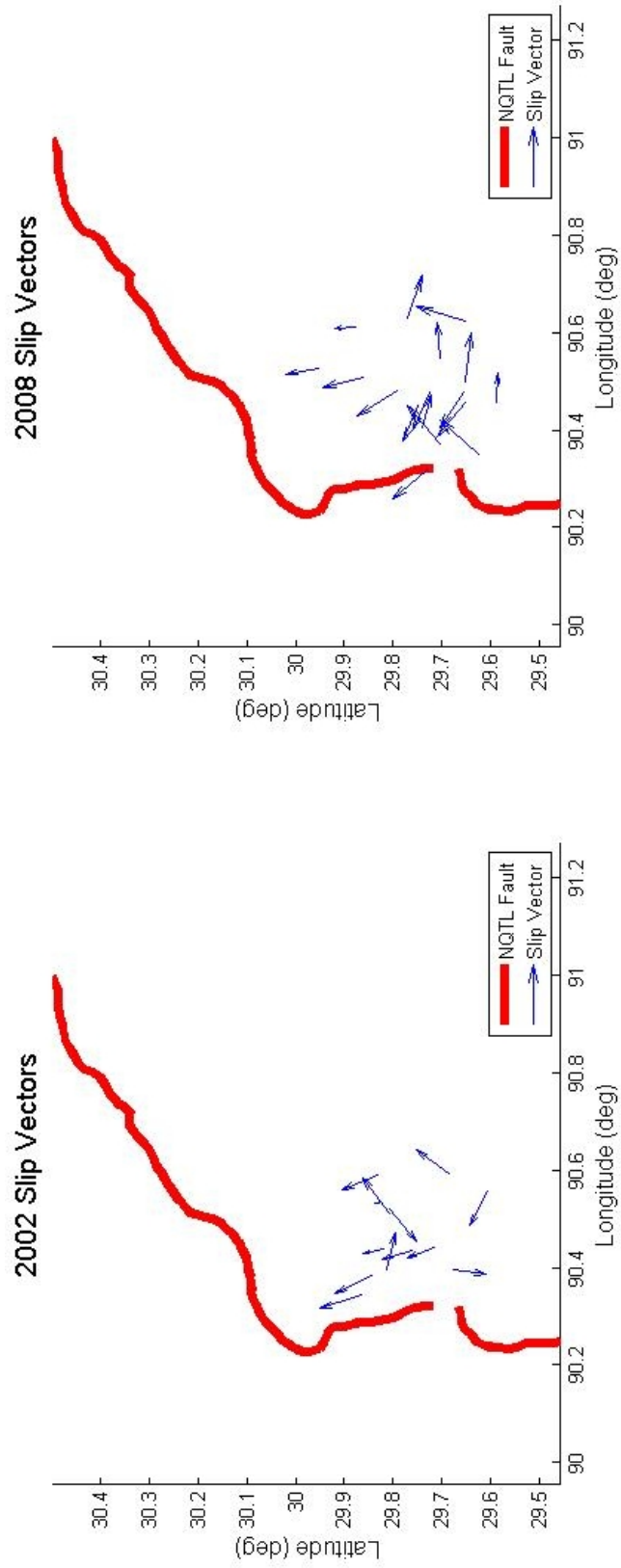


Figure 3.11: Slip Vectors associated with most likely planes plotted in map view. 2002 event slip vectors (left) 2008 event slip vectors (right).

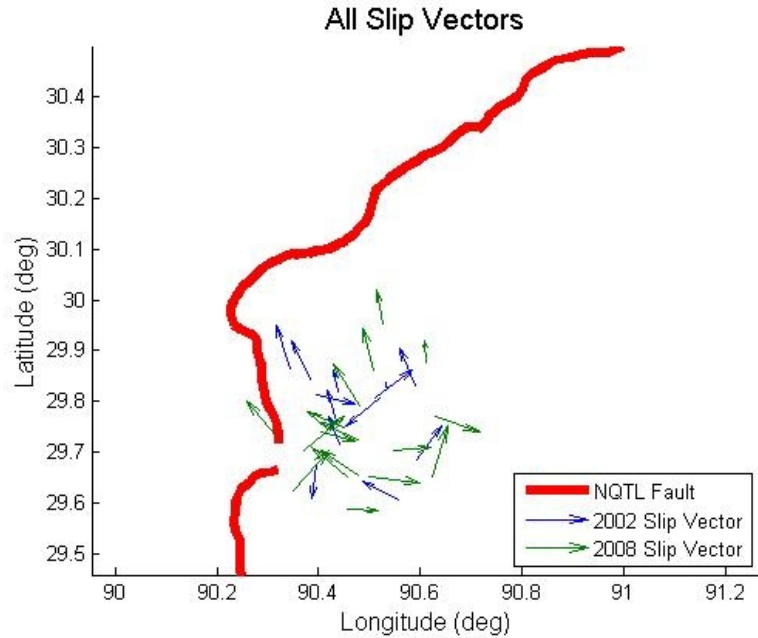


Figure 3.12: Slip Vectors associated with most likely planes plotted in map view (continued). Combined 2002 (blue) and 2008 (green) slip vectors.

plane randomly selected by CAP to represent the focal mechanism is the true slip plane. The second assumes the auxiliaries to these planes are the true slip planes. The third is the population of likely slip planes presented in table 3.1.

The results indicate that the orientations of the principal stresses are largely insensitive to which set of planes are assumed. Most sensitive are the 2002 swarm events, where the assumption of plane 1 yields a mean angular mismatch between observed and modeled slip vectors ( $\beta$ ) of  $16^\circ$ , almost half the value of  $29^\circ$  for the events deemed most likely (table 3.1). The complexity of the swarm is also indicated by the strong variation in the trend of calculated  $\sigma_3$  with the set of assumed planes, ranging from  $S12^\circ E$  to  $S48^\circ E$ , all much more southerly than determinations from other sets of assumptions (table 3.1).

Both the 2008 and combined 2002-2008 datasets yield a far more narrow range of results. The 2008 events alone show  $< 10^\circ$  variation in the trend of  $\sigma_3$ , from  $S 77^\circ E$  to  $S68^\circ E$ , and only  $5^\circ$  variation in the plunge of  $\sigma_1$ , from  $61^\circ$  to  $66^\circ$ . In contrast to the 2002 events, the lowest  $\beta$  value of the three sets of assumed planes corresponds to the likely set of events, at  $17^\circ$ . The combined 2002 and 2008 results yield a similar result to the 2008 results alone. Trends of  $\sigma_3$  are all within  $1^\circ$  of

each other, with the most likely planes trending  $S63^\circ E$ . The plunge of  $\sigma_1$  lies within a  $5^\circ$  window, with the most likely planes plunging  $68^\circ$ .

### 3.5 Discussion

The salient result of our analysis of these events is that the maximum principal stress ( $\sigma_1$ ) derived from stress inversion of the earthquakes is oriented at a high angle to the NQTL detachment. Under traditional Andersonian theory of faulting (*Anderson, 1951*), the vertical stress is a maximum principal stress. Therefore, the  $\sim 20^\circ$ - $30^\circ$  SSE to SE dip of the detachment would make it marginally oriented ( $30^\circ$  or greater) to misoriented ( $< 30^\circ$ ) within the regional stress field to slip. The fact that  $\sigma_1$  is not vertical, but rather plunges  $N36^\circ W$  at  $68^\circ$ , suggests that it is oriented within  $< 10^\circ$  of the normal to the detachment plane which on average strikes ENE and dips 20 to  $30^\circ$  ESE (*Kapp et al., 2005*). Assuming these measurements are correct, the NQTL detachment is yet another example of a major normal active fault in the brittle crust that is oriented such that the ratio of shear stress to normal stress across the fault plane is far below that expected for yielding under a Coulombic or Byerlee failure criterion.

Rotation of principal stresses in the upper crust, as suggested by the earthquake data, has traditionally been attributed to effects including high fluid pressures within the fault zone (*Axen, 1992*), or effects that create stress guides, such as flexure of the crust (*Spencer and Chase, 1989*), flow of viscous fluid directly beneath the seismogenic layer (*Yin, 1989; Melosh, 1990*), or dilation of the deep crust due to igneous intrusions (*Parsons and Thompson, 1993*). More recently, models of isotropic, uniformly stressed continental lithosphere that account for feedbacks between elastic and viscous strains in the upper crust and deep crust, respectively, predict the generation of subhorizontal shear zones in the strongest crust, near the brittle-ductile transition (*Regenauer-Lieb et al., 2006*). Despite these explanations, in the three decades or so of modern seismic instrumentation in continental rift zones, a moderate to large earthquake on a normal fault dipping less than  $\sim 25^\circ$  to  $30^\circ$  has not yet been observed (*Jackson and White, 1989; Wernicke, 1995; Elliott et al., 2010; Collettini et al., 2011*).

The events from the 2002 swarm and 2008 sequence do not add significantly to the extant database for seismic slip on low-angle normal faults. *Abers* (1991) and *Abers et al.* (1997) describe large earthquakes along detachments bounding metamorphic core complexes in the Woodlark-D'Entrecasteaux Rift System in Papua New Guinea, which dip  $25^\circ$  to  $30^\circ$  through the upper crust, as determined unambiguously by focal mechanisms and marine seismic reflection profiles across the hypocentral region of the earthquakes. Studies of the surface trace of the exhumed detachment indicate that high fluid pressures were present during deformation along a 33 m thick zone of serpentinite-rich fault gouge, suggesting that both high fluid pressures and non-Coulombic fault rocks contribute to the ability of the fault to slip at low angle (*Floyd et al.*, 2001). As noted earlier, relatively small low-angle normal fault earthquakes have also been observed in the Appenines (*Collettini et al.*, 2011) and in the Gulf of Corinth (*Katzir et al.*, 1996; *Famin et al.*, 2004; *Lecomte et al.*, 2012, 2010; *Jolivet et al.*, 2010).

By comparison, in our LUR catalog there are only the four group 1 events, which appear to define an upper crustal decollement, and two small earthquakes, D3 and D11 ( $M_w < 3$ ), which may have occurred on low-angle normal faults (table 3.1). The latter two events are located near each other at shallow depth east of Yangbajian Valley, well above the NQTL detachment. The dips of the most likely planes of D3 and D11 are  $10^\circ$  and  $14^\circ$ , respectively. The depths, locations and senses of slip on these events suggest that they did not occur on the NQTL detachment.

The fact that the earthquakes analyzed here do not correspond to slip along the NQTL detachment raises the question of precisely what their role is in the evolution of an active core complex. The observation that most of the events occurred in the footwall of the detachment and did not rupture through to the surface suggests that they reflect a significant component of brittle deformation in the footwall of a metamorphic core complex. The “radiating” pattern of slip vectors away from an area to the east of the salient in the surface trace of the detachment appear to reflect the uplift of the footwall. As noted by many authors, denudation of the upper crust along low-angle normal faults is necessarily accompanied by isostatic rebound of the unloaded footwall (*Wernicke and Axen*, 1988). Uplift would be particularly intense along antiformal salients in the detachment,

which are uplifted earlier than areas along regional strike, i.e. relative to embayments in the trace of the detachment. Whereas many authors have stressed flexure as a mechanism of footwall uplift (*Spencer, 1984*), *Wernicke and Axen (1988)* cited specific examples of footwall normal faults that also function to accommodate isostatic rebound. In the mid-Tertiary metamorphic core complexes of western North America, large, relatively steep footwall normal faults, conjugate to the main detachment, are common. For example, the Happy Valley fault in the footwall of the Catalina-Rincon detachment (*Drewes, 1981*), and the Ruby Valley fault in the footwall of the Ruby Mountains detachment, are good ancient analogs to the active uplift now ongoing beneath the NQTL detachment in Yangbajian Valley.

### 3.6 Conclusions

Through the use of an earthquake catalog constructed from focal mechanisms and locations determined by relatively new waveform modeling methods (CAP and the SP Envelope method), we have been able to analyze two earthquake sequences associated with an active metamorphic core complex in an orogenic plateau setting, which would otherwise not have been accessible to study owing to a lack of regional seismic coverage. Our analysis of the locations and earthquake focal mechanisms in the Yangbajian Valley segment of the Yadong-Gulu rift between 2002 and 2008 defines a system of west-side-down normal faults in the footwall and hanging wall of the NQTL detachment. The footwall structures, which include the ( $M_w$ ) 6.3 Damxung mainshock and two large aftershocks, are best interpreted as accommodating distributed footwall uplift across strike from a salient in the surface trace of the detachment, similar to structures that are well known from ancient metamorphic core complexes.

Inversion of focal mechanisms from these events suggest a stress tensor with an ESE-WNW least principal stress orientation, in close agreement with the sense of offset on the NQTL detachment determined from surface exposures. The orientation of the maximum principal stress (trending N36W, plunging  $68^\circ$ ) is perpendicular ( $\pm 10^\circ$ ) to the orientation of detachment, as recorded in surface exposures and subsurface seismic reflection and refraction profiles (table 3.2). This observation

Table 3.2: Slick program outputs

	$\sigma_1$		$\sigma_3$		$\beta$
	Trend	Plunge	Trend	Plunge	
2002					
Plane 1	-34.00	68.50	168.19	19.96	16.48
Plane 2	-29.31	64.13	131.90	24.62	25.21
Likely	-23.12	68.00	146.82	21.64	29.41
2008					
Plane 1	-45.14	66.25	104.14	20.68	23.01
Plane 2	-41.58	60.87	113.30	26.74	18.67
Likely	-41.81	66.50	108.90	20.74	16.56
2002&2008					
Plane 1	-36.33	69.06	115.89	18.66	22.59
Plane 2	-37.77	64.38	115.68	23.18	20.57
Likely	-35.80	68.26	117.13	19.51	22.17

appears to add the NQTL detachment, a major active fault zone in the upper continental crust, to a growing list of major upper crustal fault zones oriented at high angles to the maximum principal stress.

## Chapter 4

# A Possible Continental Slow Slip Event in the Nyainquentanglha Detachment Region, Southern Tibet

### 4.1 Introduction

The advent of continuous GPS (cGPS) coverage along subduction zones over the last 15 years has led to the discovery of discrete slow slip events (SSEs) along the subduction interface (*Schwartz and Rokosky, 2007*) and have been observed extensively in regions such as in Cascadia, Guerrero, Mexico, New Zealand, Alaska, and northeast Japan (*Dragert, 2001; Dragert et al., 2004; Lowry et al., 2001; Freymueller et al., 2002; Douglas et al., 2005*). These events radiate no seismic energy, and originate at the transition zone between aseismic slip at depths of  $\sim 20$  to 40 km depth, and the shallower seismic zone. The zone of SSEs behavior is generally regarded as a rheological boundary zone between velocity weakening and its associated stick-slip behavior, and velocity strengthening, stable sliding or creep.

Although most instances of SSEs have been observed at subduction zones, these events are also well known along a short stretch of the San Andreas Fault (*Wesson, 1988; Galehouse, 2002*) and along the Hayward Fault in northern California (*Burgmann et al., 2000; Simpson et al., 2001; Malservisi et al., 2003*), which have long been instrumented with pre-GPS geodetic infrastructure. In both of these instances slow slip occurs at the surface as well as at seismogenic depths. In addition,

SSEs occur along mid-ocean ridge transform faults, and may accommodate as much as 85% of their motion (*Boettcher and Jordan, 2004*).

Continental SSEs, not associated with motion along a nearby plate boundary, have also been described in the orogenic plateau setting of the Basin and Range Province (*Davis et al., 2006*). For these events, large portions of the Basin and Range crust exhibit coherent velocity changes of  $\sim 1$  to  $4\text{mm/yr}$ , interpreted as representing oscillating motion along a megadetachment. Considering a variety of indicators, including a magma injection event near the Moho during one of the slip events (*Smith et al., 2004*), the structure, the state of stress, and the rheology of the Basin and Range lithosphere, these events have been interpreted to represent ductile stick-slip along a  $\sim 500\text{km}$  wide detachment surface along the Moho (*Wernicke et al., 2008; Wernicke and Davis, 2010*).

Another possible SSE in an orogenic plateau setting may be represented by a strong increase in the east component of velocity which was recorded at a cGPS site in Lhasa, Tibet, between the beginning of 2001 and the middle of 2002. The apparent rapid cessation of this event was immediately followed by an earthquake swarm in 2002-2003 in the Yadong-Gulu rift, about 70 km west of Lhasa (described in chapters 2 and 3), and then six years later by the ( $M_w 6.3$ ) Damxung earthquake, in the same area of the rift as the swarm (*Elliott et al., 2010, chapters 2 and 3*). The western margin of the rift at this latitude is bounded by a major SE to E-dipping low-angle normal fault, the Nyainqentanglha (NQTL) detachment (*Harrison et al., 1995; Cogan et al., 1998; Kapp et al., 2005*), which juxtaposes mid-crustal metamorphic tectonites in its footwall against Quaternary and older basin fill in its hanging wall. In addition to these observations, the Yadong-Gulu rift valley is underlain by a zone of strong mid-crustal reflections, below which magnetotelluric and seismic velocity profiling suggest the existence of a partially molten zone (*Nelson et al., 1996*) and (*Cogan et al., 1998*).

In this chapter, we synthesize these observations to develop the hypothesis that the swarm observed within the rift region was related to a slow-slip event at depth, most plausibly along the NQTL detachment, but possibly as deep as the Moho. If correct, it implies that the numerous earthquake swarms that characterize Tibetan rift valleys ( $M_w < 4$ ) are associated with SSEs on

inter- or intralithospheric decoupling horizons present at depth well outside the upper crustal rifts. This event would also be only the second continental SSE ever observed.

## 4.2 Data and Methods

Continuous GPS data recorded at station LHAS at Lhasa, Tibet from 1996 to 2005 was initially processed using the GAMIT/GLOBK and GIPSY OASIS II software packages. Daily position estimates with uncertainties of 1-2 mm in east and north directions and 3-6 mm in the vertical direction were determined using methods detailed in (*Bennett et al.*, 2002, 2003; *Hreinsdottir et al.*, 2003). Seasonal stochastic variations in velocities were removed using the Site Position Kalman Filter (SPKF), which was developed for processing data recorded by the BARGEN network (*Davis et al.*, 2006). These filtered data were then analyzed for the presence of velocity transients following the method described in *Wernicke and Davis* (2010). Time series for continuous GPS data for a new cGPS site LHAS, located near the decommissioned IGS site LHAS, from 2007.0 to 2010.9, were processed using the GYPSY-OASIS software package following the methods described (*Genrich et al.*, 2000), and filtered to generate velocity time series as for site LHAS.

Earthquake focal mechanism locations and focal mechanisms were obtained using CAP (Cut and Paste) along with the SP-Envelope method described in chapter 2. Kinematic data from surface exposures of the NQTL detachment, which reflect its late Miocene and younger evolution, were obtained by *Kapp et al.* (2005).

## 4.3 Results

The average motion of site LHAS, relative to a Eurasian reference frame, is N45°E at 26 mm/yr (*Zhang et al.*, 2004, figure;)). Relative to a western Tibetan frame, it is moving due east at a rate that varies from 15 to 19 mm/yr. The eastward motion is part of the overall eastward flow of southern and central Tibet relative to both India and Asia (*Copley*, 2008). Significant changes in velocity were recorded at LHAS between 1998 and 2004 (figure 4.2). The east component of velocity,

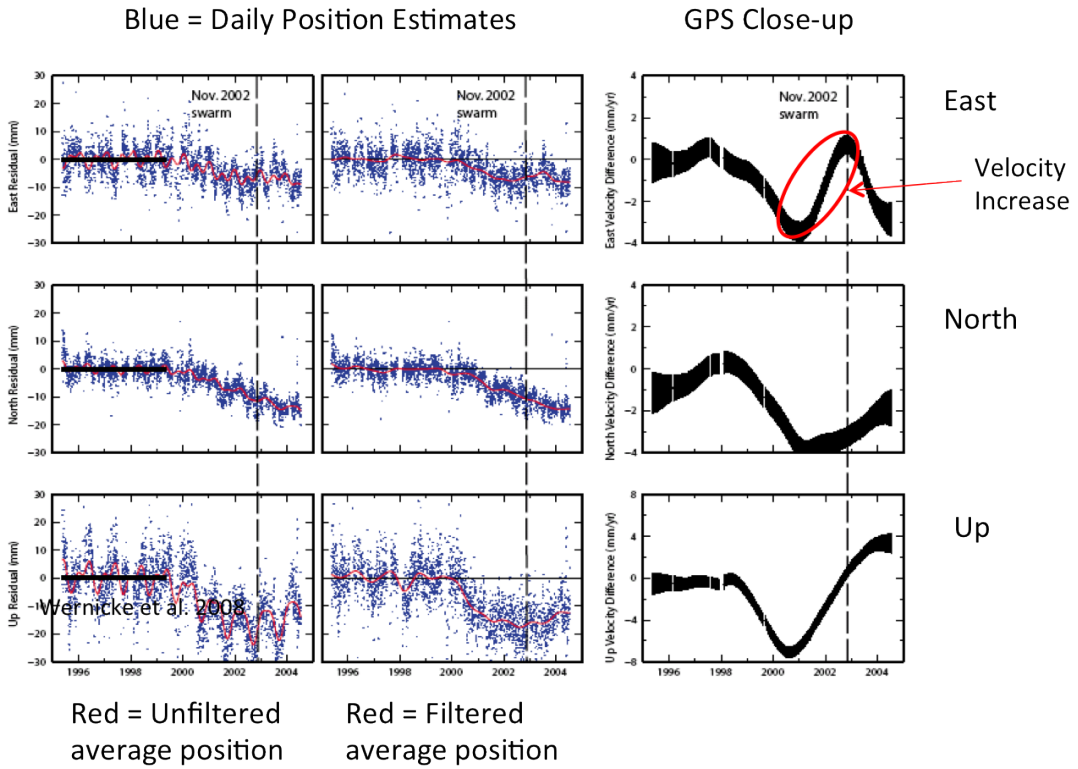


Figure 4.1: cGPS records from LHAS at Lhasa Tibet from 1995 to 2004. An increase in the eastward component of velocity was observed just before the NQTL Region Swarm began in 2002.

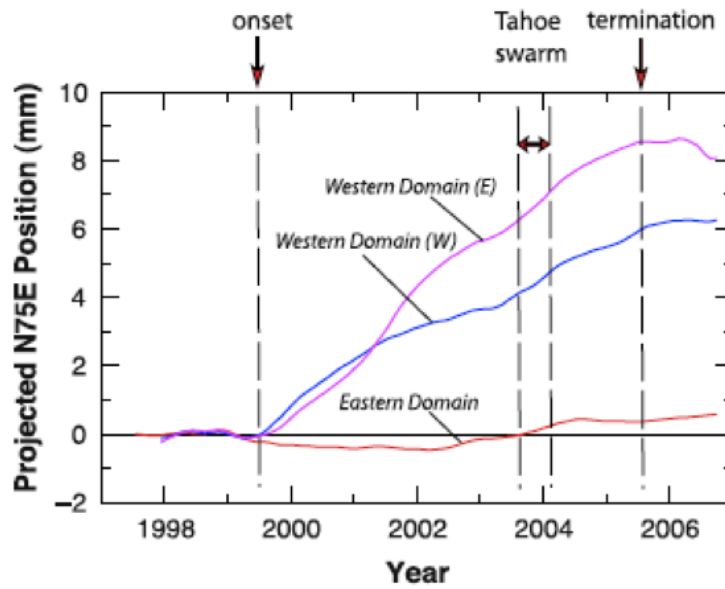


Figure 4.2: Velocity anomalies measured within the BARGEN network in the Basin and Range. From *Wernicke et al.* (2008).

relative to its average value from 1995 to 1998, gradually decreased by 4 mm/yr over this period. Then from its minimum near 2001.0, it rapidly increased by 4 mm/yr, peaking in late 2002, and then rapidly decreased back to its T2001.0 value. The north component may have increased by up to 1 mm/yr over this period of “spiking” east velocity, but the change is not statistically different from zero. The resulting combined velocity vector suggests that the rapid, anomalous motion measured at LHAS was E or ENE, relative to its average velocity. It is noteworthy that all three components of velocity began slowing in 2000, but only the east component appears to have a strong temporal correlation with the earthquake swarm.

In marked contrast to the major velocity transients near the time of the swarm, no significant velocity transients were observed in the 1.5 years before and after the October 6, 2008 Damxung mainshock and its aftershocks (figure 4.3). This is somewhat surprising, given that the aftershocks occur in the same area as the swarm, with a similar population of focal mechanisms as the swarm.

The kinematics of both the 2002-2003 swarm and 2008 earthquake sequence indicate generally E-W extension. The NQTL detachment is divisible into two major segments, one striking NE and the other striking N-S. The NE striking segment indicates ESE displacement along the shear zone, but where the detachment bends southward, the kinematic data suggest more easterly extension (figure 4.1). The orientation of the active stress field, derived from inversion of the 2002 and 2008 events described in chapter 3, suggests that the least principal stress trends  $S65^{\circ}E$ .

## 4.4 Discussion and Conclusions

Velocity vectors calculated from transient GPS signals measured at LHAS indicate that the directions of motion before and after the 2002-3 swarm were east with a smaller component of northward motion, i.e. approximately parallel to the displacement along the NQTL detachment, but  $20^{\circ}$  to  $30^{\circ}$  more easterly. These motions are very likely to be tectonic because the swarm occurred at the peak of rapid eastward motion. The rapid decrease in east velocity recorded at LHAS after the swarm suggests that the swarm and the motion were somehow related.

The fact that this transient was only recorded at LHAS weakens this hypothesis, because we

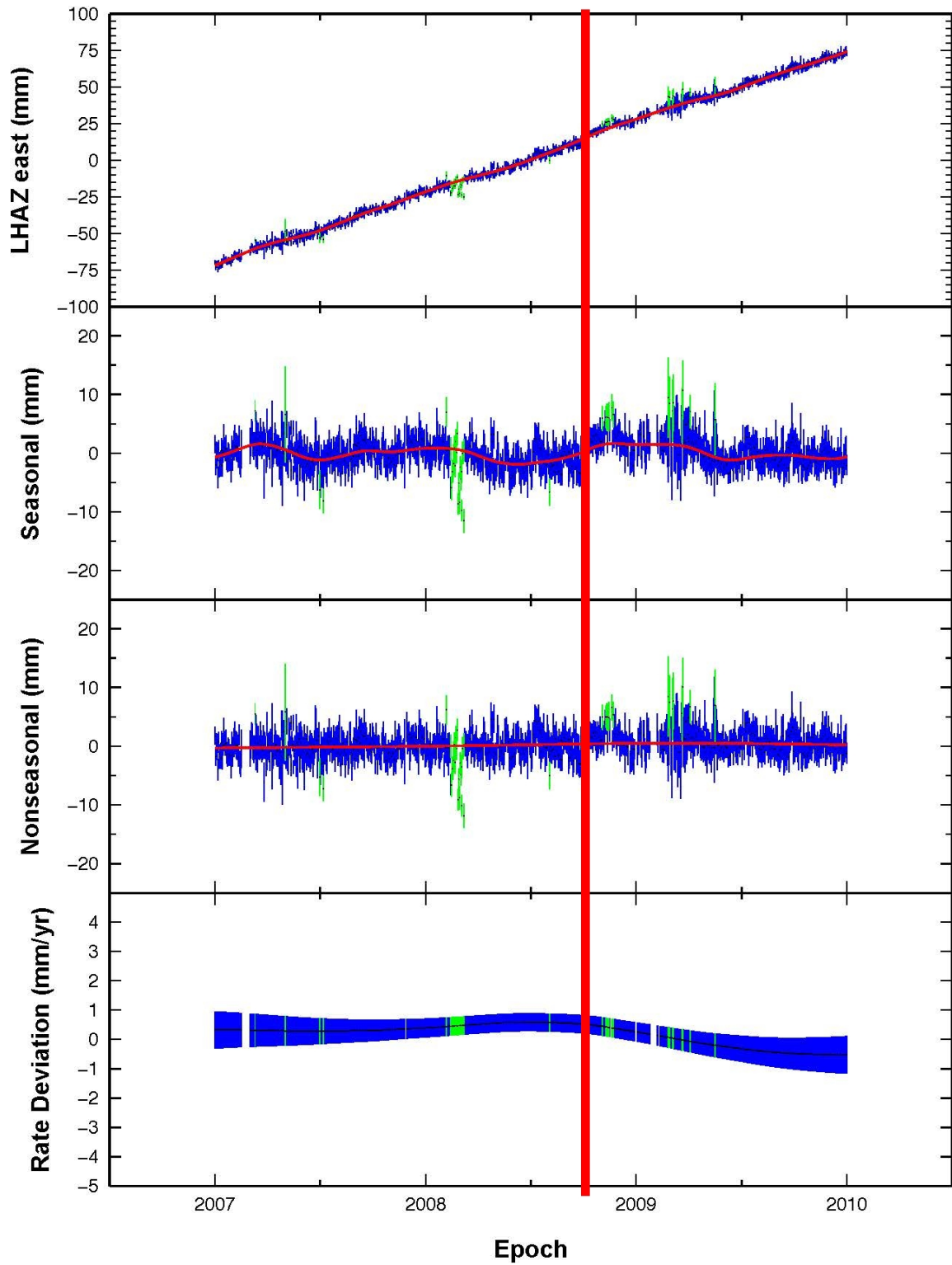


Figure 4.3: The east component of velocity measure at the cGPS station at LHAZ before and after the 2008 ( $M_w$ 6.3) Damxung earthquake. The red line indicates the timing of the Damxung earthquake.

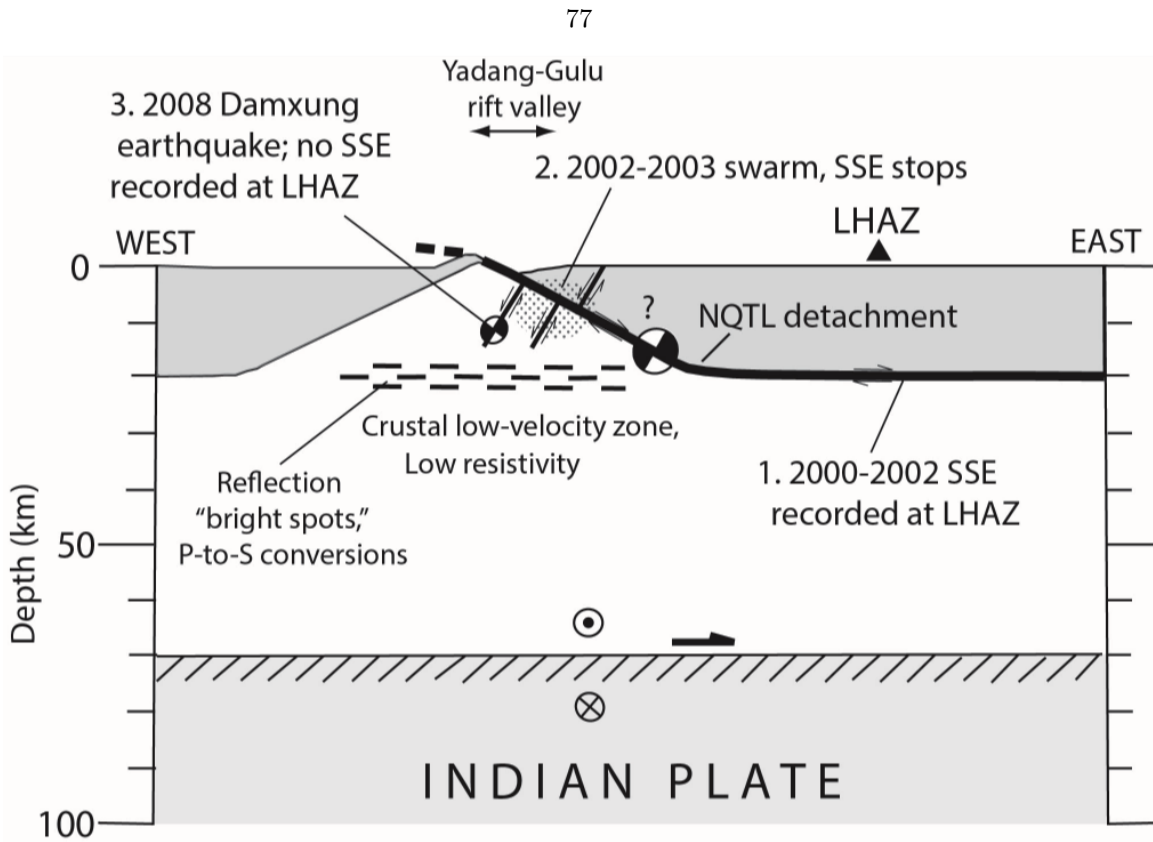


Figure 4.4: Schematic of deformation within the Yadong Gulu Rift Valley and surrounding regions between 2000 and 2010. The large focal mechanism east of the swarm location represents the sense of motion of a large earthquake that could occur along the NQTL in the future.

cannot eliminate the possibility that local site effects (e.g., hydrological effects), which are well known from some cGPS sites, are a cause of the transient motions. In particular, the effect of groundwater withdrawal and changes in the levels of large lakes are known to cause similar velocity changes elsewhere (reference); however, it is not likely that such effects are the source of anomalous motion seen at LHAS, because there are no lakes or other large bodies of water near the Lhasa site, and the thickness of alluvium in the Lhasa River valley is at most tens to perhaps a few hundred meters. Seasonal signals related to hydrology and climate, which as is obvious from figures 4.2 and 4.3 produce large motions of the site, were removed during data processing by using the SPKF.

Motion on the NQTL detachment, or along some other interface below it, is the most straightforward explanation of the velocity transients (figure 4.4). Along subduction interfaces, at the depths at which SSEs occur, temperatures are ca.350 – 550°C (*Dragert et al., 2004*). As noted by previous workers, at depths of 15 to 20 km beneath the region, temperatures high enough for a transition from

brittle deformation to crystal-plastic deformation of granitic rocks have been observed (*Makovsky et al.*, 1996; *Chen et al.*, 1996; *Kind et al.*, 1996; *Alsdorf and Nelson*, 1999). Wide-angle and near-vertical incidence seismic reflection data acquired beneath the NQTL region during the INDEPTH II experiment exhibit strong P to S conversions, and reflection “bright spots” at 15 to 20 km depth (*Brown et al.*, 1996; *Makovsky et al.*, 1996; *Chen et al.*, 1996; *Kind et al.*, 1996). Below these features, teleseismic data suggest a pronounced intracrustal low-velocity zone, and magnetotelluric profiling suggests low crustal resistivity (*Nelson et al.*, 1996, summarized in). All of these observations are consistent with the presence of the zone of partially molten material at 15-20 km depth beneath the Yadong-Gulu rift and environs. These inferences regarding the active tectonic regime are supported by the conditions of late Miocene deformation observed in the footwall of the NQTL, where both syntectonic intrusions of granitic magmas, and mylonitic deformation of the intrusive rocks (*Kapp et al.*, 2005), indicate low amphibolite facies temperatures appropriate for SSEs on the down-dip projection of the NQTL detachment into the middle crust (figure 4.4).

In the case of the Basin and Range SSEs, a variety of data support the hypothesis that SSEs are generated by active intrusion and shearing along the Moho, rather than along a mid-crustal interface. The primary data that support this hypothesis are the temporal correlation of an earthquake swarm at Moho depth with one of the largest velocity transients observed in the GPS data (*Wernicke et al.*, 2008), and the spatial correlation of transient velocities with a strongly reflective Moho. In the NQTL region we do not currently have any data to support the idea that the Moho, which is found at depths of 70-80 km beneath Tibet, is the source of this motion. Rather, both criteria for the SSE-generating interface in the Basin and Range, temporal correlation with seismicity and spatial correlation with an imaged interface at depth, point toward the NQTL.

The cGPS transients and seismicity appear to define the cycle of seismic and geodetic events that occur within the NQTL region. The sequence begins with a top-east, SSE along the down-dip projection of the NQTL detachment beneath the Lhasa region east of the rift (figure 4.4). Strain release on such an interface would be expected to be top-east, increasing the eastward velocity. This sliding would be expected to increase differential stress to the west in the Yadong-Gulu rift region,

and hence we suggest that the peak of eastward velocity triggered up-dip brittle failure in the form of the 2002-2003 earthquake swarm. The modest strain relief represented by the swarm caused the decrease in eastward velocity which transitioned into period of low velocity and coupling between the upper crust and deep crust under Lhasa. The observation that the mainshock had no relation to SSE sliding, whereas the swarm did, suggests that the swarms are an expression of geodetic transients. In contrast, the large events, as is typically the case, occur without any warning.

Because we have only observed one NQTL region “cycle” we cannot say that the observed order of events is the order in which they will always occur. It is likely that multiple episodes of rapid sliding and associated earthquake swarms follow each other, given the decadal frequency of swarm events associated with Tibetan rift valleys. In this sense, the 2008 Damxung mainshock may be somewhat anomalous, in that most swarms are not followed by large events within the decade. The Damxung event, in terms of net moment released in the Yadong-Gulu rift, is a minor event. The net extension rate across the rift is perhaps as much as 5 mm/yr, and so the NQTL detachment need only fail once every few thousand years. As such, there is little surprise (*Elliott et al.*, 2010, cf. ) that the limited record of a few decades of Tibetan normal fault earthquakes grossly underestimates the internal strain rate measured geodetically.

## Chapter 5

# Using Cut and Paste to Invert for Microearthquake Source Mechanisms – A Preliminary Study

### 5.1 Introduction

Reliable earthquake source characteristics are difficult to calculate from borehole geophone records used in the passive microseismic monitoring of hydraulic fracturing. The quality of the calculated source characteristics is heavily dependent on the azimuthal distribution of the monitor wells in which borehole geophones are situated, the accuracy of the velocity model, the recorded data's signal to noise ratio, and general down-hole conditions. Because of these difficulties, records obtained from microseismic monitoring studies are most often used to determine locations but not focal mechanisms of microseisms associated with hydrofracturing in oilfields. These earthquake locations are used to image the fracture networks activated during hydraulic fracturing stimulation of tight reservoirs (*Albright and Hanold, 1976; Pearson, 1981; Pine and Batchelor, 1984; Fehler, 1989*) and during the injection and production process (*Majer and McEvilly, 1979; Denlinger and Bufe, 1982; Eberhart-Phillips and Oppenheimer, 1984*).

Microseismicity induced by hydraulic fracturing generally occurs within a 3D, elongated cloud of event locations (*House, 1987; Jones et al., 1995; Warpinski et al., 1995; Phillips et al., 1998*) and is thought to be caused by several different mechanisms. Fracture nucleation can cause tensile

failure earthquakes within the rock through which the fracture is propagating. Large shear stresses at fracture tips are often generated as a result of the extension associated with fracture opening (*Sneddon, 1946*). These shear stresses also cause shear slip to occur on nearby favorably oriented planes of weakness such as bedding, joints, and natural fractures (*Nolen-Hoeksema and Ruff, 2001*). Earthquakes also occur when high pressure pore fluids present within the hydraulic fracture leak into the surrounding rock, replace native pore fluids, and increase pore pressures (*Maxwell et al., 2010*). These increased pore pressures change the local stress regime by reducing normal stresses, and thus cause motion on nearby planes of weakness (*Pearson, 1981; Cornet and Julien, 1989; Fehler, 1989; Jupe et al., 1992, 1998; Feng and Lees, 1998; Nolen-Hoeksema and Ruff, 2001*).

The locations and source mechanisms of microseismic events can be used to calculate the volume of the region stimulated by hydrofracturing, the orientation of fractures within this region, fracture dimensions, local stresses, and fluid flow (*Rutledge and Phillips, 2003*). Methods for determining earthquake locations can be classified into three groups. The first group of methods, called the hodogram technique (e.g. (*Albright and Hanold, 1976*)), requires that data be recorded by a three component geophone. A hodogram is a plot of the particle motion caused by the direct P and/or Swave arrival. Back-azimuth can be calculated from a hodogram if it is assumed that these direct arrivals are polarized in the direction of wave propagation (*Maxwell et al., 2010*). The final location is then determined by calculating the difference between P and S arrival times when the velocity model is well-known. The second group of methods is derived from triangulation methods developed in the early days of seismology (*Shapiro, 2008; Gibowicz and Kijko, 1994*) and uses P and S-wave arrivals at multiple stations to obtain an earthquake location. The third group of location methods avoids using P and S arrival times altogether by maximizing a semblance measure of a single phase and is similar to Kirchoff migration (*Drew et al., 2005*) and (*Rentsch et al., 2007*). The accuracy of locations obtained using any of these methods is dependent on the quality of the velocity model and the suitability of the geophone array geometry to the region (*Pavlis, 1986*).

Microseismic earthquake source location determination methods are well researched and generally reliable. Conversely, microseismic focal mechanism determination methods are less developed. The

focal mechanisms of microseismic events are most often determined by plotting P-wave first motions on a focal sphere (e.g. (*Sasaki*, 1998; *Rutledge and Phillips*, 2003; *Rutledge et al.*, 2004)). Previous studies of P-wave radiation patterns have found that shearing is the dominant sense of motion associated with hydraulic fracturing related microseismic events with depths of 10 to 4000 m (e.g., (*Cash et al.*, 1983; *Matsunaga et al.*, 1989; *Wallroth*, 1992)). Observed microseismicity is unlikely to be purely tensile because hydraulic fractures are nearly aseismic (*Sasaki*, 1998). Although tensile earthquakes do occur, the seismic energy radiated by tensile failure is small compared to that of shear failure, and thus is much more difficult to detect.

Limited azimuthal distribution of boreholes and their borehole geophones has made it very difficult to determine accurate source mechanisms of microseismic events using first motion plotting methods. The expense of drilling wells to improve azimuthal coverage makes finding a method of determining focal mechanisms with few geophones a desirable alternative option. One method which could be effective in this endeavor is Cut-and-Paste (CAP). This S-waveform modeling method, developed in (*Zhao and Helmberger*, 1994) and improved in (*Zhu and Helmberger*, 1996) allows for the determination of focal mechanisms using regional broadband seismic records and has been used successfully in regions where station coverage is sparse. When given an earthquake location, CAP calculates the source mechanism by splitting the record in the Pnl and surface wave components and cross correlating the data with synthetic seismograms generated using a grid search for strike, dip and rake. The fact that the seismograms are split into body-wave and surface-wave portions reduces the impact of inaccuracies in the velocity model and Green's functions on the quality of the focal mechanism.

In this chapter, we test whether CAP can be effectively used to solve the problem of determining focal mechanisms in oilfields with poor azimuthal station coverage by studying a microseismic dataset acquired in the Piceance Basin of northwestern Colorado in 2008. This data set, which was acquired below ground by borehole geophones, does not contain any surface waves. CAP is able to work around this problem by equating the S-waves in the record to surface waves. If successful in working with such an unconventional dataset, CAP could make the calculation of microseismic

source parameters as ubiquitous as the calculation of source locations and could greatly improve our understanding of crustal deformation associated with hydraulic fracturing microseismic events.

## 5.2 Geological Setting of the Piceance Basin

The Piceance Basin of northwestern Colorado is comprised of 10,101 square km of exposed Cenozoic rocks (figure 5.1). The boundaries of the basin are demarcated by strong structural boundaries and outcrops of the Cretaceous-Tertiary contact. The basin is a northwest-trending asymmetrical downwarp with shallow dips on the southwest flank and steeper dips on the northeast flank. Folds, high-angle normal faults, and fracture and joint systems can also be found throughout the basin (*Anderson, 1980*).

The Precambrian basement complex lining the basin is draped by a continuous sequence of sedimentary rocks with a maximum thickness of 8230 m (*Anderson, 1980*). The fracture stimulation project that generated the micro-earthquakes studied in this chapter was performed in the Upper Cretaceous Williams Fork Formation (figure 5.2). This formation is part of the Mesaverde Group, one of the most productive tight gas reservoirs in the world. The rocks within the Williams Fork Formation are mostly very low permeability, highly cemented, fine- to medium-grained sandstones which are rich in volcanic and carbonate lithic fragments (*Ozkan et al., 2010*). The formation also contains mudrocks which were deposited in coastal and fluvial environments.

## 5.3 Data

### 5.3.1 Tools and Acquisition Geometry

From August to October 2008, microseismic data were collected during a fracture stimulation program in a gas well located in tight Williams Fork Formation sandstones. Data were acquired using dual element Oyo DS 250 high output geophones. These three component geophones were deployed via wireline in 12-unit arrays in two separate cased, vertical monitor wells (figure 5.3). In array 1 and array 2, the geophones were distributed over 1277 m to 1408 m and 1405 m to 1536 m respectively.



Figure 5.1: The Piceance Basin of northwestern Colorado. The study area is shown within the red box (Sarkar et al., 2011).

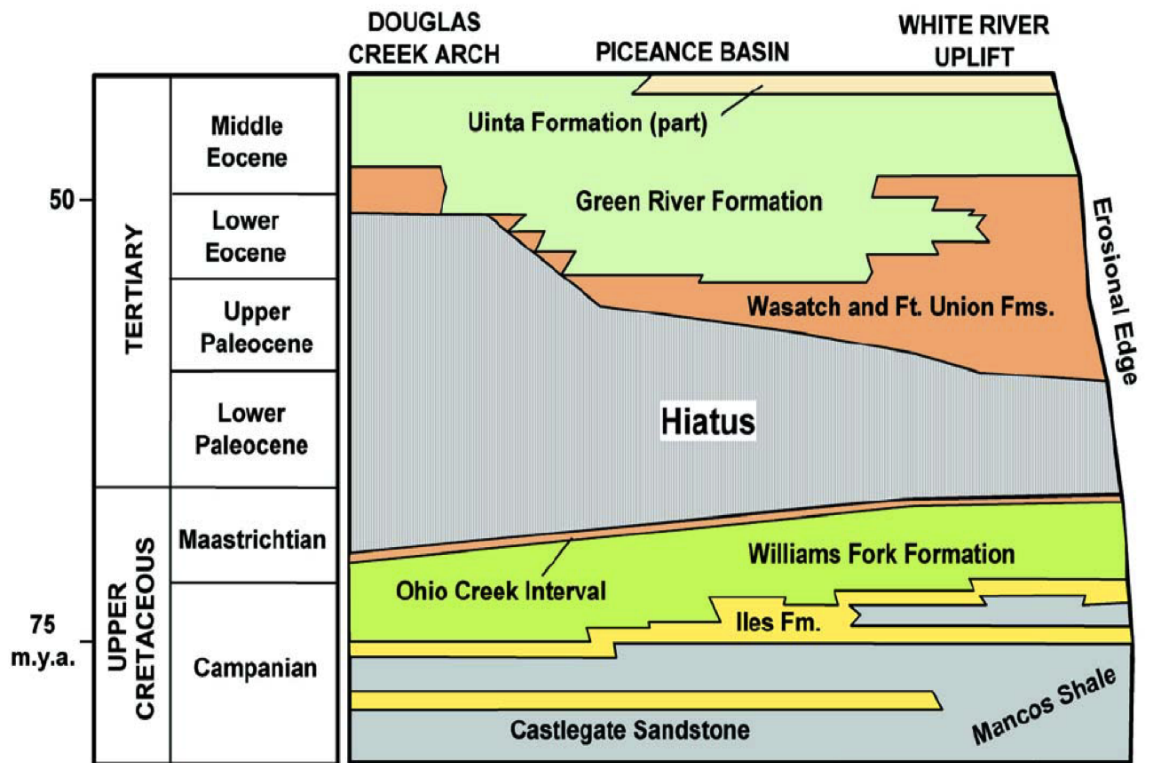


Figure 5.2: Piceance basin regional stratigraphy. The study region is within the Williams Fork Formation. (Cole and Cumella, 2003)

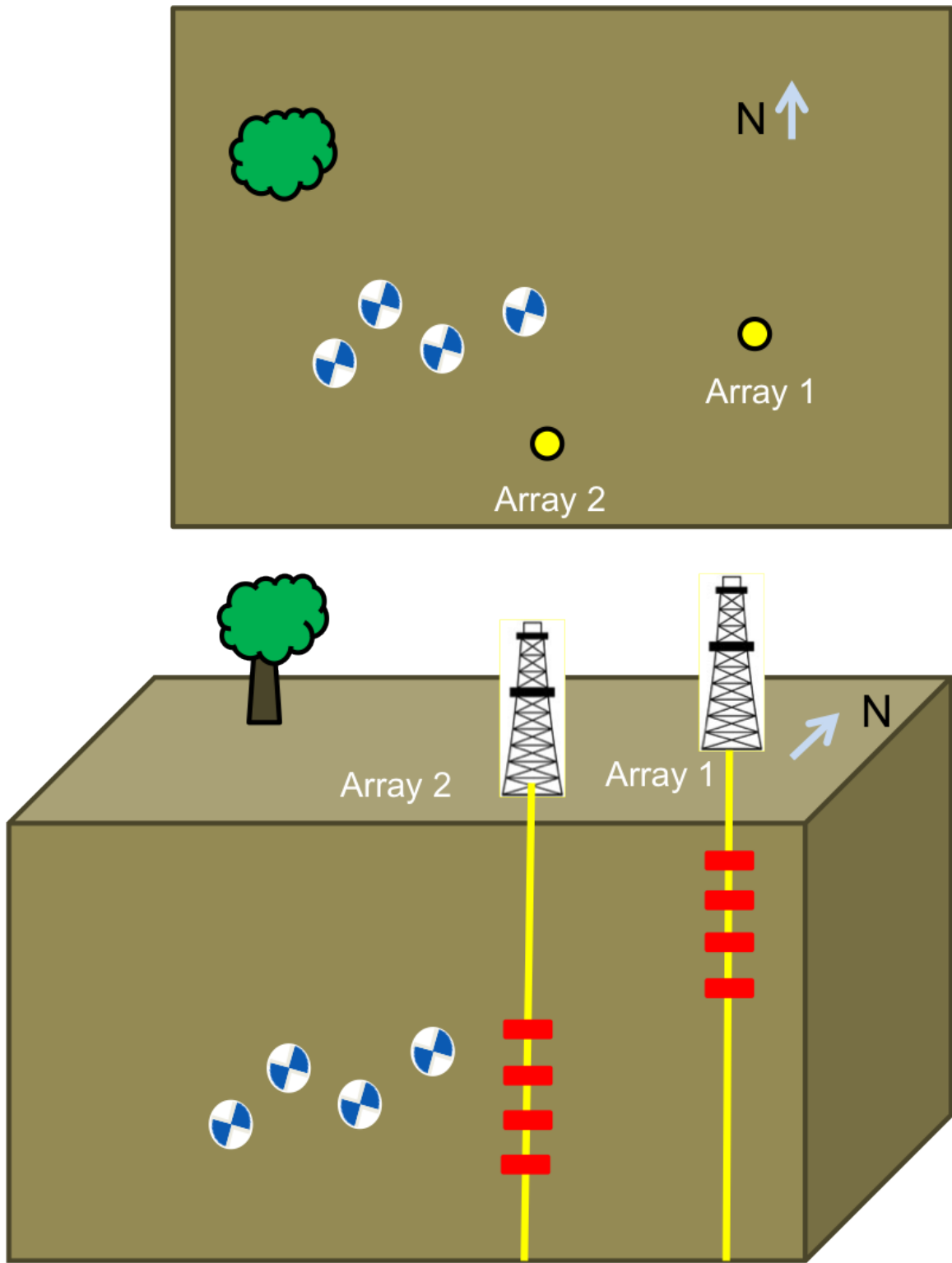


Figure 5.3: Schematic of geophone positioning, array locations, and microearthquakes. The geophone locations are represented by red bars.

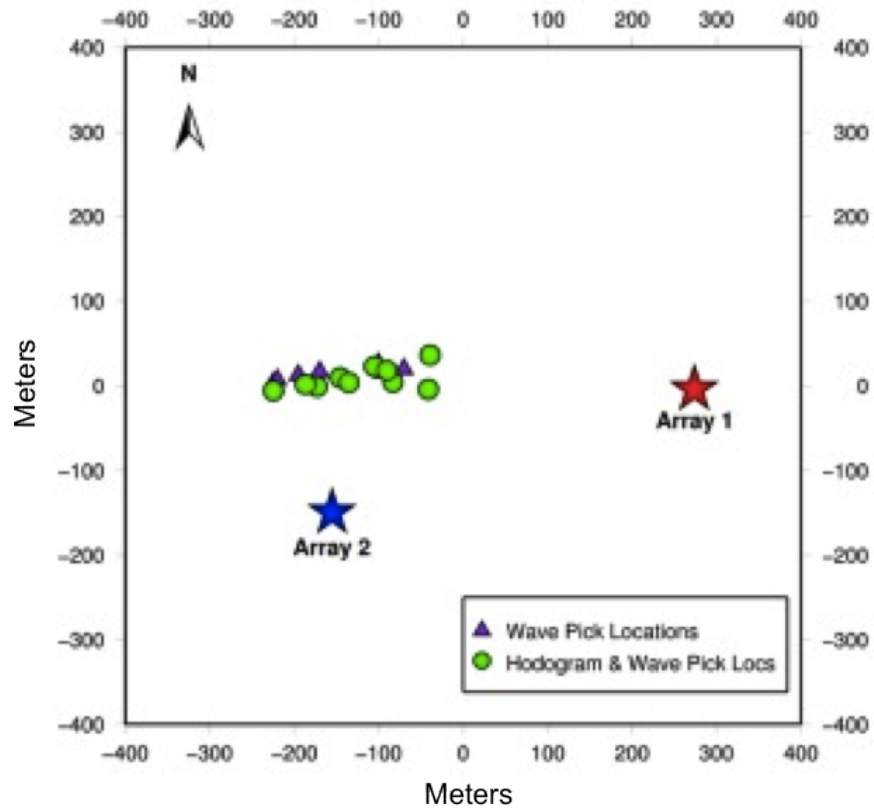


Figure 5.4: Event locations calculated using P and S arrivals from geophones in both arrays (triangles) and array 2 P and S Picks and P-hodograms. The coordinate system is local and in meters.

In both arrays, the distance between neighboring geophones within an array was between 11 and 13 m. The two monitor wells sit along a line trending NNE, and the fracture initiation well was 160 m west of array 1 and 310 m west of array 2. All fractures and microseismic events recorded by the arrays occurred along a line striking east-west.

### 5.3.2 Piceance Microearthquakes and Their Locations

The arrays in both monitor wells recorded thousands of microseismic events over the course of multiple stages of hydraulic fracturing. Although there were many events, the low signal to noise ratio of the data recorded by the geophones made it possible to identify and pick P and S-wave arrivals on only 50 of the events recorded by both arrays. Only 15 of these events had P-wave hodograms of high enough quality to allow for accurate location of the events.

Table 5.1: Altcom Velocity Model

Depth (km)	P Velocity (km/s)	S Velocity (km/s)
-1.02	4.36	2.44
-1.06	4.46	2.49
-1.1	3.89	2.00
-1.14	4.34	2.67
-1.16	4.16	2.64
-1.2	4.08	2.45
-1.22	4.24	2.78
-1.24	3.76	2.20
-1.26	4.38	2.62
-1.28	4.01	2.81
-1.3	4.66	2.74
-1.36	4.61	2.60
-1.38	4.47	2.95
-1.4	4.35	2.51
-1.44	4.14	2.55
-1.46	4.21	2.52
-1.48	4.20	2.49
-1.5	4.00	2.42
-1.52	4.09	2.48
-1.54	4.00	2.42
-1.56	3.81	2.31
-1.58	3.20	2.40
-1.6	3.68	2.28
-1.62	3.58	2.20
-1.64	3.49	2.17
-1.66	3.53	2.20
-1.68	3.61	2.26
-1.7	3.57	2.20
-1.72	4.12	2.44
-1.74	4.21	2.49
-1.76	4.06	2.42
-1.78	4.55	2.58
-1.8	4.11	2.50

Earthquakes were located using a velocity model built from  $V_p/V_s$  logs in conjunction with P and S arrivals and hodograms (table 5.1). Locations were determined using data from either both arrays or the array closest to the stimulation well (array 2) (figure 5.4). When locating events with only one array, P-hodograms were used to determine the optimum azimuth of energy propagation. Using two arrays should improve the location estimates because this eliminates the 180 degree uncertainty of the azimuth direction. Two-array event location determination also reduced the major axis of the location error ellipsoids by one standard deviation and reduced uncertainties associated with P and S-wave arrival picks and the velocity model by a factor of 2 (*Jupe et al., 2011*).

Ten of the events with the clearest P and S-wave arrivals and clearest P-hodograms were provided for this study. Of these, eight had arrivals clear enough to be used with CAP. The names of the events in the final list are 4960, 5069, 5169, 5407, 5547, 5740, 5779, and 5834. These events were all recorded by both arrays, but data recorded by the geophones in array 2 had a much higher signal to noise ratio. All data were in velocities and was provided in raw form, i.e., the amplitudes of the velocity data did not reflect actual amplitudes recorded at each geophone. Because the shape of the waveform is the same whatever the amplitude scale, the data could still be used to calculate accurate source mechanisms using CAP. The inaccuracy of the amplitude only prevents the magnitudes of the microearthquakes from being calculated correctly.

## 5.4 Methods

### 5.4.1 Data Preparation

The steps taken to prepare microseismic data for use with CAP are different from the steps taken when using regional data. CAP requires an origin time to be present within the data. The origin time is the starting point from which synthetic waveforms and data are lined up. Pnl and surface wave portions of the synthetic waveforms are then shifted in time from this starting point until the best cross correlation between data and synthetic is found. Because microseismic data do not generally come with origin times, they had to be estimated from the P arrival time and P-wave velocity model (figure 5.5). In the case of the Piceance data, we calculated origin times using the P arrival and 4.06 km/s, the average P-velocity in the velocity model. Because P arrival times change with depth as a result of moveout, the average P arrival time for each event was used to generate an origin time. CAP also requires that data be rotated to the appropriate great circle path so that the data can be separated into different arrival phases. The locations of the geophones and earthquakes were provided only in meters. In order to rotate the data properly within the program used to perform these analyses, all values in meters had to be converted to decimal degrees.

Green's functions used to build synthetic waveforms used in CAP were generated using a frequency-

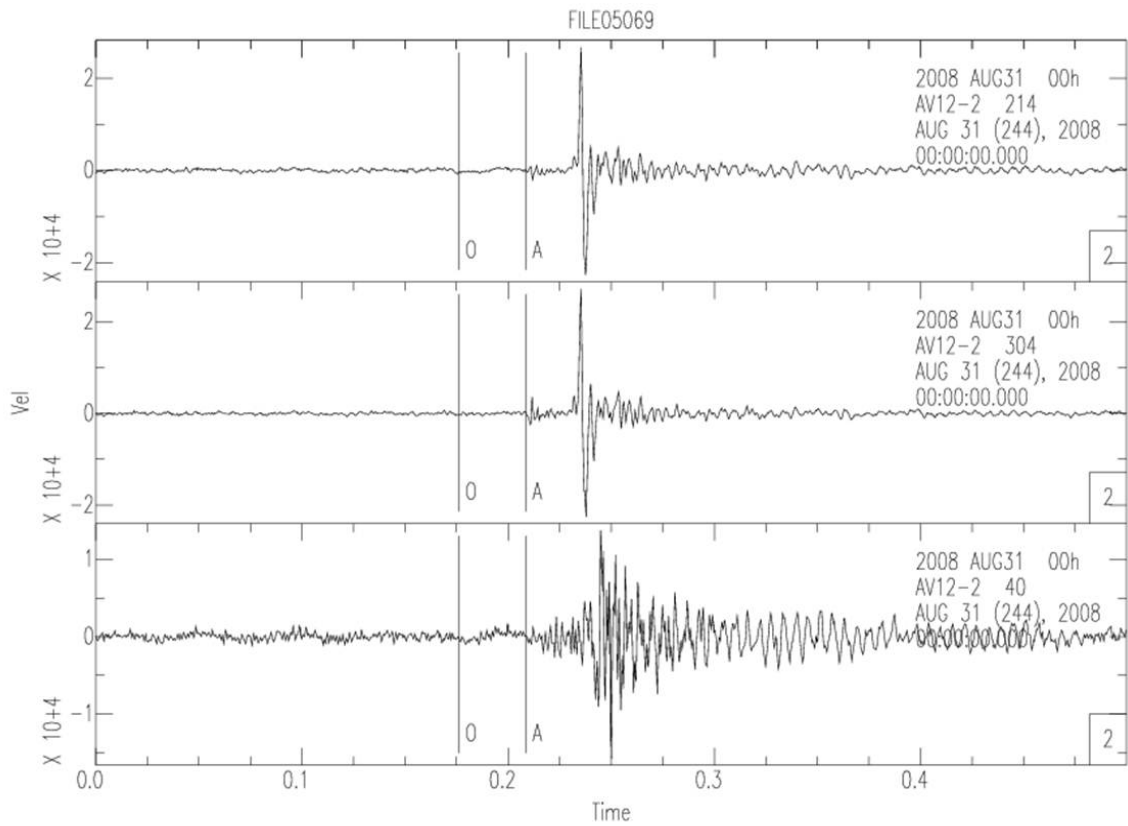


Figure 5.5: A 3-component record of event 5069 from geophone 13 in array 2. The origin time is marked by “O” and the P arrival is marked by “A”. Towards the end of the record, identifying record information has been obscured. The title “00:00:00.000” is simply the start time of the record.

wavenumber (FK) factorization code and a velocity model provided by the oil company vendor which processed the microseismic data. This same velocity model was used to calculate the earthquake locations. In order for the FK code to generate Green's functions, the velocity model had to be modified to include P and S-wave attenuation values. Appropriate values for P and S attenuation within the Williams Fork Formation are 50 and 100 respectively (Anca Rosca, Personal Communication., 2009), and these were added to the model. Since the depths of the earthquakes in our data set ranged from 1400 m to 1540 m, we generated Green's functions at 10 m intervals within this depth range. These depths represent the possible depth of the source. A source mechanism was calculated using synthetics made from Green's functions at these depths, and the most likely mechanism was determined to be at the Green's function depth with the lowest error.

Once Green's functions are generated, they must have P and S arrival times marked within them. Because the earthquakes locations were so close to the geophones, the regional travel time calculating code used to place the P and S arrival times within the Greens functions could not be used. As a result, all P and S arrivals were manually marked within each of the Green's functions. After arrival the needed modifications were made to the velocity model and Green's functions, the amplitude of the original microseismic data had to be reduced so that it was the same order of magnitude as the Green's functions. This last modification, although seemingly extraneous, had to be performed so CAP would run.

#### **5.4.2 Running CAP**

Because we were given two sets of locations, one calculated using P and S arrival picks and the other calculated using P-hodograms and array 2 P and S arrival picks, we decided to run CAP at both sets of locations to see which one would provide the best results, i.e., those with the lowest time shifts and highest cross correlation fits. The inputs used to run CAP were the same for both sets of event locations. The grid search to determine the strike and rake of the source mechanism was performed by searching between 0 and 360 degrees for strike, 0 and 90 degrees for dip, and -90 and 90 degrees for rake. The search interval within the grid search was 5 degrees for strike and 1 degree

for dip and rake. The maximum time shifts used to fit the Pnl waves and surface wave synthetics to the data were 0.05 and 0.15 s respectively. Before running, CAP performs a band-pass filter of the data so that noise can be removed. Because the frequency range of our earthquake data is quite high, we used a filter of 50 to 100 Hz for Pnl and surface waves. We also used a source duration of 0.05 s.

After performing two separate CAP runs using all geophone records and the locations determined from either P and S arrival picks or the P and S arrival picks and P-hodograms, we decided to work on improving the results by running CAP using only the records with the clearest P and S arrivals. We assumed that, because these data were less noisy, we would be able to obtain a more accurate result. We also tried to improve our results by going through the time shifts and fits recorded at each station during the “all record” runs for both sets of locations and running the stations with the best results again.

## 5.5 Results

For each event we obtained six different focal mechanisms (figures 5.6 , 5.7, 5.8 , 5.9). The first set of three focal mechanisms was determined using the locations determined from P- and S-wave picks only. Each of these three mechanisms were then calculated using records from all stations (the “all” mechanism), records from the stations with the clearest arrivals (the “best” mechanism), and records from the stations with the best CAP results when CAP was run with all stations (the “best rerun” mechanism). The second set of three mechanisms was determined using the locations obtained from P-hodograms and arrival picks. Each of these three mechanisms was produced according to the same guidelines as those in the first set.

### 5.5.1 Event Mechanisms

Event 4960 is located on the eastern edge of the swarm of microearthquakes and has highly variable mechanisms. The “best rerun” and “best” mechanisms obtained using the array1 and array 2 arrival picks locations are both NE/NW striking strike-slip events, but the “all” event is a NE/NW striking

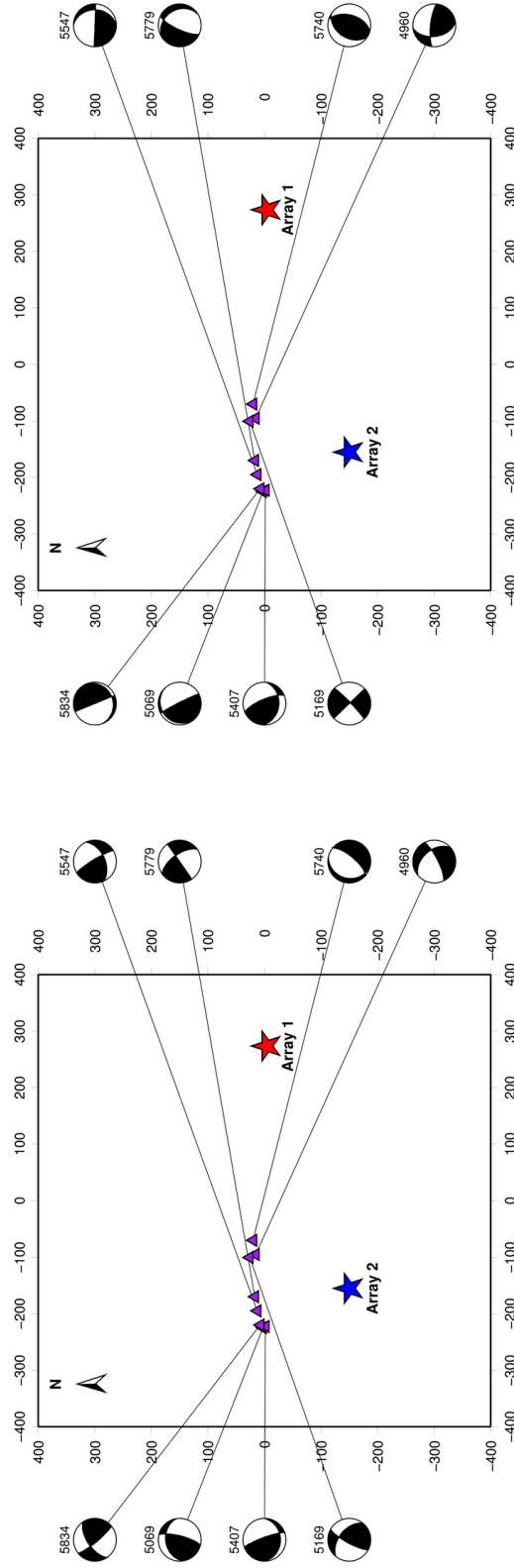


Figure 5.6: CAP source mechanisms obtained using locations obtained from P and S arrivals and for all three runs. “All” mechanisms (left) and “best” mechanisms (right).

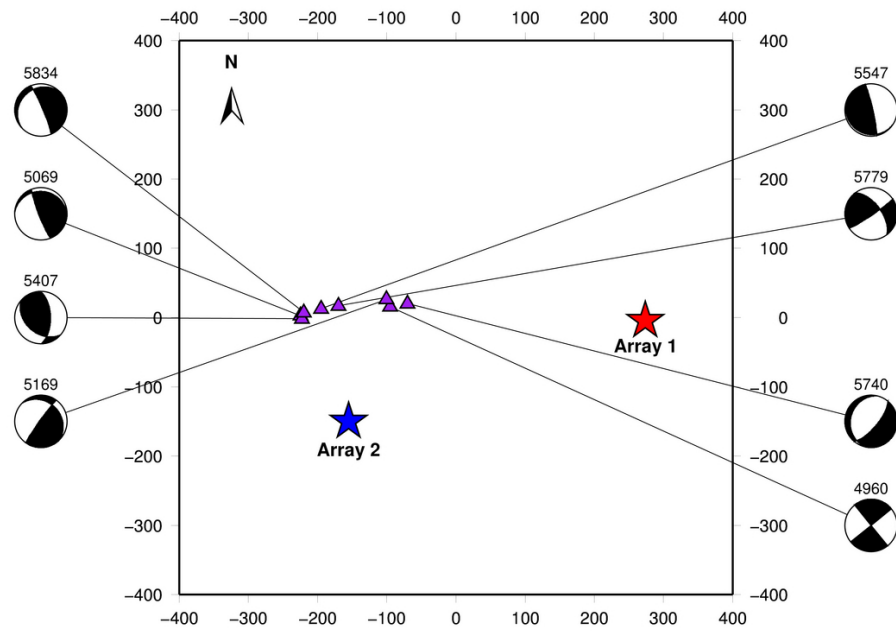


Figure 5.7: CAP source mechanisms obtained using locations obtained from P and S arrivals and for all three runs (continued). Only “best rerun” mechanisms (bottom) are shown.

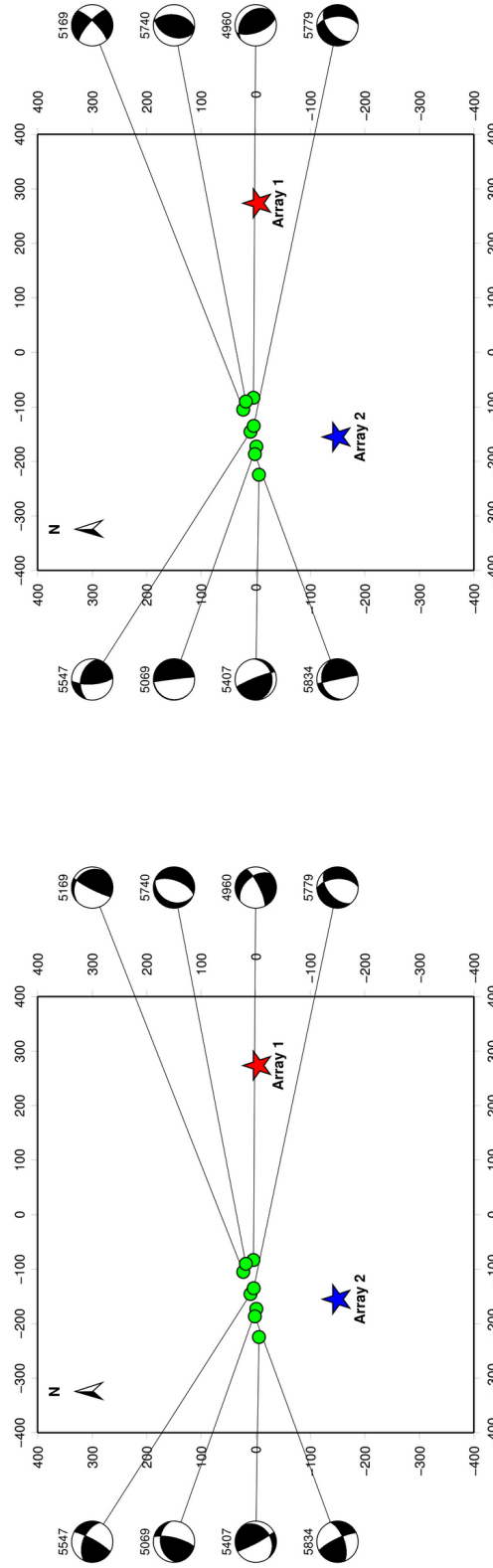


Figure 5.8: CAP source mechanisms obtained using locations obtained from array 2's P and S arrivals and P-hodograms for all three runs. "All" mechanisms (left) and "best" mechanisms (right) are shown.

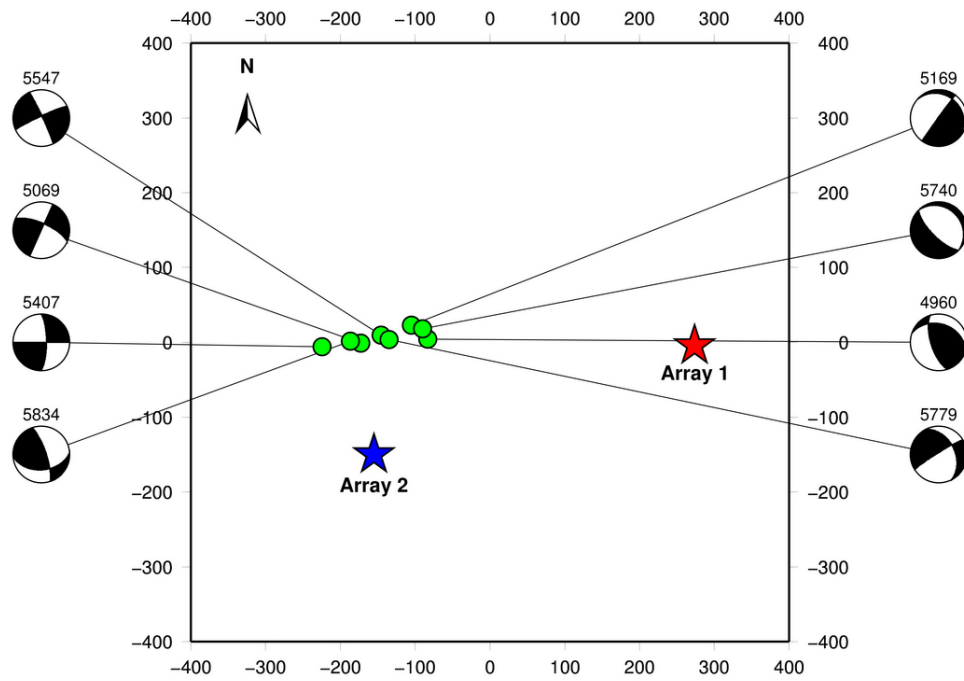


Figure 5.9: CAP source mechanisms obtained using locations obtained from array 2's P and S arrivals and P-hodograms for all three runs. Only "best rerun" mechanisms are shown.

oblique normal fault. The arrival picks and hodograms results have a greater thrust component. The sense of motion imaged by the “best” and “best rerun” mechanisms are NW striking thrust and NW striking oblique thrust. The “all” mechanism is a NE/NW striking oblique normal event that looks very similar to the “all” mechanism calculated using the arrival picks location.

Event 5069 is located on the far western edge of the swarm of microearthquakes. Its mechanisms are more consistent than those of 4960. The “all” mechanism for the arrival picks locations and array 2 arrival picks and P-hodogram locations are both NE striking oblique thrusts. The “best” and “best rerun” mechanisms calculated from the arrival picks locations are both NE/NW striking oblique thrust events with one very low angle plane. Only the “best rerun” mechanism calculated from arrivals and P-hodograms is a NE/NW striking normal fault.

Event 5169 (figure 5.10) is located just to the east of the center of the swarm of microearthquakes and has a more consistent set of mechanisms than 5169 or 5069. The “all” and “best” mechanisms for the arrival picks locations as well as the “best” and “best rerun” for the array 2 arrival picks and P-hodogram locations all show motion along a NE/NW striking strike-slip fault. The remaining mechanisms are both NE/NW striking oblique slip mechanisms with a thrust component.

Event 5407 is located on the western edge of the swarm and also has a fairly consistent set of source mechanisms. Four of the six mechanism show motion along an oblique thrust fault. The oblique thrust faults in the case of the “all” and “best” mechanisms calculated using both arrival picks have a NW or EW strike. The “all” and “best” mechanisms calculated using the array 2 arrival picks and P-hodograms locations are NE/NW striking oblique thrusts. The remaining “best rerun” events are NW-striking oblique thrust and NS/EW striking strike-slip.

Event 5547 (figure 5.11) is also located in the western half of the swarm. Both “all” mechanisms and the “best rerun” mechanism generated using arrival picks and P-hodograms show motion along a NE/NW striking strike-slip fault. The “best” and “best rerun” mechanisms determined using arrival picks locations are both likely to be NE/NW striking oblique thrust faults, but the “best rerun” event has one very low angle plane and could possibly have a component of normal motion instead of thrust motion. The “best” mechanism determined using array 2 arrival picks and P-hodograms



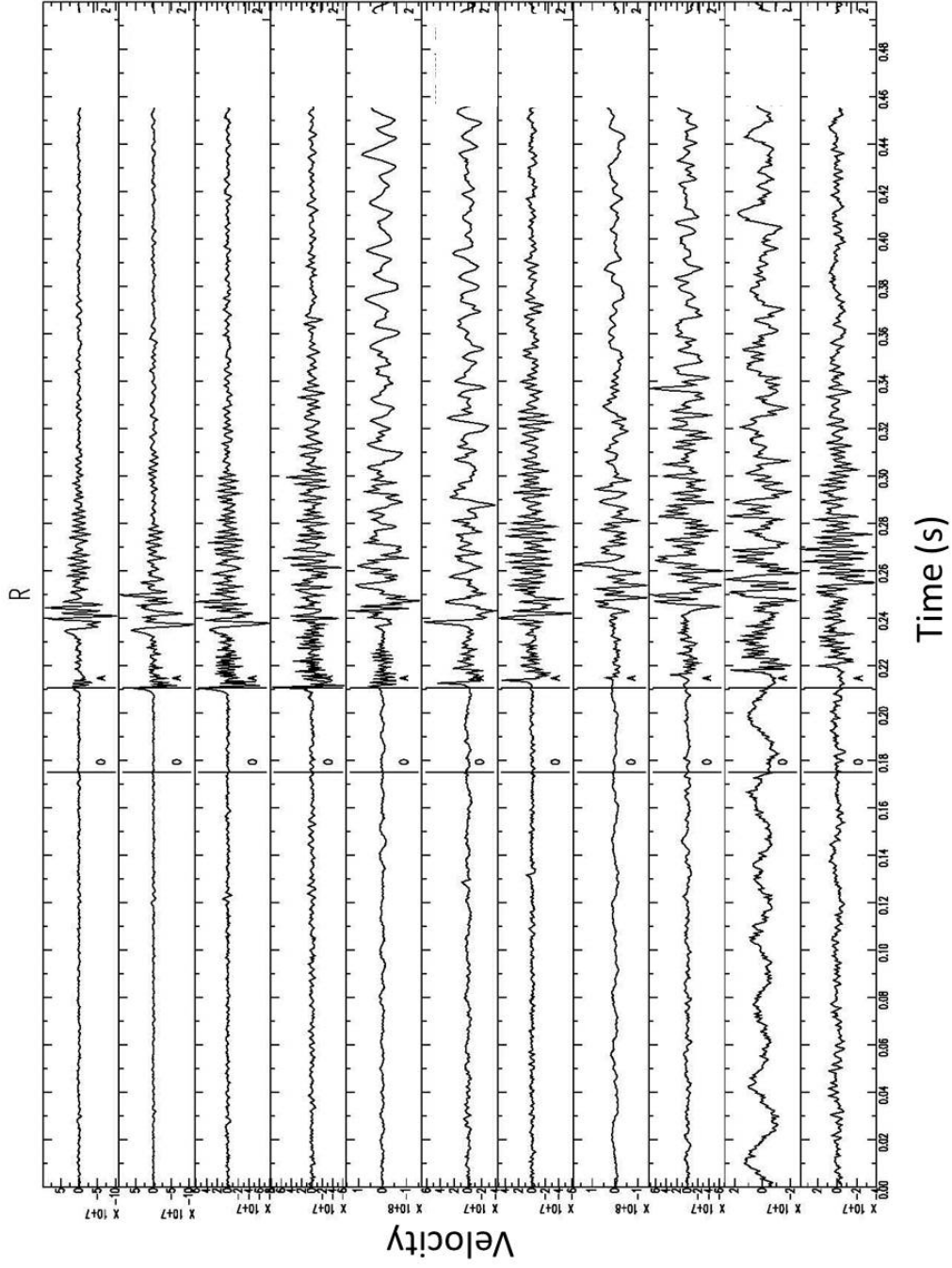


Figure 5.11: The R components of event 5547 records. These records are an example of those which become noisier as the depths of the geophones increase i.e., as one moves downhole. Identifying record information has been removed, causing the end of the record to be obscured.

is a northwest-striking oblique thrust.

Event 5740 is also in the eastern portion of the swarm. The mechanisms calculated from both sets of locations display motion with opposite polarities. Both sets of “all” and “best rerun” mechanisms display motion along a NE-striking normal fault, and both sets of “best” events show motion along a NW-striking thrust fault.

Event 5779 is located in the center of the swarm and has the most consistent set of source mechanisms. All mechanisms display motion along NE- or NW-striking strike-slip faults which have a variable component of normal motion.

Event 5834 is located on the western edge of the swarm and has a much more variable set of mechanisms than 5779. Both “all” mechanisms and are NW- or NE-striking strike-slip faults. The “best” mechanism calculated using the arrival picks location and the “best rerun” location calculated using the array 2 arrival picks and P-hodograms show motion along faults with NW or EW strike-slip motion. The “best” rerun event calculated using the arrival picks and P-hodograms location shows motion along an oblique normal fault.

## 5.6 Discussion

CAP was able to calculate source mechanisms of microearthquakes recorded within the Piceance Basin using locations determined from arrival picks and P-hodograms, but the quality of the source mechanisms obtained is dubious. The data recorded by the borehole geophones are incredibly noisy, making arrival times difficult to pick and the locations determined from these arrival times unreliable. We tried to alleviate the noise problem filtering the data, but we were unable to find a filter that would remove the noise without further compromising data quality.

When tables of time shifts, cross correlation fits, and source characteristics are examined the relationship between poor data quality and poor results is revealed. In the case of noisy events such as 4960, 5069, and 5834, the low signal to noise ratio data lead to very poor cross correlation fits and source mechanisms with highly variable source characteristics (tables 5.2, 5.3, 5.4, 5.5). Even when starting with a location obtained from the cleaner records from array 2 and their associated

Table 5.2: CAP Time Shifts and Fits for locations from Array 2 P and S Picks and P-Hodograms

Event	Pnl R Shift (s)	Pnl R Fit	Pnl V Shift (s)	Pnl V Fit	V Shift (s)	V Fit	R Shift (s)	R Fit	T Shift (s)	T Fit	Run	Data Quality	Mechanism Consistency	Fit Quality
FILE4960	0.02	37	0.02	48	0.02	36	0.02	49	0.03	50	all			
	0	48	0	51	0	47	0	51	0	67	best	noisy	highly variable	bad fits
	0.01	57	0.01	51	0.01	57	0.01	50	0.03	49	best rerun			
FILE5069	0.03	36	0.03	40	0.03	36	0.03	38	0	43	all			
	0	34	0	25	0	34	0	16	-0.01	65	best	noisy	highly variable	very bad fits
	-0.01	15	-0.01	36	-0.01	14	-0.01	34	-0.06	63	best rerun			
FILE5169	-0.02	44	-0.02	35	-0.02	43	-0.02	33	0.03	48	all			
	0.01	61	0.01	62	0.01	60	0.01	61	0	71	best	very noisy	somewhat consistent	ok fits
	-0.03	44	-0.03	46	-0.03	43	-0.03	42	0	61	best rerun			
FILE5407	-0.01	25	-0.01	74	-0.01	25	-0.01	71	-0.05	33	all			
	0	44	0	50	-0.04	55	-0.04	37	-0.04	33	best	clean	somewhat consistent	ok fits
	-0.01	62	-0.01	73	-0.01	59	-0.01	70	-0.05	39	best rerun			
FILE5547	-0.02	0	-0.02	51	-0.02	0	-0.02	47	0	48	all			
	0.01	33	0.01	28	0.01	32	0.01	29	0.01	42	best	noisy downhole	somewhat consistent	very bad fits
	-0.02	0	-0.02	58	-0.06	16	-0.06	48	-0.01	70	best rerun			
FILE5740	0.01	64	0.01	18	0.01	63	0.01	11	-0.12	33	all			
	-0.05	59	-0.05	18	-0.05	59	-0.05	15	-0.01	58	best	noisy	opposite	ok fits
	0.01	64	0.01	18	0.01	63	0.01	11	-0.12	33	best rerun			
FILE5779	0	70	0	0	0	69	0	0	0	64	all			
	0	69	0	2	0	68	0	0	0	68	best	clean	consistent	very good fits
	0	70	0	0	0	70	0	0	0	64	best rerun			
FILE5854	0.03	23	0.03	44	0.03	27	0.03	38	0	44	all			
	0.01	53	0.01	7	0.01	52	0.01	7	-0.06	67	best	noisy	inconsistent	bad fits
	-0.05	46	-0.05	51	-0.05	43	-0.05	45	-0.04	68	best rerun			

Table 5.3: CAP Time Shifts and Fits for locations from P and S Picks

Event	Pnl R Shift (s)	Pnl R Fit	Pnl V Shift (s)	Pnl V Fit	V Shift (s)	V Fit	R Shift (s)	R Fit	T Shift (s)	T Fit	Run	Data Qual- ity	Mechanism Consistency	Fit Quality
FILE4960	0.01	45	0.01	44	0.01	44	0.01	47	0.03	49	all			
	-0.04	25	-0.04	24	-0.04	24	-0.04	41	0	65	best	noisy	highly variable	bad fits
	0	44	0	42	0	42	0	41	0.03	49	best rerun			
FILE5069	0.03	0	0.03	0	0.03	0	0.03	48	0.01	45	all			
	-0.04	43	-0.04	41	-0.04	41	-0.04	7	-0.05	65	best	noisy	highly variable	bad fits
	0.03	35	0.03	30	0.11	30	0.11	13	0.11	54	best rerun			
FILE5169	-0.03	43	-0.03	42	-0.03	42	-0.03	44	0.03	47	all			
	0	63	0	62	0	62	0	62	0	71	best	very noisy	somewhat consistent	ok fits
	-0.03	42	-0.03	41	-0.03	41	-0.03	42	0.03	46	best rerun			
FILE5407	-0.01	37	-0.01	36	-0.01	36	-0.01	71	-0.02	41	all			
	-0.01	54	-0.01	53	-0.01	53	-0.01	42	-0.05	42	best	clean	somewhat consistent	ok fits
	0.03	52	0.03	50	0.03	50	0.03	60	-0.05	39	best rerun			
FILE5547	0.04	31	0.04	31	0.04	31	0.04	59	0.03	45	all			
	-0.01	40	-0.01	38	-0.01	38	-0.01	44	0	53	best	noisy downhole	somewhat consistent	ok fits
	0	58	0	12	0.05	12	0.05	44	0.01	70	best rerun			
FILE5740	-0.04	59	-0.04	59	-0.04	59	-0.04	35	-0.12	36	all			
	-0.05	57	-0.05	57	-0.05	57	-0.05	11	0	58	best	noisy	opposite	good fits
	0.01	63	0.01	62	0.01	62	0.01	37	-0.12	33	best rerun			
FILE5779	0.02	71	0.02	71	0.02	71	0.02	71	-0.02	47	all			
	0.02	71	0.02	71	0.02	71	0.02	71	-0.02	47	best	clean	consistent	very good fits
	0.01	70	0.01	70	0.01	70	0.01	72	-0.03	48	best rerun			
FILE5854	0	0	0	0	0.08	0	0.08	43	0	40	all			
	-0.02	43	-0.02	24	-0.07	24	-0.07	23	0	63	best	noisy	inconsistent	bad fits
	-0.01	47	-0.01	45	-0.01	45	-0.01	38	0.07	50	best rerun			

Table 5.4: Microearthquake Source Parameters - Locations from P and S Picks

Event	X (m)	Y (m)	CAP Depth (m)	Orig Depth (m)	Strike	Dip	Rate	Run	No. of Stations	Data Quality	Mechanism Consistency
FILE4960	-95	15.7	-1420	-1470.5	114	55	54	all	12		highly variable
	-95	15.7	-1530		276	76	45	best	6	noisy	
	-95	15.7	-1420		141	90	0	best rerun	3		
FILE5069	-225	2.7	-1420	-1459.9	51	71	10	all	12		highly variable
	-225	2.7	-1520		333	86	77	best	4	noisy	
	-225	2.7	-1510		274	16	26	best rerun	2		
FILE5169	-100.3	26.3	-1420	1472.5	309	51	16	all	12		somewhat consistent
	-100.3	26.3	-1520		136	90	5	best	2	very noisy	
	-100.3	26.3	-1400		314	25	9	best rerun	4		
FILE5407	-222.5	-1.8	-1400	-1489.6	89	26	21	all	12		somewhat consistent
	-222.5	-1.8	-1450		94	33	31	best	8	clean	
	-222.5	-1.8	-1400		131	41	50	best rerun	2		
FILE5547	-195	12.6	-1440	1435.1	65	51	10	all	12		somewhat consistent
	-195	12.6	-1420		0	28	-2	best	4	noisy downhole	
	-195	12.6	-1410		126	7	49	best rerun	1		
FILE5740	-70	20	-1480	1505	40	70	-80	all	12		opposite
	-70	20	-1540		16	50	79	best	2	noisy	
	-70	20	-1480		40	70	-80	best rerun	12		
FILE5779	-169.9	16.9	-1530	1421.7	55	90	28	all	12		consistent
	-169.9	16.9	-1480		205	74	-67	best	11	clean	
	-169.9	16.9	-1530		56	85	31	best rerun	9		
FILE5854	-219.9	7.2	-1440	1450	236	62	11	all	12		inconsistent
	-219.9	7.2	-1400		338	90	-74	best	1	noisy	
	-219.9	7.2	-1470		229	19	-19	best rerun	3		

Table 5.5: Microearthquake Source Parameters - Locations from Array 2 P and S Picks and P-Hodograms

Event	X (m)	Y (m)	CAP Depth (m)	Orig Depth (m)	Strike	Dip	Strike	Dip	Strike	Depth	Run	No. of Stations	Data Quality	Mechanism Consistency
FILE4960	-83.27	4.12	-1430	-1470	319	46	319	46	319	-1470	all	12		
	-83.27	4.12	-1430		316	30	316	30	316		best	6	noisy	highly variable
	-83.27	4.12	-1430		288	35	288	35	288		best rerun	3		
FILE5069	-173.04	-1.09	-1430	-1455	14	75	14	75	14	-1455	all	12		
	-173.04	-1.09	-1470		224	3	224	3	224		best	4	noisy	highly variable
	-173.04	-1.09	-1420		24	90	24	90	24		best rerun	2		
FILE5169	-105.21	22.97	-1400	-1475	315	19	315	19	315	-1475	all	12		
	-105.21	22.97	-1520		311	75	311	75	311		best	2	very noisy	somewhat consistent
	-105.21	22.97	-1400		310	19	310	19	310		best rerun	5		
FILE5407	-224.69	-5.97	-1400	-1490	152	85	152	85	152	-1490	all	12		
	-224.69	-5.97	-1400		84	22	84	22	84		best	10	clean	somewhat consistent
	-224.69	-5.97	-1530		0	75	0	75	0		best rerun	3		
FILE5547	-145.67	9.72	-1400	-1432	29	81	29	81	29	-1432	all	12		
	-145.67	9.72	-1460		285	45	285	45	285		best	4	noisy	somewhat consistent
	-145.67	9.72	-1400		245	85	245	85	245		best rerun	4	downhole	
FILE5740	-90.25	17.95	-1480	1505	205	30	205	30	205	1505	all	12		
	-90.25	17.95	-1540		8	48	8	48	8		best	2	noisy	opposite
	-90.25	17.95	-1480		135	70	135	70	135		best rerun	6		
FILE5779	-135.07	3.71	-1440	-1420	230	50	230	50	230	-1420	all	12		
	-135.07	3.71	-1440		230	50	230	50	230		best	9	clean	consistent
	-135.07	3.71	-1500		238	85	238	85	238		best rerun	6		
FILE5854	-186.409	1.784	-1430	-1455	70	64	70	64	70	-1455	all	12		
	-186.409	1.784	-1500		254	25	254	25	254		best	1	noisy	inconsistent
	-186.409	1.784	-1420		86	45	86	45	86		best rerun	3		

P-hodograms, the cross correlation fits improved slightly or not at all. The number of stations that could be used in the inversion of source mechanisms was also reduced by noise in the data. Although CAP can be successful in inverting for source mechanisms with as little as one station (chapter 2, this thesis), it generally performs better when run using stations with have a wider range of azimuthal coverage.

Events with cleaner records, such as 5779 and 5407, had more consistent source mechanisms and better fits, no matter the location set used. The event with the cleanest records was 5779 (figures 5.13, 5.12). All of its source mechanisms were NE/NW striking strike-slip with a component of normal motion. The cross correlation coefficients were between 68 and 73 and would be a respectable result in any CAP study of regional earthquakes. Event 5547, for which noisy data were recorded only further down-hole, had passable cross-correlation fits and less variable source mechanisms. The only event that defies the trend in which clean data correlate with cross correlation fits is 5740. Although the arrivals are clear enough to pick, the noise in the data causes the records at each geophone to look different (figure 5.14). The difference in the shape of the records recorded by each geophone makes it likely that the characteristics of the CAP source mechanism would be highly dependent on the records that were picked to run. This noise-induced shape difference between records obtained at different geophones for the same event is the most likely reason for the observed variability in all event records.

The unfavorable geometry of the data acquisition setup also likely contributed to the low quality of the source mechanisms inverted for by CAP. The expense of drilling multiple monitor wells limited the azimuths at which the earthquakes could be observed to two. Because CAP can produce good quality results with limited station coverage, these well locations could have been sufficient to produce good results, but only array 2 was deep enough to obtain a good "view" of the microseismic events. Unlike array 2, the shallower array1 viewed the focal sphere from above. In regional studies using CAP, distances are large enough that a difference in the elevation of stations and the earthquakes being studied are less significant.

Although the positioning of geophones within the array 2 may be more favorable for the view

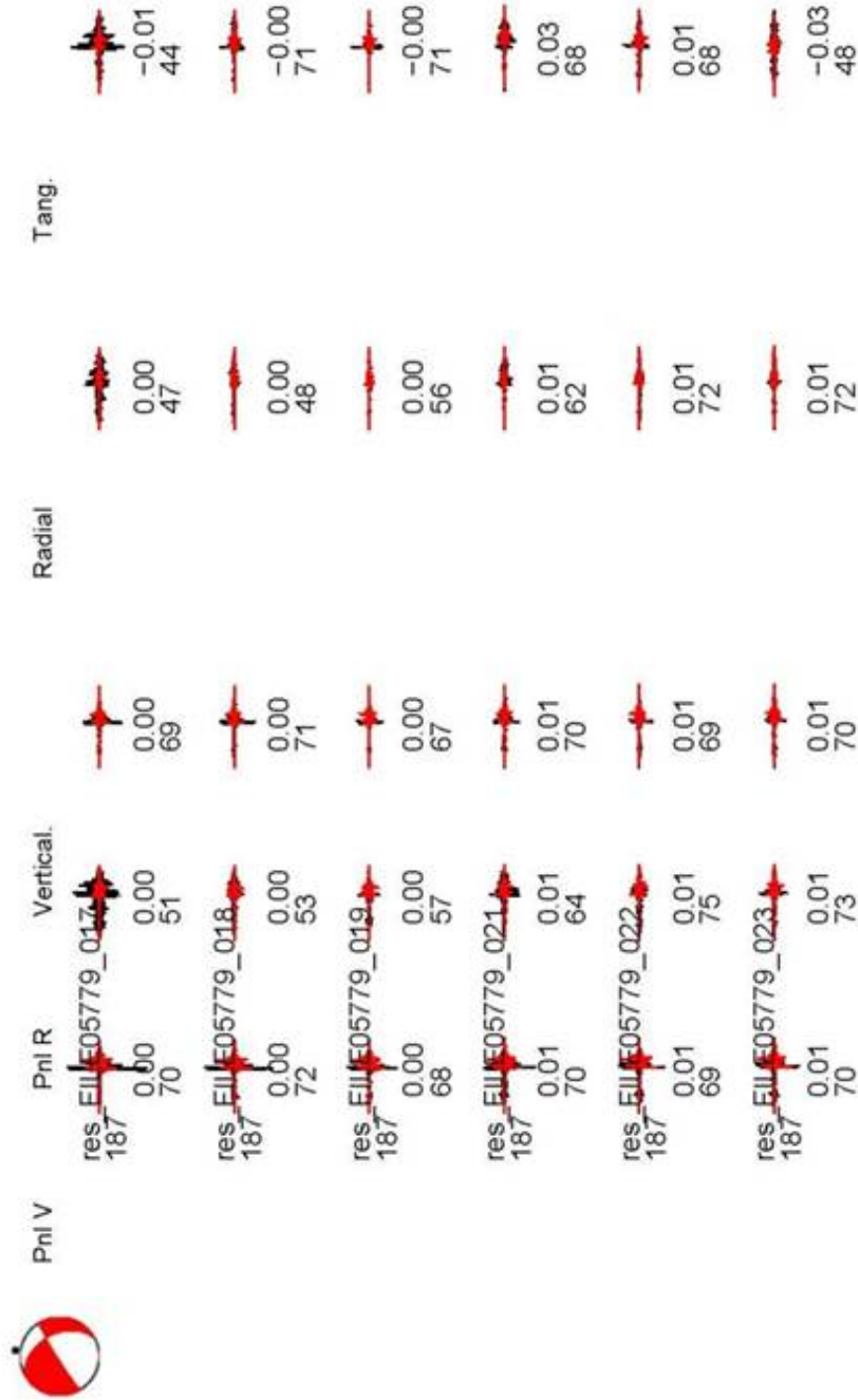


Figure 5.12: Event 5779 CAP result at 1.50 km depth. The mechanism is in the top left of the image. Data is shown in black and synthetic data generated by CAP is shown in red. The text beneath the seismogram segments are the time shifts (top) and cross correlation fits (bottom). This output is the best produced by CAP during the entire study. The time shifts and fits are on par with those which would be observed when applying CAP to the study of regional earthquakes.

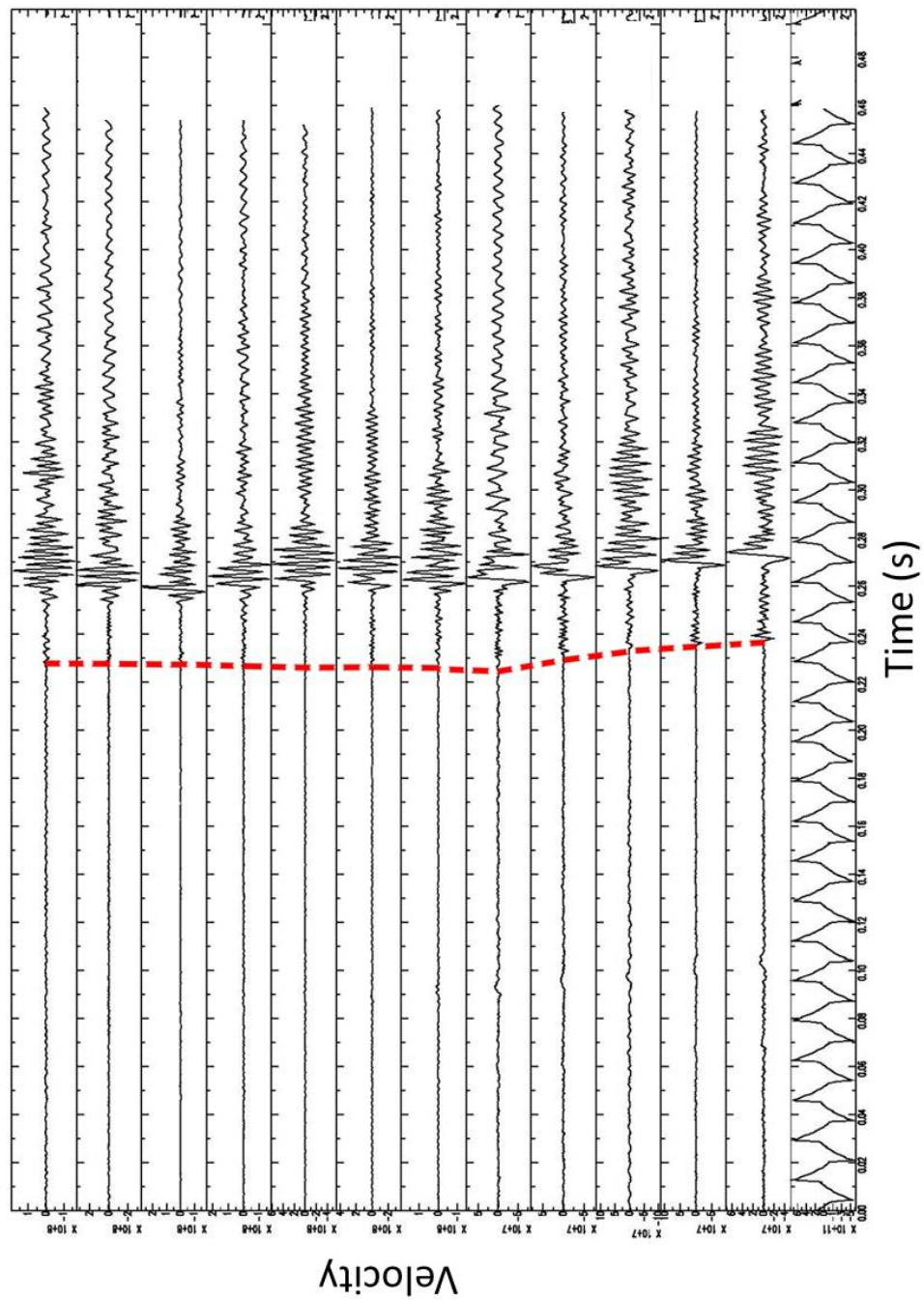


Figure 5.13: Moveout imaged in the Z component of event 5779, recorded in array 2. This is the only event with a noise level low enough to make it possible to observe this phenomenon easily. The bottommost sensor is a dummy sensor which does not record earthquake data.

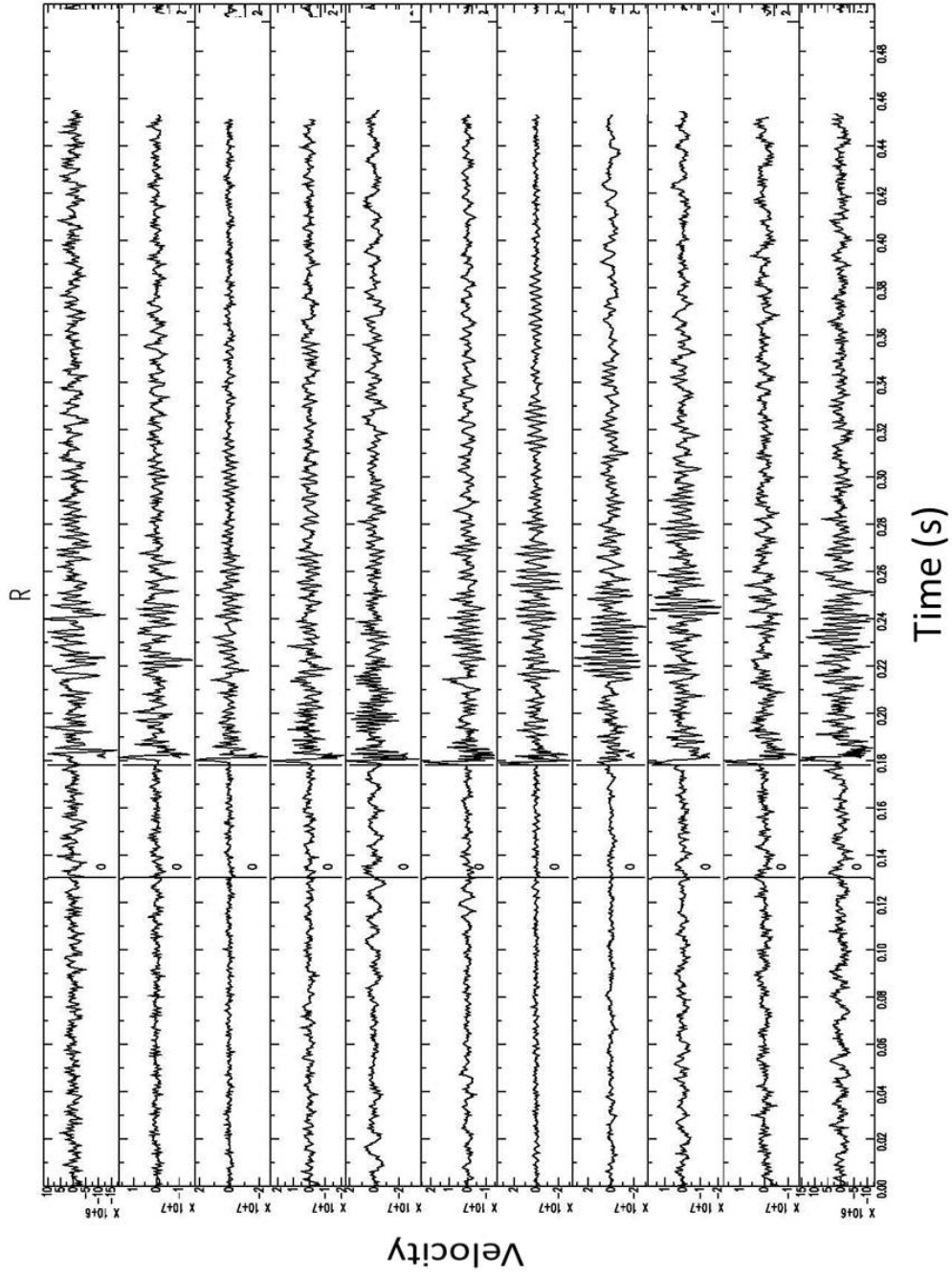


Figure 5.14: The R component of event 5740 recorded in array 2 is a good example of a noisy record. Origin time is marked by “O” and the P arrival is marked by “A”. The waveforms recorded at each station look different enough to produce different mechanisms depending on which records are chosen to run.

of the focal sphere, the favorability of the geophone depths is reduced by the fact that the F-K factorization code used to generate Green's functions within this study cannot give a result corresponding to the depth of the observed event. This means that, that if an event depth is recorded as -1470 m Green's functions will not be generated for this depth and CAP will most likely find the lowest error result at the next nearest location. Because of this issue and the 10 m interval chosen for the calculation of Green's functions, depth estimations calculated by CAP are likely off by at least 10 m.

## 5.7 Conclusion

In this study we made a preliminary attempt at using the CAP-waveform modeling method to invert for the source mechanisms of microseismic events recorded by borehole geophones. The resulting mechanisms were of questionable quality because the signal to noise ratio was low and the data acquisition geometry was suboptimal. Despite the limitations of the data set, the resulting source mechanisms were shearing events, consistent with deformation expected to be observed within high-pressure hydraulic fracturing environments. The few high-quality results obtained suggest that future studies that use CAP to obtain source mechanisms of microseismic events can be successful if data quality can be improved.

# Bibliography

- Abers, G. A. (1991), Possible seismogenic shallow-dipping normal faults in the Woodlark-Dentrecasteaux extensional province, Papua New Guinea, *Geology*, *19*, 1205–1208.
- Abers, G. A., C. Z. Mutter, and J. Fang (1997), Shallow dips of normal faults during rapid extension: Earthquakes in the Woodlark-D'Entrecasteaux rift system, Papua New Guinea, *Journal of Geophysical Research—Solid Earth*, *102*, 15,301–15,317.
- Agius, M. R., and P. Galea (2011), A single-station automated earthquake location system at Wied Dalam Station, Malta, *Seismological Research Letters*, *82*(4), 545–559.
- Albright, J. N., and R. J. Hanold (1976), Seismic mapping of hydraulic fractures made in basement rocks, *Proceedings of the Energy Research and Development Administration Symposium on Enhanced Oil and Gas Recovery*, *2*.
- Allmendinger, R. W., J. W. Sharp, D. Vontish, and et al. (1983), Cenozoic and Mesozoic structure of the eastern Basin and Range province, Utah, from cocorp seismic-reflection data, *Geology*, *11*, 532.
- Allmendinger, R. W., N. Cardozo, and D. M. Fisher (2011), *Structural Geology Algorithms: Vectors and Tensors*, Cambridge University Press, West Nyack, NY.
- Alsdorf, D., and D. Nelson (1999), Tibetan satellite magnetic low: Evidence for widespread melt in the Tibetan crust?, *Geology*, *27*(10), 943–946.
- Anderson, E. M. (1951), *The Dynamics of Faulting and Dyke Formation with Applications to Britain*, Oliver and Boyd, Edinburgh.

- Anderson, S. (1980), Western gas sands project—stratigraphy of the Piceance Basin, *Tech. rep.*, Department of Energy.
- Armijo, R., P. Tapponnier, J.-L. Mercier, and et al. (1986), Quaternary extension in southern Tibet: Field observations and tectonic implications, *Journal of Geophysical Research*, *91*(B14), 803–813,872.
- Armijo, R., P. Tapponnier, and H. Tonglin (1989), Late Cenozoic right-lateral strike-slip faulting in southern Tibet, *Journal of Geophysical Research—Solid Earth And Planets*, *94*, 2787–2838.
- Axen, G. J. (1992), Pore pressure, stress increase, and fault weakening in low-angle normal faulting, *Journal of Geophysical Research*, *97*, 8979–8991.
- Axen, G. J. (1993), Ramp-flat detachment faulting and low-angle normal reactivation of the Tule Springs Thrust, Southern Nevada, *Geological Society of America Bulletin*, *105*, 1076–1090.
- Bennett, R. A., J. Davis, J. E. Normandeau, and B. Wernicke (2002), Space geodetic measurements of plate boundary deformation in the western U.S. Cordillera, *Plate Boundary Zones, American Geophysical Union Geodynamics Series*, *30*, 27–55.
- Bennett, R. A., B. P. Wernicke, N. A. Niemi, A. M. Friedrich, and J. L. Davis (2003), Contemporary strain rates in the northern Basin and Range province from GPS data, *Tectonics*, *22*(2).
- Boettcher, M., and T. Jordan (2004), Earthquake scaling relations for mid-ocean ridge transform faults, *Journal of Geophysical Research—Solid Earth*, *109*(B12), doi:{10.1029/2004JB003110}.
- Brown, L. D., et al. (1996), Bright spots, structure, and magmatism in southern Tibet from INDEPTH seismic reflection profiling, *Science*, *274*(5293), 1688–1690.
- Burgmann, R., D. Schmidt, R. Nadeau, M. d’Alessio, E. Fielding, D. Manaker, T. McEvilly, and M. Murray (2000), Earthquake potential along the northern Hayward fault, California, *Science*, *289*(5482), 1178–1182, doi:{10.1126/science.289.5482.1178}.

- Cash, D., E. F. Homuth, H. Keppler, C. Pearson, and S. Sasaki (1983), Fault plane solutions for microearthquakes induced at the Fenton Hill hot dry rock geothermal site: Implications for the state of stress near a quaternary volcanic center, *Geophysical Research Letters*, *10*, 1141.
- Chen, L., J. R. Booker, A. G. Jones, N. Wu, M. J. Unsworth, W. Wei, and H. Tan (1996), Electrically conductive crust in southern Tibet from INDEPTH magnetotelluric surveying, *Science*, *274*(5293), 1694–1696.
- Chen, Q., J. T. Freymueller, Z. Yang, C. Xu, W. Jiang, Q. Wang, and J. Liu (2004), Spatially variable extension in southern Tibet based on GPS measurements, *Journal of Geophysical Research*, *109*.
- Chen, W. P., and P. Molnar (1981), Constraints on the seismic-wave velocity structure beneath the Tibetan Plateau and their tectonic implications, *Journal of Geophysical Research*, *86*, 5937–5962.
- Chiaraluze, L., C. Chiarabba, C. Collettini, D. Piccinini, and M. Cocco (2007), Architecture and mechanics of an active low-angle normal fault: Alto Tiberina Fault, Northern Apennines, Italy, *Journal of Geophysical Research*, *112*.
- Cogan, M. J., K. D. Nelson, W. S. F. Kidd, C. Wu, and P. I. Team (1998), Shallow structure of the Yadong-Gulu rift, southern Tibet, from refraction analysis of Project INDEPTH common midpoint data, *Tectonics*, *17*(1), 46–61.
- Cole, R. D., and S. P. Cumella (2003), Stratigraphic architecture and reservoir characteristics of the Mesaverde Group, southern Piceance Basin, *Piceance Basin 2003 guidebook: Denver, Colorado, Rocky Mountain. Association of Geologists.*, pp. 385–442.
- Collettini, C., and R. E. Holdsworth (2004), Fault zone weakening and character of slip along low-angle normal faults: insights from the Zuccale fault, Elba, Italy, *Journal of the Geological Society*, *161*, 1039–1051.
- Collettini, C., A. Niemeijer, C. Viti, S. A. F. Smith, and C. Marone (2011), Fault structure, frictional properties and mixed-mode fault slip behavior, *Earth and Planetary Science Letters*, *311*, 316–327.

- Copley, A. (2008), Kinematics and dynamics of the southeastern margin of the Tibetan Plateau, *Geophysical Journal International*, *174*(3), 1081–1100, doi:{10.1111/j.1365-246X.2008.03853.x}.
- Cornet, F. H., and P. Julien (1989), Stress determination from hydraulic test data and focal mechanisms of induced seismicity, *International Journal of Rock Mechanics and Mining Sciences & Geomechanics Abstracts*, pp. 235–248.
- Dai, H. C., and C. MacBeth (1995), Automatic picking of seismic arrivals in local earthquake data using an artificial neural-network, *Geophysical Journal International*, *120*, 758–774.
- Dai, H. C., and C. MacBeth (1997), The application of back-propagation neural network to automatic picking seismic arrivals from single-component recordings, *Journal of Geophysical Research*, *102*, 15,105–15,113.
- Davis, G. A., and G. S. Lister (1988), Detachment faulting in continental extension: perspectives from the southwestern U. S. Cordillera, *John Rodgers symposium volume. Special Paper of the Geological Society of America.*, *218*, 133–159.
- Davis, G. H. (1983), Shear-zone model for the origin of metamorphic core complexes, *Geology*, *11*, 342–347.
- Davis, G. H., and P. J. Coney (1979), Geologic development of the cordilleran metamorphic core complexes, *Geology*, *7*(3), 120–124.
- Davis, J. L., B. P. Wernicke, S. Bisnath, N. A. Niemi, and P. Elosegui (2006), Subcontinental-scale crustal velocity changes along the Pacific North America plate boundary, *Nature*, *441*, 1131–1134.
- Deng, Q., P. Zhang, Y. Ran, X. Yang, W. Min, and Q. Chu (2003), Basic characteristics of active tectonics of China, *Science in China, Series D*, *46*(4), 356–372.
- Denlinger, R. P., and C. G. Bufe (1982), Reservoir conditions related to induced seismicity at The Geysers steam reservoir, northern California, *Bulletin of the Seismological Society of America*, *72*, 1317–1327.

- Douglas, A., J. Beavan, L. Wallace, and et al. (2005), Slow slip on the northern Hikurangi subduction interface, New Zealand, *Geophysical Research Letters*, *32*.
- Dragert, H. (2001), A silent slip event on the deeper Cascadia subduction interface, *Science*, *292*(1525).
- Dragert, H., K. Wang, and G. Rogers (2004), Geodetic and seismic signatures of episodic tremor and slip in the northern Cascadia subduction zone, *Earth Planets and Space*, *56*(12), 1143–1150, 2nd International Symposium on Slip and Flow Processes in and Below the Seismogenic Region, Tokyo, Japan, Mar 10-12, 2004.
- Dreger, D. S., and D. V. Helmberger (1991), Source parameters of the Sierra-Madre earthquake from regional and local body waves, *Geophysical Research Letters*, *18*, 2015–2018.
- Dreger, D. S., and D. V. Helmberger (1993), Determination of source parameters at regional distances with three-component sparse network data, *Journal of Geophysical Research*, *98*, 8107–8125.
- Drew, J., D. Leslie, P. Armstrong, and G. Michaud (2005), Automated microseismic event detection and location by continuous spatial mapping, *Society of Petroleum Engineers (SPE) Annual Technical Conference and Exhibition*, doi:10.2118/95513-MS.
- Drewes, H. D. (1981), *Tectonics of Southeastern Arizona*, U.S. Government Printing Office.
- Eberhart-Phillips, D., and D. H. Oppenheimer (1984), Induced seismicity in The Geysers geothermal area, California, *Journal of Geophysical Research*, *89*, 1191–1207.
- Elliott, J. R., R. J. Walters, P. C. England, J. A. Jackson, Z. Li, and B. Parsons (2010), Extension on the Tibetan plateau: Recent normal faulting measured by InSAR and body wave seismology, *Geophysical Journal International*, *183*, 503–535.
- Famin, V., P. Philippot, L. Jolivet, and et al. (2004), Evolution of hydrothermal regime along a crustal shear zone, Tinos Island, Greece, *Tectonics*, *23*.
- Fan, G., and T. Wallace (1991), The determination of source parameters for small earthquakes from a single, very broadband seismic station, *Geophysical Research Letters*, *18*(8), 1385.

- Farr, T. G., et al. (2007), The shuttle radar topography mission, *Reviews of Geophysics*, 45(2), doi:{10.1029/2005RG000183}.
- Fehler, M. C. (1989), Stress control of seismicity patterns observed during hydraulic fracturing experiments at the Fenton Hill hot dry rock geothermal energy site, New Mexico, *International Journal of Rock Mechanics and Mining Sciences & Geomechanics Abstracts*, 26, 211–219.
- Feng, Q., and J. M. Lees (1998), Microseismicity, stress and fracture in the Coso geothermal field, California, *Tectonophysics*, 289, 221–238.
- Floyd, J. S., J. C. Mutter, A. M. Goodliffe, and et al. (2001), Evidence for fault weakness and fluid flow within an active low-angle normal fault, *Nature*, 411, 779–783.
- Forsyth, D. W. (1992), Finite extension and low-angle normal faulting, *Geology*, 20, 27–30.
- Frey Mueller, J. T., S. Hreinsdottir, C. Zweck, and P. J. Haeussler (2002), The 1998–2002 deep megathrust slip event, Alaska, *Eos, Transactions, American Geophysical Union (EOS)*, 83, Abstract G61A-0972, Fall Meeting Supplement.
- Frohlich, C., and J. Pulliam (1999), Single-station location of seismic events: A review and a plea for more research, *Physics of the Earth and Planetary Interiors*, 113, 277–291.
- Froitzheim, N., and G. Manatschal (1996), Kinematics of Jurassic rifting, mantle exhumation, and passive-margin formation in the Austroalpine and Penninic nappes (eastern Switzerland), *Geological Society of America Bulletin*, 108, 1120–1133.
- Galehouse, J. S. (2002), Data from theodolite measurements of creep rates on San Francisco Bay Region faults, California: 1979–2001, *Open File Report 02-225*, U.S. Geological Survey.
- Genrich, J., Y. Bock, R. McCaffrey, L. Prawirodirdjo, C. W. Stevens, S. S. O. Puntodewo, C. Subarya, and S. Wdowinski (2000), Distribution of slip at the northern Sumatran fault system, *JOURNAL OF GEOPHYSICAL RESEARCH-SOLID EARTH*, 105(B12), 28,327–28,341, doi:{10.1029/2000JB900158}.

- Gibbs, A. D. (1984), Structural evolution of extensional basin margins, *Journal of the Geological Society*, *141*, 609–620.
- Gibowicz, S. J., and A. Kijko (1994), *An Introduction to Mining Seismology*, Academic Press, Waltham, MA.
- Harrison, T. M., P. Copeland, W. S. F. Kidd, and O. M. Lovera (1995), Activation of the Nyainqentanghla shear zone: Implications for uplift of the southern Tibetan Plateau, *Tectonics*, *14*(3), 658–676.
- House, L. (1987), Locating microearthquakes induced by hydraulic fracturing in crystalline rock, *Geophysical Research Letters*, *14*, 919.
- Howard, K. A., and B. E. John (1987), Crustal extension along a rooted system of imbricate low-angle faults: Colorado River extensional corridor, California and Arizona, *Continental Extensional Tectonics, Geological Society Special Publication No. 28*, pp. 299–311.
- Hreinsdottir, S., J. Freymueller, H. Fletcher, C. Larsen, and R. Burgmann (2003), Coseismic slip distribution of the 2002 M(w)7.9 Denali fault earthquake, Alaska, determined from GPS measurements, *Geophysical Research Letters*, *30*(13), doi:{10.1029/2003GL017447}.
- Hubbert, M. K., and W. W. Rubey (1959), Role of fluid pressure in mechanics of overthrust faulting, *Bulletin of the Geological Society of America*, *70*, 115–166.
- Jackson, J. A., and N. J. White (1989), Normal faulting in the upper continental crust: observations from regions of active extension, *Journal of Structural Geology*, *11*(1/2), 15–36.
- Johnson, R. A., and K. L. Loy (1992), Seismic-reflection evidence for seismogenic low-angle faulting in southeastern Arizona, *Geology*, *20*, 597–600.
- Jolivet, L., L. Labrousse, P. Agard, and et al. (2010), Rifting and shallow-dipping detachments, clues from the Corinth Rift and the Aegean, *Tectonophysics*, *483*, 287–304.

- Jones, R. H., A. Beauce, A. Jupe, Fabriol, and C. Oyer (1995), Imaging induced microseismicity during the 1993 injection tests at Soultz-Sous-Forets, France, *Proceedings of the World Geothermal Congress*, pp. 2665–2669.
- Jupe, A., R. Jones, B. Dyer, and S. Wilson (1998), Monitoring and management of fractured reservoirs using induced microearthquake activity, *SPE/ISRM Rock Mechanics in Petroleum Engineering, 8–10 July 1998, Trondheim, Norway*.
- Jupe, A., S. Sarkar, J. Shemeta, A. Rosca, and R. Langan (2011), Uncertainty in microseismic event source parameters associated with a fracture stimulation in a tight sand when using two borehole geophone arrays, in *Society of Exploration Geophysicists Forum, Chengdu Sichuan, China, 29 March–1 April 2011*.
- Jupe, A. J., A. S. P. Green, and T. Wallroth (1992), Induced microseismicity and reservoir growth at the Fjallbacka hot dry rocks project, Sweden, *International Journal of Rock Mechanics and Mining Sciences & Geomechanics Abstracts*, 29(4), 343–354, doi:{10.1016/0148-9062(92)90511-W}.
- Jurkevics, A. (1988), Polarization analysis of 3-component array data, *Bulletin of the Seismological Society of America*, 78, 1725–1743.
- Kanamori, H., H. Thio, and D. Dreger (1992), Initial investigation of the Landers, California, earthquake of 28 June 1992 using Terrascope, *Geophysical Research Letters*, 19, 2267–2270.
- Kapp, J. L. D., T. M. Harrison, P. Kapp, and et al. (2005), Nyainqentanglha Shan: A window into the tectonic, thermal, and geochemical evolution of the Lhasa block, southern Tibet, *Journal of Geophysical Research—Solid Earth*, 110.
- Kapp, P., M. Taylor, D. Stockli, and L. Ding (2008), Development of active low-angle normal fault systems during orogenic collapse: Insight from Tibet, *Geology*, 36(1), 7–10.
- Katzir, Y., A. Matthews, Z. Garfunkel, and et al. (1996), The tectono-metamorphic evolution of a dismembered ophiolite (Tinos, Cyclades, Greece), *Geological Magazine*, 133, 237–254.

- Kim, S. G., and F. Gao (1997), Study on some characteristics of earthquakes and explosions using the polarization method, *Journal of Physics of the Earth*, *45*, 13–27.
- Kind, R., et al. (1996), Evidence from earthquake data for a partially molten crustal layer in southern Tibet, *Science*, *274*(5293), 1692–1694.
- Lachenbruch, A. H., and J. H. Sass (1988), The stress heat-flow paradox and thermal results from Cajon Pass, *Geophysical Research Letters*, *15*, 981–984.
- Langin, W. R., L. D. Brown, and E. A. Sandvol (2003), Seismicity of central Tibet from Project INDEPTH III seismic recordings, *Bulletin of the Seismological Society of America*, *93*(5), 2146–2159.
- Lay, T., and T. C. Wallace (1995), *Modern Global Seismology*, Academic Press, Waltham, MA.
- Lecomte, E., L. Jolivet, O. Lacombe, and et al. (2010), Geometry and kinematics of Mykonos detachment, Cyclades, Greece: Evidence for slip at shallow dip, *Tectonics*, *29*.
- Lecomte, E., L. L. Pourhiet, and O. Lacombe (2012), Mechanical basis for slip along low-angle normal faults, *Geophysical Research Letters*, *39*.
- Liang, X., et al. (2008), Earthquake distribution in southern Tibet and its tectonic implications, *Journal of Geophysical Research*, *113*.
- Lister, G. S., and G. A. Davis (1989), The origin of metamorphic core complexes and detachment faults formed during tertiary continental extension in the northern Colorado River region, USA, *Journal of Structural Geology*, *11*, 65–94.
- Lockman, A. B., and R. M. Allen (2005), Single-station earthquake characterization for early warning, *Bulletin of the Seismological Society of America*, *95*(6), 2029–2039.
- Lowry, A. R., K. M. Larson, V. Kostoglodov, and et al. (2001), Transient fault slip in Guerrero, southern Mexico, *Geophysical Research Letters*, *28*, 3753–3756.

- Magotra, N., N. Ahmed, and E. Chael (1989), Single-station seismic event detection and location, *IEEE Transactions on Geoscience and Remote Sensing*, *27*, 15–23.
- Majer, E. L., and T. V. McEvilly (1979), Seismological investigations at The Geysers geothermal field, *Geophysics*, *44*, 246–269.
- Makovsky, Y., S. L. Klemperer, L. Ratschbacher, L. D. Brown, M. Li, and W. Z. F. Meng (1996), INDEPTH wide-angle reflection observation of P-Wave-to-S-Wave conversion from crustal bright spots in Tibet, *Science*, *274*(5293), 1690–1691.
- Malservisi, R., C. Gans, and K. Furlong (2003), Numerical modeling of strike-slip creeping faults and implications for the Hayward fault, California, *Tectonophysics*, *361*(1-2), 121–137, doi:{10.1016/S0040-1951(02)00587-5}.
- Matsunaga, I., M. Kuriyagawa, and S. Sasaki (1989), In situ stress measurements by the hydraulic fracturing method at Imaichi pumped storage power plant, Tochigi, Japan, *International Journal of Rock Mechanics and Mining Sciences & Geomechanics Abstracts*, *26*, 203–209.
- Maxwell, S. C., J. Rutledge, R. Jones, and M. Fehler (2010), Petroleum reservoir characterization using downhole microseismic monitoring, *Geophysics*, *75*(5), 75A129–75A137.
- McBride, J. H., W. J. Stephenson, and E. I. P. McBride (2010), Reanalysis of the COCORP Utah Line deep seismic reflection profile: Toward an improved understanding of the Sevier Desert detachment question, *Geosphere*, *6*, 840–854.
- Melosh, H. J. (1990), Mechanical basis for low-angle normal faulting in the Basin and Range province, *Nature*, *343*, 331–335.
- Melosh, H. J. (1996), Dynamical weakening of faults by acoustic fluidization, *Nature*, *379*, 601–606.
- Michael, A. J. (1984), Determination of stress from slip data: Faults and folds, *Journal of Geophysical Research*, *89*(B13), 11,517–11,526.
- Michael, A. J. (1987), Use of focal mechanisms to determine stress: A control study, *Journal of Geophysical Research*, *92*(B1), 357–368.

- Molnar, P., and W.-P. Chen (1983), Focal depths and fault plane solutions of earthquakes under the Tibetan Plateau, *Journal of Geophysical Research*, 88(B2), 1180–1196.
- Molnar, P., and H. Lyon-Caen (1989), Fault plane solutions of earthquakes and active tectonics of the Tibetan Plateau and its margins, *Geophysical Journal International*, 99, 123–153.
- Molnar, P., and P. Tapponnier (1977), Relation of tectonics of eastern China to India-Eurasia collision—application of slip-line field-theory to large-scale continental tectonics, *Geology*, 5, 212–216.
- Nelson, K., et al. (1996), Partially molten middle crust beneath southern Tibet: Synthesis of project INDEPTH results, *Science*, 274, 1684–1688.
- Nolen-Hoeksema, R. C., and L. Ruff (2001), Moment tensor inversion of microseisms from the B-sand propped hydrofracture, M-site, Colorado, *Tectonophysics*, 336, 163–181.
- Ozkan, A., S. P. Cumella, K. L. Milliken, and S. E. Laubach (2010), Prediction of lithofacies and reservoir quality using well logs, Williams Fork Formation, Mamm Creek Field, Piceance Basin, *AAPG Bulletin*, 94.
- Pan, Y., and W. S. F. Kidd (1992), Nyainqentanglha shear zone: A late Miocene extensional detachment in the southern Tibetan Plateau, *Geology*, 20, 775–778.
- Parsons, T., and G. A. Thompson (1993), Does magmatism influence low-angle normal faulting?, *Geology*, 21, 247–250.
- Pavlis, G. L. (1986), Appraising earthquake hypocenter location errors: A complete, practical approach for single-event locations, *Bulletin of the Seismological Society of America*, 76, 1699–1717.
- Pearson, C. (1981), The relationship between microseismicity and high pore pressures during hydraulic stimulation experiments in low permeability granitic rocks, *Journal of Geophysical Research*, 86(B9), 7855–7864.

- Phillips, W. S., T. D. Fairbanks, J. T. Rutledge, and D. W. Anderson (1998), Induced microearthquake patterns and oil-producing fracture systems in the Austin chalk, *Tectonophysics*, *289*, 153–169.
- Pine, R. J., and A. S. Batchelor (1984), Downward migration of shearing in jointed rock during hydraulic injections, *International Journal of Rock Mechanics and Mining Sciences & Geomechanics Abstracts*, *21*, 249–263.
- Planke, S., and R. B. Smith (1991), Cenozoic extension and evolution of the Sevier Desert Basin, Utah, from seismic-reflection, gravity, and well log data, *Tectonics*, *10*, 345–365.
- Plesch, A. (2000), 3D visualization of earthquake focal mechanisms, GOCAD Wizard.
- Regenauer-Lieb, K., R. F. Weinberg, and G. Rosenbaum (2006), The effect of energy feedbacks on continental strength, *Nature*, *442*, 67–70.
- Rentsch, S., S. Buske, S. Lueth, and S. A. Shapiro (2007), Fast location of seismicity: A migration-type approach with application to hydraulic-fracturing data, *Geophysics*, *72*(1), S33–S40, doi: {10.1190/1.2401139}.
- Reston, T. (2007), Extension discrepancy at North Atlantic nonvolcanic rifted margins: Depth-dependent stretching or unrecognized faulting?, *Geology*, *35*, 367–370.
- Rice, J. R. (1992), Fault stress states, pore pressure distributions, and the weakness of the San Andreas Fault, *International Geophysics*, *51*, 475–503.
- Rietbrock, A., C. Tiberi, F. Scherbaum, and H. Lyon-Caen (1996), Seismic slip on a low angle normal fault in the Gulf of Corinth: Evidence from high-resolution cluster analysis of microearthquakes, *Geophysical Research Letters*, *23*, 1817–1820.
- Rigo, A., H. Lyon-Caen, R. Armijo, A. Deschamps, D. Hatzfeld, K. Makropoulos, P. Papadimitriou, and I. Kassaras (1996), A microseismic study in the western part of the Gulf of Corinth (Greece): implications for large-scale normal faulting mechanisms, *Geophysical Journal International*, *126*, 663–668.

- Ritsema, J., and T. Lay (1993), Rapid source mechanism determination of large (Mw 5) earthquakes in the western United States, *Geophysical Research Letters*, *20*(15), 1611–1614.
- Roberts, R. G., A. Christoffersson, and F. Cassidy (1989), Real-time event detection, phase identification and source location estimation using single station 3-component seismic data, *Geophysical Journal—Oxford*, *97*, 471–480.
- Romanowicz, B., D. Dreger, M. Pasyanos, and R. Uhrhammer (1993), Monitoring of strain release in central and northern California using broadband data, *Geophysical Research Letters*, *20*(15), 1643.
- Rutledge, J. T., and W. S. Phillips (2003), Hydraulic stimulation of natural fractures as revealed by induced microearthquakes, Carthage Cotton Valley gas field, east Texas, *Geophysics*, *68*(2), 441–452.
- Rutledge, J. T., W. S. Phillips, and M. J. Mayerhofer (2004), Faulting induced by forced fluid injection and fluid flow forced by faulting: An interpretation of hydraulic-fracture microseismicity, Carthage Cotton Valley gas field, Texas, *Bulletin of the Seismological Society of America*, *94*(5), 1817–1830.
- Ruud, B. O., and E. S. Husebye (1992), A new three-component station detector and automatic single station bulletin production., *Bulletin of the Seismological Society of America*, *82*, 221–237.
- Ruud, B. O., E. S. Husebye, S. F. Ingate, and A. Christoffersson (1988), Event location at any distance using seismic data from a single, three-component station, *Bulletin of the Seismological Society of America*, *78*(1), 308–325.
- Sarkar, S., A. Jupe, J. Shemeta, A. Rosca, and B. Langan (2011), Uncertainty in microseismic event locations associated with a fracture stimulation in a tight sand when using one, two, or more borehole arrays, *Internal Oil Company Presentation*.
- Sasaki, S. (1998), Characteristics of microseismic events induced during hydraulic fracturing exper-

- iments at the Hijiori hot dry rock geothermal energy site, Yamagata, Japan, *Tectonophysics*, 289, 171–188.
- Scholz, C. H. (2002), *The Mechanics of Earthquakes and Faulting*, Cambridge University Press, West Nyack, NY.
- Schwartz, S. Y., and J. M. Rokosky (2007), Slow slip events and seismic tremor at circum-Pacific subduction zones, *Reviews of Geophysics*, 45.
- Shapiro, S. A. (2008), *Microseismicity—A Tool for Reservoir Characterization*, EAGE Publications.
- Simpson, R., J. Lienkaemper, and J. Galehouse (2001), Variations in creep rate along the Hayward Fault, California, interpreted as changes in depth of creep, *Geophysical Research Letters*, 28(11), 2269–2272, doi:{10.1029/2001GL012979}.
- Smith, D. E., and T. H. Heaton (2011), Models of stochastic, spatially varying stress in the crust compatible with focal-mechanism data, and how stress inversions can be biased toward the stress rate, *Bulletin of the Seismological Society of America*, 101(3), 1396–1421, doi:{10.1785/0120100058}.
- Smith, K. D., D. von Seggern, G. Blewitt, L. Preston, J. G. Anderson, B. Wernicke, and J. L. Davis (2004), Evidence for deep magma injection beneath Lake Tahoe, Nevada-California, *Science*, 305(5688), 1277–1280, doi:{10.1126/science.1101304}.
- Smith, S. A. F., R. E. Holdsworth, and C. Collettini (2007), Using footwall structures to constrain the evolution of low-angle normal faults, *Journal of the Geological Society*, 164, 1187–1191.
- Sneddon, I. N. (1946), The distribution of stress in the neighbourhood of a crack in an elastic solid, *Proceedings of the Royal Society of London*, 187(1009), 229–260.
- Spencer, J. E. (1984), Role of tectonic denudation in warping and uplift of low-angle normal faults, *Geology*, 12, 95–98.
- Spencer, J. E., and C. G. Chase (1989), Role of crustal flexure in initiation of low-angle normal faults and implications for structural evolution of the Basin and Range province, *Journal of Geophysical Research—Solid Earth and Planets*, 94, 1765–1775.

- Stein, and Wysession (2003), *An Introduction to Seismology, Earthquakes and Earth Structures*, Blackwell Publishing.
- Sun, J., K. M. Johnson, Z. Cao, Z. Shen, R. Burgmann, and X. Xu (2011), Mechanical constraints on inversion of coseismic geodetic data for fault slip and geometry: Example from InSAR observation of the October 2008 Mw 6.3 Dangxiong-Yangyi (Tibet) earthquake, *Journal of Geophysical Research*, 116.
- Tan, Y., L. Zhu, D. V. Helmberger, and C. K. Saikia (2006), Locating and modeling regional earthquakes with two stations, *Journal of Geophysical Research*, 111.
- Tan, Y., A. Song, S. Wei, and D. Helmberger (2010), Surface wave path corrections and source inversions in Southern California, *Bulletin of the Seismological Society of America*, 100(6), 2891–2904.
- Tape, C. (2009), Seismic tomography of southern California using adjoint methods, Ph.D. thesis, California Institute of Technology.
- Taylor, B., J. R. Weiss, A. M. Goodliffe, M. Sachpazi, M. Laigle, and A. Hirn (2011), The structures, stratigraphy and evolution of the Gulf of Corinth rift, Greece, *Geophysical Journal International*, 185, 1189–1219.
- Taylor, M., and A. Yin (2009), Active structures of the Himalayan-Tibetan orogen and their relationships to earthquake distribution, contemporary strain field, and Cenozoic volcanism, *Geosphere*, 5(3), 199–214.
- Thio, H.-K., and H. Kanamori (1992), Moment tensor inversions in Southern California using surface waves recorded by terrascopes, *Eos, Transactions, American Geophysical Union (EOS)*, 73, 376.
- Townend, J., and M. D. Zoback (2004), Regional tectonic stress near the San Andreas fault in central and southern California, *Geophysical Research Letters*, 31.
- Wallroth, T. (1992), Hydromechanical breakdown of crystalline rock : a study based on experiments on hot dry rock geothermal energy, *Dept of Geology, CTH/GU, Gotenborg, Publ A71*.

- Warpinski, N. R., B. P. Engler, C. J. Young, R. Peterson, P. T. Branagan, and J. E. Fix (1995), Microseismic mapping of hydraulic fractures using multi-level wireline receivers, *SPE Annual Technical Conference and Exhibition*.
- Wei, S., O. Konca, N. Lin, S. Ni, and D. V. Helmberger (2009), Integrating geodesy and seismology: 2008/10/6 Tibet M6.2 events, (*unpublished*).
- Wei, W., et al. (2001), Detection of widespread fluids in the Tibetan crust by magnetotelluric studies, *Science*, *292*(5517), 716–718.
- Wernicke, B. (1995), Low-angle normal faults and seismicity: A review, *Journal of Geophysical Research*, *100*(B10), 20,159–20,174.
- Wernicke, B., and G. J. Axen (1988), On the role of isotasy in the evolution of normal fault systems, *Geology*, *16*, 848–851.
- Wernicke, B., and J. L. Davis (2010), Detecting large-scale intracontinental slow-slip events (SSEs) using geodograms, *Seismological Research Letters*, *81*(5), 694–698, doi:{10.1785/gssrl.81.5.694}.
- Wernicke, B., J. D. Walker, and M. S. Beaufait (1985), Structural discordance between neogene detachments and frontal sevier thrusts, central Mormon Mountains, Southern Nevada, *Tectonics*, *4*, 213–246.
- Wernicke, B., J. L. Davis, N. A. Niemi, P. Luffi, and S. Bisnath (2008), Active megadetachment beneath the western United States, *Journal of Geophysical Research*, *113*.
- Wesson, R. (1988), Dynamics of fault creep, *Journal of Geophysical Research—Solid Earth And Planets*, *93*(B8), 8929–8951, doi:{10.1029/JB093iB08p08929}.
- Xiao, H. B., F. A. Dahlen, and J. Suppe (1991), Mechanics of extensional wedges, *Journal of Geophysical Research*, *96*, 10,301–10,318.
- Yin, A. (1989), Origin of regional, rooted low-angle normal faults—a mechanical model and its tectonic implications, *Tectonics*, *8*, 469–482.

- Zhang, P.-Z., Z. Shen, M. Wang, W. Gan, R. Burgmann, and P. Molnar (2004), Continuous deformation of the Tibetan Plateau from global positioning system data, *Geology*, *32*, 809–812.
- Zhao, L. S., and D. V. Helmberger (1991), Broad-band modeling along a regional shield path, Harvard recording of the Saguenay earthquakes, *Geophysical Journal International*, *105*, 301–312.
- Zhao, L.-S., and D. V. Helmberger (1994), Source estimation from broadband regional seismograms, *Bulletin of the Seismological Society of America*, *84*(1), 91–104.
- Zhizhin, M. N., J. B. D. Rouland, A. D. Gvishiani, and A. Burtsev (2006), Rapid estimation of earthquake source parameters from pattern analysis of waveforms recorded at a single three-component broadband station, Port Vila, Vanuatu, *Bulletin of the Seismological Society of America*, *96*(6), 2329–2347.
- Zhu, L. (1998), Broadband waveform modeling and its application to lithospheric structure of the Tibetan Plateau, Ph.D. thesis, California Institute of Technology.
- Zhu, L., and D. V. Helmberger (1996), Advancement in source estimation techniques using broadband regional seismograms, *Bulletin of the Seismological Society of America*, *86*, 1634–1641.
- Zhu, L., Y. Tan, D. V. Helmberger, and C. K. Saikia (2006), Calibration of the Tibetan Plateau using regional seismic waveforms, *Pure and Applied Geophysics*, *163*, 1193–1213.